PHYSIK-DEPARTMENT

TECHNISCHE UNIVERSITÄT
MÜNCHEN

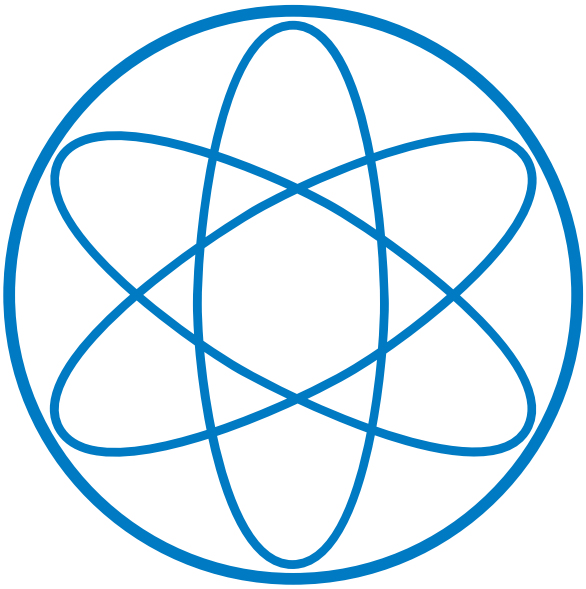

Experimental Investigation of Heat Transport and Divertor Loads of Fusion Plasma in All Metal ASDEX Upgrade and JET

Bernhard Sieglin

Max-Planck Institute for Plasma Physics
Boltzmannstr. 2, 85748 Garching

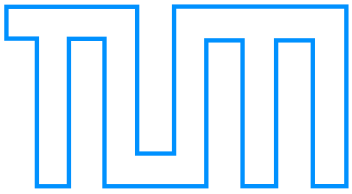

Technische Universität München

Max-Planck-Institut für Plasmaphysik

Experimental Investigation of Heat Transport and Divertor Loads of Fusion Plasmas in All Metal ASDEX Upgrade and JET

Bernhard A. Sieglin

Vollständiger Abdruck der von der Fakultät für Physik der Technischen Universität München zur Erlangung der akademischen Grades eines

Doktors der Naturwissenschaften

genehmigten Dissertation.

Vorsitzende(r)	Univ.-Prof. Dr. J. L. van Hemmen
Prüfer der Dissertation:	1. Univ.-Prof. Dr. U. Stroth
	2. Priv.-Doz. Dr. A. Ulrich

Die Dissertation wurde am 30.01.2014 bei der Technischen Universität München eingereicht und durch die Fakultät für Physik am 28.04.2014 angenommen.

Abstract

For the development of a future fusion power plant the understanding of the power flux onto the plasma facing components is mandatory, in order to predict and mitigate the thermal load onto the divertor target. This work presents divertor heat load studies conducted at two of the largest tokamaks currently in operation, ASDEX Upgrade and the Joint European Torus (JET). For a long time in fusion research carbon has been used as material for the plasma facing components. In recent years however the use of carbon has been deemed unacceptable due to high tritium retention, therefore metals are studied for the use as wall material. In 2007 ASDEX Upgrade demonstrated the operation with an all tungsten wall [1] and from 2009 to 2011 JET has been equipped with the ITER-like wall (ILW) consisting of beryllium in the main chamber and tungsten in the divertor region [2].

Using IR thermography the heat flux in L- and H-mode was measured. Various improvements were implemented in the heat flux evaluation to enable the measurement on tungsten. The thermal properties of the target materials were validated using the high heat flux test facility GLADIS.

The distribution of the steady state heat flux profile on the target is commonly described by a diffusive model containing the upstream power fall-off length λ_q and the divertor broadening S. A commonly agreed empirical scaling for λ_q in H-mode [3] obtained in carbon devices is validated in JET with the ILW.

Using ASDEX Upgrade L-mode discharges with low to medium recycling divertor conditions the divertor broadening S is studied. A comparison to theoretical and empirical models for the heat transport perpendicular to the magnetic field lines is made. Bohm and Gyro-Bohm like models are identified as possible candidates describing S.

Quantities for the assessment of the thermal load induced by transient heat loads are defined. Most important for the description of the load onto the divertor target induced by edge localised modes (ELM) are the energy fluency and the duration of the energy deposition. The pedestal temperature and density for all presented discharges in JET with both carbon and ITER-like wall was measured using the high resolution Thomson scattering(HRTS). Empirical scalings using both upstream and target data are presented.

JET with the ILW exhibits an on average longer ELM duration of about 2 ms as compared to 750 µs with the carbon wall. For identical pedestal conditions the ELM durations in both cases are found to be the same within error bars. An empirical scaling based on the pedestal temperature and density is given permitting the extrapolation towards ITER.

It is found that the energy fluency parallel to the magnetic field lines in JET is the same for both metal and carbon wall, despite the large difference in ELM duration. The energy fluency is found to depend mainly on the pedestal pressure with a weak dependence on the relative loss in stored energy. This is noteworthy since the current extrapolation to ITER assumes a linear dependence on the relative ELM size.

Zusammenfassung

Um die thermische Belastung der Komponenten im Divertor von Fusionskraftwerken vorhersagen und begrenzen zu können ist es unerlässlich den Leistungsfluss auf die plasmaexponierten Bauteile besser zu verstehen. In diese Arbeit wird der Wärmefluss auf den Divertor von zwei der grössten derzeit im Betrieb befindlichen Tokamaks, dem Joint European Torus (JET) und ASDEX Upgrade, untersucht. In der Fusionforschung wurde über einen langen Zeitraum hinweg Kohlenstoff als Material für die plasmaexponierten Bauteile verwendet. In den letzten Jahren jedoch wurde der Einsatz von Kohlenstoff für zukünftige Anlagen aufgrund des hohen Rückhalts an Tritium als inakzeptabel eingestuft, weswegen die Verwendung von Metall als Wandmaterial geprüft wird. 2007 zeigte ASDEX Upgrade erfolgreich den Betrieb mit Wolfram als Wandmaterial [1] und 2011 wurde JET mit einer ITER-ähnlichen Wand (ILW), bestehend aus Beryllium im Hauptraum und Wolfram im Divertor, ausgestattet [2].

Mit Hilfe von Infrarotthermographie (IR) wurde der Wärmefluss in den Divertor mit bisher nicht gekannter raum-zeitlicher Auflösung gemessen. Dazu wurden wesentliche Verbesserungen zur Auswertung der Daten implementiert um die Messung auf Wolfram zu ermöglichen. Die thermischen Eigenschaften der verwendeten Materialien wurden mit Hilfe des Wärmeflussteststandes GLADIS validiert.

Im Allgemeinen lässt sich die Verteilung des Wärmeflusses auf die Divertorplatten mit einem diffusiven Model beschreiben, welches die Abfalllänge der Leistung λ_q und die Verbreiterung im Divertor S enthält. Eine allgemein anerkannte empirische Skalierung für λ_q [3], welche Daten von Experimenten mit Kohlenstoff als Wandmaterial benutzt, wurde in JET mit der ILW bestätigt.

Die Verbreiterung des Leistungsflusses im Divertor S wurde in ASDEX Upgrade Entladungen in verschiedenen Divertorzuständen untersucht. Ein Vergleich mit theoretischen und empirischen Modellen für den Wärmetransport senkrecht zum magnetischen Feld wurde angestellt. Bohm- und Gyro-Bohm-artige Diffusionsmodelle werden als mögliche Kandidaten zur Beschreibung der Verbreiterung S identifiziert.

Messgrößen zur Bestimmung der durch transiente Wärmelasten induzierten thermischen Belastung werden eingeführt. Am wichtigsten für die Beschreibung der, durch sogenannten *Edge Localised Modes* oder kurz ELMs, auf die Divertorplatten induzierten Last sind die Energie Fluenz und die Dauer der Energiedeposition. Aus Daten von JET mit verschiedenen Wandmaterialien wurden empirische Skalierungen für die Divertorbelastung in Abhängigkeit der Plasmarandparameter entwickelt.

In JET-ILW ist die Dauer der Energiedeposition durch ELMs in etwa dreimal so lang wie mit der Kohlenstoffwand. Es konnte aber gezeigt werden, das für ähnliche Temperaturen und Dichten am Plasmarand sich auch ähnliche ELM-Dauern einstellen. Eine empirische Skalierung mit Hilfe der Temperatur und Dichte, welche eine Extrapolation zu ITER erlaubt, wurde gefunden.

Trotz der sehr unterschiedlichen Dauer der Energiedeposition ergeben sich in JET, sowohl mit Kohlenstoff als auch mit Metall als Wandmaterial, die selben Energieflüsse parallel zum magnetischen Feld. Es wird gezeigt, dass der Energiefluss hauptsächlich vom Druck am Plasmarand abhängt und nur ein leichter Einfluss des relativen Energieverlustes des eingeschlossenen Plasmas existiert. Dies ist erwähnenswert, da derzeitige Extrapolationen eine lineare Abhängigkeit zwischen dem relativen ELM-Energieverlust und der deponierten Energiedichte annehmen.

Contents

Chapter 1

Introduction

Due to the steady increase of the worlds power consumption and the simultaneous depletion of fossil fuels, it is necessary to investigate new ways of providing energy. One promising candidate, which has been researched since the early 1950's, is thermonuclear fusion. A commercial power plant based on thermonuclear fusion, would have many advantages compared to todays power plants. Thermonuclear fusion does not release greenhouse gases like CO_2, which can harm the global environment. Secondly there are no long lived nuclear wastes produced and the fuel supply is virtually unlimited (some 10 million years). Thirdly the resources needed to build and operate fusion power plants are more evenly spread on the earth's surface as compared to e.g. fossil fuels such as oil, mitigating one possible cause for conflicts.

1.1. Thermonuclear Fusion

The process of fusing two light nuclei into one heavier nucleus is called nuclear fusion. If this process takes place in a thermalized environment it is called thermonuclear fusion. There are many different fusion reactions, which have a positive energy balance, meaning that the kinetic energy of the products is higher than that of the educts [4].

$$\mathrm{D}_1^2 + \mathrm{D}_1^2 \longrightarrow \mathrm{He}_2^3 + \mathrm{n}_0^1 + 3.267\,\mathrm{MeV} \tag{1.1}$$

$$\mathrm{D}_1^2 + \mathrm{D}_1^2 \longrightarrow \mathrm{T}_1^3 + \mathrm{p}_1^1 + 4.028\,\mathrm{MeV} \tag{1.2}$$

$$\mathrm{D}_1^2 + \mathrm{He}_2^3 \longrightarrow \mathrm{He}_2^4 + \mathrm{p}_1^1 + 18.350\,\mathrm{MeV} \tag{1.3}$$

$$\mathrm{D}_1^2 + \mathrm{T}_1^3 \longrightarrow \mathrm{He}_2^4 + \mathrm{n}_0^1 + 17.58\,\mathrm{MeV} \tag{1.4}$$

The reaction of deuterium and tritium (eq. 1.4) has the largest fusion cross section of all fusion reactions at the lowest fusion energy (about 64 keV). This reaction is the foreseen fusion reaction for a power plant. Deuterium and tritium are isotopes of

hydrogen. Deuterium is stable and is present in earths water to an amount of about 0.0156 % [4]. Tritium is radioactive and has a half-life of about 12.6 years and therefore does not occur naturally on earth. However tritium can be bred directly in the fusion reactor utilizing lithium and the neutron from the fusion process (eq. 1.4) [4].

$$\mathrm{Li}_3^6 + \mathrm{n}_0^1 \longrightarrow \mathrm{He}_2^4 + \mathrm{T}_1^3 + 4.800\,\mathrm{MeV} \tag{1.5}$$

$$\mathrm{Li}_3^7 + \mathrm{n}_0^1 \longrightarrow \mathrm{He}_2^4 + \mathrm{T}_1^3 + \mathrm{n}_0^1 - 2.466\,\mathrm{MeV} \tag{1.6}$$

The reaction with Li_3^6 is exotherm, the reaction with Li_3^7 is endotherm but in addition releases one neutron, which in turn can react with another lithium nucleus. In order to have a self sustained fuel cycle, every neutron released in the reaction of deuterium and tritium has to produce at least one new tritium nucleus. Considering that not every neutron will react with lithium but will be captured by other parts of the reactor which are not designed to breed tritium and allowing for imperfections in the extraction of the tritium out of the breeding blanket, every neutron in fact has to produce more than one tritium nucleus on average. This can be achieved by adjusting the ratio between Li_3^6 and Li_3^7 in the breeding blanket, where Li_3^7 can act as a neutron multiplier. Further neutron multiplication will be done using other elements like beryllium.

Achieving ignition, which is the point where the fusion process can be self-sustainably run without the need for further external heating, is an important goal in fusion research. For this Lawson formulated a relationship for the minimum parameters to reach ignition [4]. This criterion contains the ion density n_i, the temperature T_i and the energy confinement time τ_E.

$$n_i\, T_i\, \tau_E \geq 5 \cdot 10^{21}\ \frac{\mathrm{keV\ s}}{\mathrm{m}^3} \tag{1.7}$$

Assuming a temperature of about 10 keV for a fusion plasma using deuterium and tritium, one can calculate that for a density of about $1 \cdot 10^{20}\ \mathrm{m}^{-3}$ an energy confinement time of 5 s is needed. These are typical values which will be present in fusion power plants with magnetic confinement.

1.2. Confinement

Due to the high temperatures of about 10 keV, no wall material can sustain the direct contact with a fusion plasma. Only three methods of confining a fusion plasma are known.

Gravitational confinement is found in stars. The gravitational force induced by the large mass of a star, counter acts the pressure induced by the fusion process,

preventing the fusion plasma to expand until it becomes too cold. Due to the large mass needed, this method cannot be reproduced on earth.

Inertial confinement utilizes the inertia of the plasma to obtain fusion. The fuel is heated up very quickly by e.g. intense laser beams until the fusion process starts. After this the fusion reaction runs until the expanding plasma has cooled below the temperature needed for fusion. Although this confinement method is also investigated for power plant usage, its main application is reported to be of military nature.

Magnetic confinement uses magnetic fields to confine the fusion plasma. In the course of fusion research there has been a multitude of different concepts for this method. The most advanced concepts are the tokamak and the stellarator.

1.3. Tokamak

In the 1950s the tokamak concept was developed in the former Soviet Union [5]. A tokamak mainly consists of three sets of magnetic field coils (fig. 1.1).

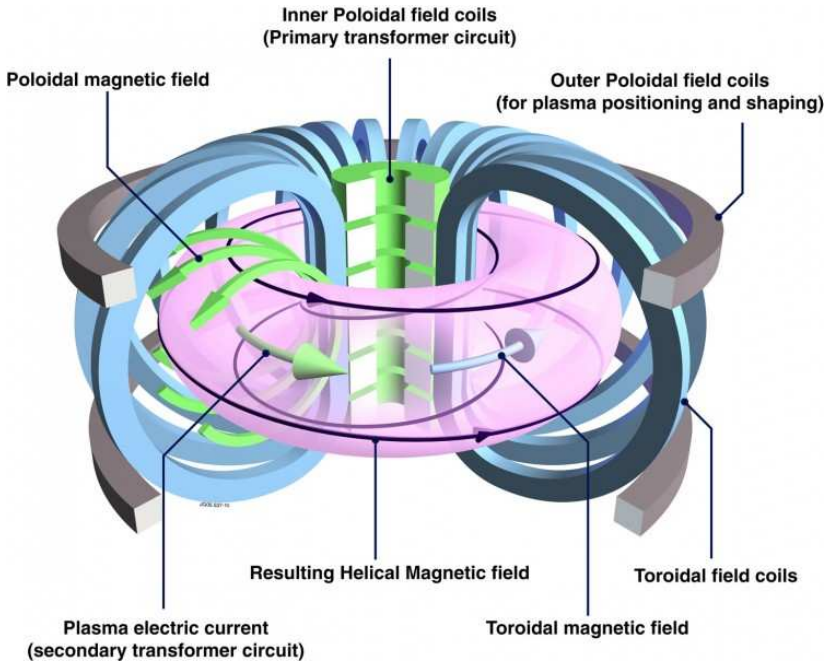

Figure 1.1: Sketch of the tokamaks magnetic coil system. Blue: toroidal field coils, grey: poloidal field coils and green: central solenoid [6].

The toroidal field coils (blue) produce a toroidal magnetic field B_{tor}. Because the field coils are closer together on the inside of the machine compared to the outside, the magnetic field is higher on the inside than on the outside. This gradient of the

magnetic field induces a particle drift in the plasma.

$$v_{\nabla B} = \frac{W_\perp}{q} \frac{\mathbf{B} \times \nabla B}{B^3} \tag{1.8}$$

Where $\mathbf{B}$ is the magnetic field, q the electric charge and $W_\perp$ the perpendicular kinetic energy of the particle. The direction of this drift dependents on the sign of the electric charge of the particles, leading to a vertical charge separation in the plasma. This charge separation in turn induces an electric field $\mathbf{E}$ which causes an additional drift velocity.

$$v_{\mathbf{E}\times\mathbf{B}} = \frac{\mathbf{E} \times \mathbf{B}}{B^2} \tag{1.9}$$

Since the direction of this drift is independent on the electric charge of the particles, it causes a net drift of the plasma. In the case of a purely toroidal magnetic field geometry, the plasma drifts horizontally outwards eventually touching the wall of the machine extinguishing the plasma.

To eliminate the $v_{\mathbf{E}\times\mathbf{B}}$ drift, the parts of the plasma with positive charge have to be connected to the parts with negative charge, balancing the charge separation and erasing the vertical electric field. This is done by the central solenoid (green) which together with the plasma acts as a transformer, inducing a toroidal electric current in the plasma. This current creates a poloidal magnetic field B_{pol}, which together with the toroidal magnetic field B_{tor} leads to helically wound magnetic field lines.

The current in the plasma forms a toroidal ring in which the opposite sides repel each other. To compensate this force the polodial field coils (gray) form a Helmholtz coil pair creating a homogeneous vertical magnetic field B_z, which prevents the plasma from expanding horizontally outward.

1.3.1. Magnetic Flux Surfaces

For an axisymmetric magnetic equilibrium, that is an equilibrium which is independent of the toroidal angle ϕ, the magnetic field lines lie in nested poloidal magnetic flux surfaces. The requirement for an equilibrium is that no net force acts on the plasma in all points. Therefore the magnetic field has to compensate the force due to the plasma

pressure (eq. 1.10).

$$\mathbf{j} \times \mathbf{B} = \nabla p \tag{1.10}$$

$$\mathbf{B} \cdot \nabla p = 0 \tag{1.11}$$

$$\mathbf{j} \cdot \nabla p = 0 \tag{1.12}$$

Equation 1.10 shows that a pressure gradient in the plasma can be sustained by an electric current $\mathbf{j}$ perpendicular to the magnetic field $\mathbf{B}$. From equation 1.10 it also follows, that there is no pressure gradient along the magnetic field lines (eq. 1.11).

In a tokamak it is useful to define the poloidal magnetic flux function ψ. This function is given by the poloidal flux contained within each magnetic surface and is thereby constant on that surface. The pressure p and the current density $\mathbf{j}$ are constant on those magnetic flux surfaces.

1.3.2. Limiter

Without further engagement there exists one poloidal magnetic flux surface that touches the wall of the tokamak, limiting the extend of the plasma. This part of the wall is called *limiter* (Figure 1.2a)). The plasma inside the flux surface touching the limiter is confined, the plasma outside of it quickly reaches the wall recombining to neutral gas. Due to the proximity of the center of the plasma and the tokamak wall, impurities released from the wall can easily reach the confined plasma. For a long time most of the tokamaks were build with limiters (e.g. JET, TFTF, Tore Supra ...).

1.3.3. Divertor

To increase the distance between the wall touching the plasma and the confined plasma a different magnetic configuration has been thought of. Additional poloidal field coils are placed above and below the plasma. The electric current in these coils is parallel to the plasma current inducing an additional poloidal magnetic field. This leads to a reduction of the poloidal magnetic flux between the plasma and the coils. If the current is strong enough to reduce the poloidal magnetic flux to zero, a new magnetic topology is created (Figure 1.2b)). The point where there is no poloidal magnetic flux, is called the X-point. A further increase of the current in the divertor coils moves the X-point closer to the confined plasma. Eventually the confined plasma does not touch the limiter anymore (fig. 1.2c)). This magnetic configuration is the so called divertor configuration. The flux surface containing this X-point is called the *separatrix*.

Plasma outside the separatrix follows the magnetic field lines and reaches the wall in the divertor region. Due to the localised energy deposition, the divertor region must be designed to handle high heat loads in the range of 10 MWm^{-2}.

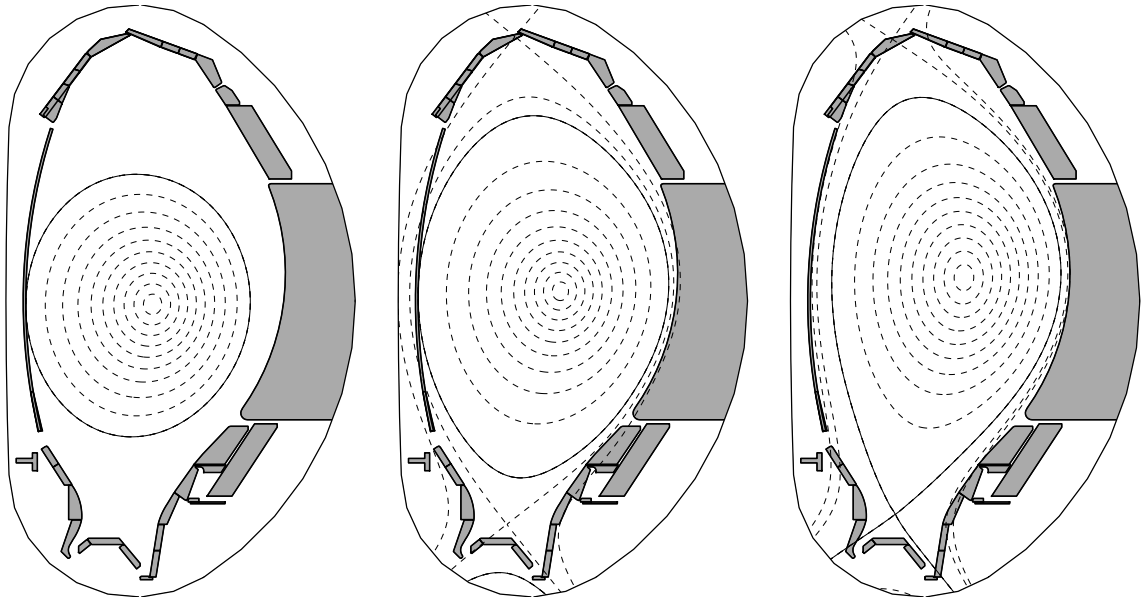

a) Limiter configuration. b) Limiter configuration with divertor coils. c) Divertor configuration.

Figure 1.2: Poloidal cross section of typical magnetic flux surfaces in ASDEX Upgrade in 1.2a) limiter configuration, 1.2b) limiter configuration with divertor coil currents and 1.2c) divertor configuration.

Tokamaks with a divertor configuration achieve better confinement than those with a limiter configuration, making the divertor essential for a power plant. The divertor concept has been tested in various devices (e.g. ASDEX, ASDEX Upgrade, D3D, JET, JT-60).

Looking at the geometry of the divertor target, one can distinguish two types, the open and the closed divertor configuration (Figure 1.3). In operation the different divertor closure results in a different divertor density for a given averaged plasma density. A divertor with a higher closure is able to hold/create a higher neutral gas pressure, which is favourable for helium pumping and divertor detachment, which means that the plasma energy and momentum is dissipated by atomic processes prior to reaching the divertor target plates. For future fusion devices (e.g. ITER, DEMO) a closed divertor configuration is foreseen to be able to efficiently remove the helium ash released by the fusion process. The measurements conducted during this thesis were performed in a closed divertor configuration (Divertor IIb) in ASDEX Upgrade and an open configuration at the Joint European Torus (JET in Culham, England) with a bulk tungsten target (fig. 3.3).

The power going into the divertor arrives at the target in a very narrow ($\sim$ mm) toroidal ring, the so called strike line. Due to the small area the power is deposited

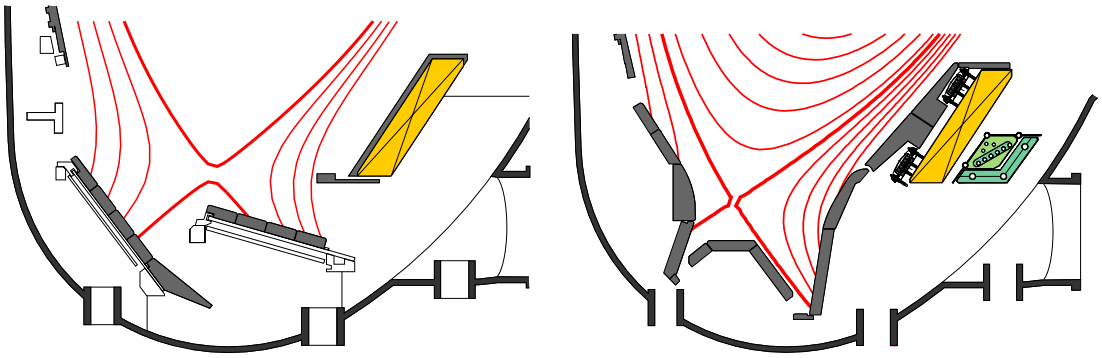

a) Open divertor. b) Closed divertor.

Figure 1.3: Poloidal cross section of the ASDEX Upgrade tokamak with open and closed divertor configuration.

onto the heat flux density [MWm^{-2}] on the target is very high. For future fusion devices such as ITER and DEMO the resulting heat flux would be to high for steady state operation.

Therefore the power flux into the divertor has to be reduced. In order to be able to effectively mitigate the heat flux onto the divertor the underlying transport processes need to be understood. The aim of this work is to study the heat transport in the SOL using heat flux measurements at the outer divertor target. The heat flux is measured using fast high resolution IR thermography.

1.4. ITER and DEMO

The next step fusion devices are ITER and DEMO. ITER is short for **I**nternational **T**hermonuclear **E**xperimental **R**eactor. The goal of this device is to show the possibility to gain more thermal power by fusion than is needed to sustain the fusion process. It is planned that ITER will have a fusion power of 500 MW with an external heating power of 50 MW.

After ITER the next step is to demonstrate the generation of electric power. For this the **DEMO**nstration Power Plant is envisioned which will be only slightly larger than ITER in terms of the machine size. However, DEMO will have a considerably higher fusion gain of around 2 GW, depending on the design. The DEMO design used in this work is the conventional tokamak design DEMO1 of the European Union [7].

With 6.2 m the device will have twice as large major radius than the currently largest device JET. Although the increase in size is comparable to the increase from ASDEX Upgrade to JET, the fusion process itself drastically changes the requirements. With a total power of around 550 MW the thermal load on the wall of the reactor becomes

a serious issue.

Current predictions for the expected loads and life times of the plasma exposed components are based on devices with carbon as wall material. Due to the high tritium retention of carbon it is not suitable for the use in future fusion devices. Therefor the use of metal as wall material is investigated. The wall of ITER will consist of beryllium in the main chamber and tungsten in the divertor.

To test this material composition JET was equipped with the so called ITER-like wall. During this work a database exploiting the technical capabilities of JET was created. For all discharges in the database the target heat fluxes as measured by IR thermography are available, as well as the plasma temperature and density at the edge of the confinement region are available.

In addition discharges at ASDEX Upgrade with the all tungsten wall were conducted to study the heat transport in the divertor.

This data enables the comparison of the energy transport in the SOL with previous studies conducted in carbon devices.

Chapter 2

Thermography

In order to measure the heat flux distribution onto the divertor components the surface temperature evolution is required. In this chapter the measurement of the surface temperature of the divertor target plates using infrared (IR) thermography is described. In the experimental setup the IR emission of the plasma facing components inside the vacuum vessel is measured using IR cameras. From the measured photon flux the surface temperature is determined using Planck's Law (eq. 2.1). The heat flux onto the target plates is derived by solving the heat diffusion equation. As input the measured surface temperature evolution is used. We summaries in this chapter the basics of this method frequently used in fusion devices.

2.1. Planck Radiation

The photon emission of an ideal black body, that is a body that absorbs all incoming electromagnetic radiation, is described by Planck's Law [8, 9]. The spectral radiance which is the emitted power $M^0_\lambda(\lambda, T)$ per area $\mathrm{d}A$ and wavelength interval $\mathrm{d}\lambda$ is given as follows.

$$M^0_\lambda(\lambda, T)\mathrm{d}A\mathrm{d}\lambda = \frac{2\pi hc^2}{\lambda^5}\frac{1}{\exp\left(\frac{hc}{\lambda k_B T}\right) - 1}\mathrm{d}A\mathrm{d}\lambda \qquad \left[\frac{\mathrm{W}}{\mathrm{m}^2\ \mathrm{nm}}\right] \qquad (2.1)$$

Where λ is the wavelength of the emitted photons and T the temperature of the black body. Figure 2.1 shows the spectral radiance for a black body of different temperatures.

The plasma facing components are not ideal black bodies. The ratio between the surface emission and that of an ideal black body is defined as the emissivity ϵ. If ϵ is one, then the emission is that of a black body, if it is zero the surface emits no power.

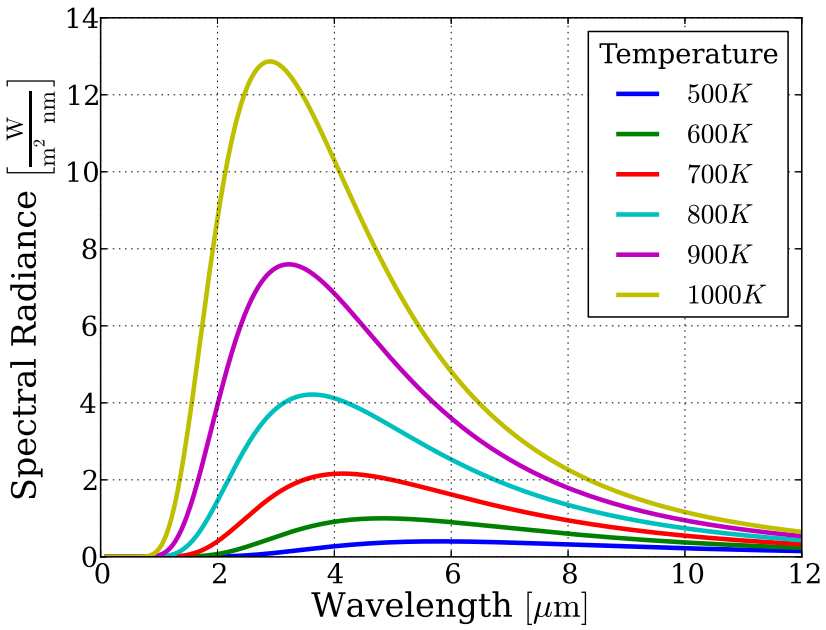

Figure 2.1: Spectral radiance of an ideal black body for different temperatures in dependence on the wavelength.

With this the emission of a surface $I^0_\lambda(\lambda, T)$ can be written as.

$$I^0_\lambda(\lambda, T)\mathrm{d}A\mathrm{d}\lambda = \epsilon\,(\lambda, T)\,\frac{2\pi hc^2}{\lambda^5}\frac{1}{\exp\left(\frac{hc}{\lambda k_B T}\right) - 1}\mathrm{d}A\mathrm{d}\lambda \qquad \left[\frac{\mathrm{W}}{\mathrm{m}^2\ \mathrm{nm}}\right] \tag{2.2}$$

Note here, that the emissivity ϵ depends on the surface temperature T and the wavelength λ. The IR cameras used in the experiments count photons and therefore it is convenient to calculate the photon flux Γ by dividing the emitted power by the energy of a photon E_γ.

$$E_\gamma = \frac{hc}{\lambda} \tag{2.3}$$

$$\Gamma^0_\lambda(\lambda, T)\mathrm{d}A\mathrm{d}\lambda = \epsilon\,(\lambda, T)\,\frac{2\pi c}{\lambda^4}\frac{1}{\exp\left(\frac{hc}{\lambda k_B T}\right) - 1}\mathrm{d}A\mathrm{d}\lambda \qquad \left[\frac{1}{\mathrm{s}\ \mathrm{m}^2\ \mathrm{nm}}\right] \tag{2.4}$$

Equation 2.4 describes the number of photons emitted by a surface with the temperature T per surface area dA and wavelength intervall $d\lambda$ of the photons.

2.2. IR Thermography

Using equation (2.4) one can calculate the photon emission of a surface for a given temperature T. In the experiment the IR camera is equipped with spectral filters, to reduce the amount of photons reaching the detector preventing saturation and to

narrow down the spectral range $\mathrm{d}\lambda$ to reduce aberration effects of the optics. In addition to the transmission curve of the filter, the transmission curves of the vacuum windows and the lens system have to be taken into account. Together with the spectral sensitivity of the detector one can calculate the spectral response function $R(\lambda)$ of the camera system. Using this function the expected photon flux $\Gamma(T)\mathrm{d}A$ from the surface is calculated:

$$\Gamma(T)\mathrm{d}A = \int_0^\infty R(\lambda)\epsilon(\lambda,T)\frac{2\pi c}{\lambda^4}\frac{1}{\exp\left(\frac{hc}{\lambda k_B T}\right)-1}\mathrm{d}A\mathrm{d}\lambda \qquad \left[\frac{1}{\mathrm{m^2\ nm}}\right] \tag{2.5}$$

In order to calculate the photon flux $\Gamma(T)$ to the detector, one has to know the solid angle $\mathrm{d}A$ of the camera system. This has been obtained by comparing the expected photon flux with the measured photon flux of a hot source with known emissivity ϵ. In this case a cavity radiator was used.

2.2.1. Temperature Sensitivity

In the experiments conducted in this thesis the wavelength range used for the measurement of the surface temperature was chosen to be between $4 - 4.5$ µm.

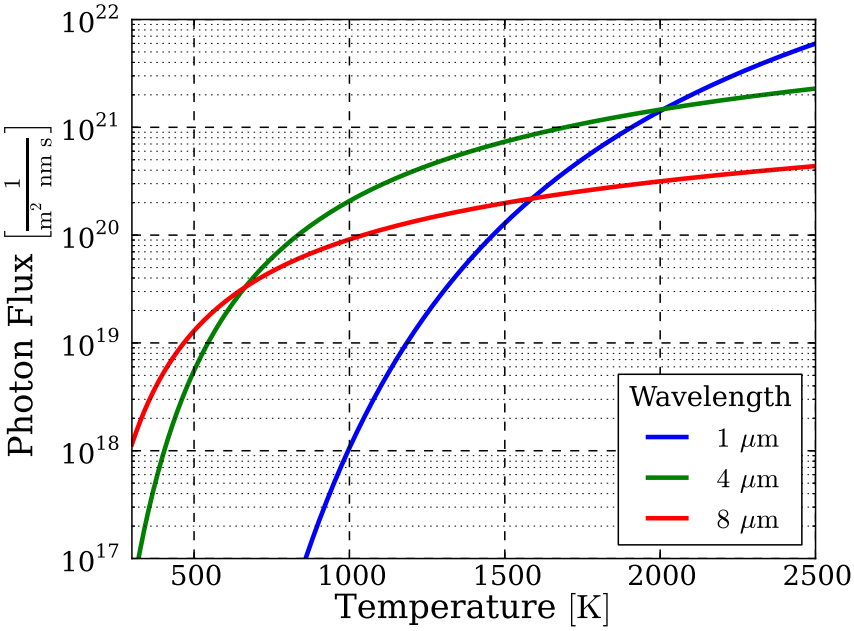

Figure 2.2: Photon flux for an ideal black body in dependence of the temperature of different photon wavelengths.

Figure 2.2 shows the photons flux of an ideal black body as function of the temperature for three different wavelengths (1, 4 and 8 µm). The photon flux exhibits a different behaviour depending on the wavelength range. For 1 µm (blue) the photon flux is low

at low temperatures but increases strongly for high temperatures ($T > 1000$ K). It is obvious that this wavelength is not suited for the measurement at low temperatures but is usable at high temperatures. IR systems measuring in this wavelength region are used, however, for machine protection where only high temperatures have to be detected. Typically relatively cheap uncooled near infrared (NIR) detectors are used.

For a wavelength of 4 µm (green) the photon flux has a relatively strong increase over the whole temperature range between $300 - 2500$ K. This wavelength region was chosen for the measurements to have a good coverage over the whole divertor temperature range expected in ASDEX Upgrade and JET ($400 - 2500$ K). Medium wavelength IR (MWIR) detectors measuring in this wavelength range require active cooling to temperatures of around 70 K which increases the complexity of the detector system and the vulnerability against external perturbations such as strong magnetic fields. These factors increase the costs of the IR systems.

At long wavelengths (LWIR) of around 8 µm (red) the photon flux increases stronger than for the MWIR measurement (green) for low temperatures. At higher temperatures ($T > 700$ K) this trend is reversed and the photon flux increases slower than for 4 µm. An IR system measuring in this wavelength region is well suited to measure at comparably low temperatures. This wavelength region can be used for the measurement of low heat fluxes which induce only a small temperature increase. On small devices (e.g. MAST, Compass-D, ...) where a short pulse length ($t < 1$ s) limits the expected temperature increase to < 500 K such a system would be more suited than a system measuring at 4 µm.

2.2.2. Observational Error

In this section sources for errors in the IR measurement are discussed. IR thermography derives the surface temperature T from a measured photon flux Γ. Any external source contributing to this photon flux will result in an overestimated surface temperature, any process reducing the photon flux results in an underestimated temperature. Assuming that the transmissions of the optical path are well known, only contributions increasing the photon flux will be discussed.

Reflections

One source for an additional photon flux is the reflection of photons originating from other regions from the observed target surface. The influence of reflection is especially large for metallic surfaces which have a low emissivity and a high reflectivity.

Figure 2.3 shows the influence of reflections on a typical temperature profile observed

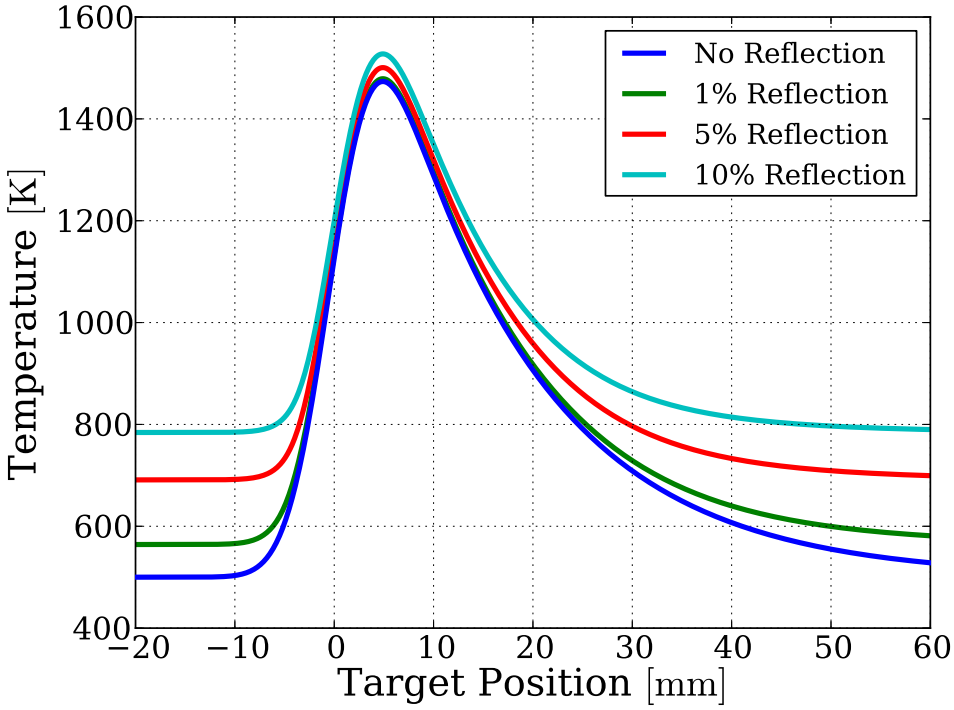

Figure 2.3: Evaluated temperature profiles using synthetic IR data with different levels of an assumed background photon flux due to reflections.

on the divertor target in tokamak devices. The unperturbed temperature profile is shown in blue. From this the expected photon flux is calculated for an IR system measuring at 4 µm as used in ASDEX Upgrade and JET. To this photon flux profile a constant photon flux of 1, 5 and 10 % of the peak photon flux of the profile are added. From the resulting photon flux profiles the surface temperature is derived.

For high temperatures the error induced by reflections is small. For low temperatures where the measured photon flux is low the impact of reflections is large. The surface temperature is overestimated significantly by a moderate excessive signal of 10 % only.

One method to quantify the degree of reflections in the experiment is a global energy balance. Here the injected energy W_{in} is balanced against the energy emitted by the plasma W_{out}. The injected energy is calculated by integrating the heating power P_{heat} over the discharge. The radiated energy W_{rad} can be measured by bolometers or thermocouples in the tiles of the first wall. Together with the measurement of the divertor losses from the IR thermography. W_{IR}, those energies have to balance each other.

$$W_{in} = W_{rad} + W_{IR} \qquad \text{[MJ]} \qquad (2.6)$$

Subtracting a constant fraction of the measured photon flux changes the derived temperature and therefore the measured deposited energy W_{IR}. With this the influence of

reflections can be quantified in the experiment.

For ASDEX Upgrade and JET with carbon plasma facing components it was found that reflections do not influence the measurement significantly. A slight increase of the measured surface temperature due to reflections was only found for the far SOL and private flux region where the surface temperature remains comparably low during the discharge. For the studies conducted in this thesis the influence of reflections is neglected.

Volume Radiation

In the experiment the IR systems observe the divertor target where the plasma touches the wall. The plasma and excited neutral particles in the divertor are emitting photons. In case of the JET IR system the divertor target at the bottom of the machine is observed from the top of the machine through the confined plasma.

If the density of the plasma/neutrals is high enough the emitted photons can contribute significantly to the measured photon flux. The influence on the measured profile is similar to the influence by reflections described in the previous section.

The optimal way to handle the influence of radiation is to choose the observed wavelength region in such a way to avoid line radiation and reduce bremsstrahlung. For the measurement at 4 µm no influence of line radiation was observed in either ASDEX Upgrade or JET except for detached conditions. In case of bremsstrahlung a low additional photon flux has been observed for discharges with very high divertor density. Those discharges are not part of the discussions in this thesis and therefore radiation is not considered in the evaluation of the surface temperature.

2.3. Heat Flux Measurement

Having measured the surface temperature evolution $T(s,t)$, where s is the coordinate along the surface of the target, the heat flux density $q(s,t)$ onto the target is calculated. This is done using the THEODOR code [10, 11], which solves the 2D heat diffusion equation in the poloidal cross-section of the divertor target tiles:

$$\rho c_p \frac{\partial T}{\partial t} = \nabla \kappa \nabla T \tag{2.7}$$

Where κ is the heat diffusivity, ρ the material density and c_p the specific heat capacity. The THEODOR code solves the heat diffusion equation using the measured surface temperature evolution $T(s,t)$ as boundary condition. This is done to obtain informa-

tion about the temperature distribution inside the tile. Which is necessary to obtain the correct heat flux. The THEODOR code uses an explicit solving scheme, for further details refer to appendix B.

2.4. Heat Transfer Coefficient

In the calculation of the heat flux onto the target, the heat diffusion equation is solved for every time step of the measurement, using the measured surface temperature T_{surf} as a boundary condition. The heat flux onto the target can be obtained using the heat transfer coefficient α using the following equation.

$$q = \alpha(T_{surf} - T_{bulk}) \qquad \left[\frac{\mathrm{W}}{\mathrm{m}^2}\right] \tag{2.8}$$

$$[\alpha] = \frac{\mathrm{W}}{\mathrm{m}^2\ \mathrm{K}} \tag{2.9}$$

Where T_{bulk} is the temperature of the tile below the surface, estimated by the solution of the heat diffusion equation. Any error in the value of the heat transfer coefficient α is directly influencing the estimated heat flux on the target.

Figure 2.4 illustrates the influence of the heat transfer coefficient α on the evaluation of the heat flux using a transient heat flux event measured in JET on the outer target made of bulk tungsten(fig. 3.3). In phases where the heat flux onto the target changes quickly, e.g. the onset of the ELM, the measured heat flux increases with the value of α used for the evaluation. After the ELM the heat flux drops faster for larger α values. In order to draw conclusions about the heat flux on the target, the value of the heat transfer coefficient α needs to be known. The experimental determination of α for the targets of the ASDEX Upgrade and JET divertors at the high heat flux test facility GLADIS is presented in section 2.5.

Possible imperfections in the surface morphology can lead to an overestimation of the surface temperature by IR thermography [12]. For the calculation of the heat flux, the surface temperature can be corrected using the following relation:

$$T_{surf} = T_{IR} - \frac{q}{\alpha_{surf}} \qquad [\mathrm{K}] \tag{2.10}$$

If the target plate consists of bulk material which is coated with a surface layer (e.g. tungsten coated CFC), then the heat transfer coefficient $\alpha_{coating}$ of the coating is cal-

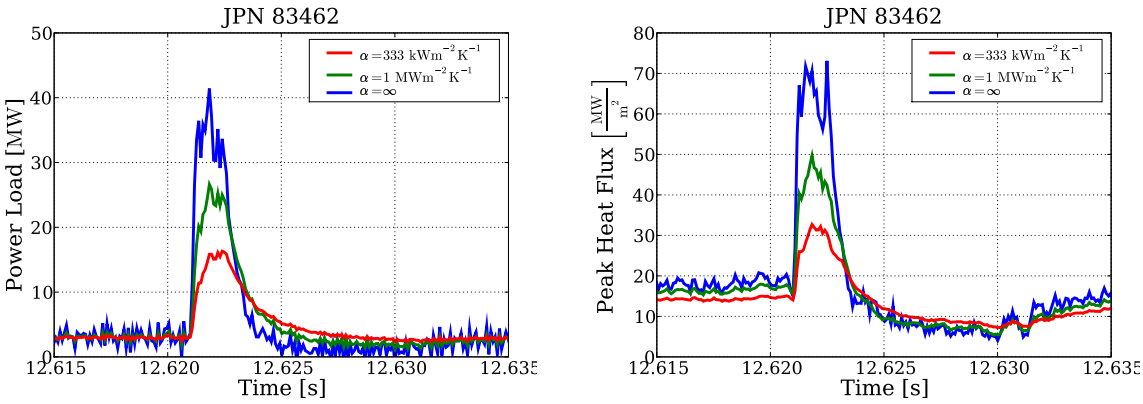

a) Power load. b) Peak Heat Flux.

Figure 2.4: Example of the influence of the heat transfer coefficient α on the measured target heat flux using the example of a discharge in JET with a bulk tungsten outer target.

culated as follows.

$$\alpha_{coating} = \frac{\kappa}{d} \qquad \left[\frac{\mathrm{W}}{\mathrm{m^2\ K}}\right] \tag{2.11}$$

Where κ is the heat conductivity and d the thickness of the coating, while the contact of the coating with the bulk is assumed to be perfect.

2.5. Experimental Determination of α

For the experimental determination of the heat transfer coefficient α of the divertor targets, observed in ASDEX Upgrade and JET, the high heat flux test facility GLADIS was used (Chapter 3.3). The different divertor target plates were exposed to short well defined heat flux pulses and the temporal response of the surface temperature was measured using pyrometers and IR cameras. The measurements were conducted for different target plates. For JET the bulk tungsten target and two CFC targets with 11 and 20 µm tungsten coating were used. For ASDEX Upgrade a tungsten coated fine grain tile and a bulk tungsten target [13] was used.

Figure 2.5 shows the heat flux density on the target for a GLADIS pulse with 5 ms duration. The two spikes at the beginning and the end of the pulse are not real but artifacts from the measurement caused by the neutral beam extraction voltage on the earthing for the experiment hall. The optimum preset pulse form would be rectangular, but here the heat flux takes some time to build up in the beginning of the pulse. This delay is caused by the electrical setup of the neutral beams power supply and accounts to about 1 ms. The typical ELM duration observed in JET with the ITER-like wall is

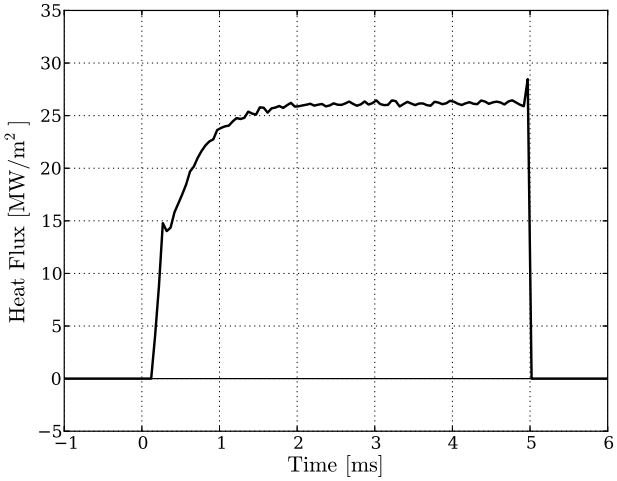

Figure 2.5: Temporal evolution of the target heat flux for a GLADIS pulse with 5 ms duration.

around 2 ms. For the experiments, pulse durations of 5, 10, 25 and 50 ms have been used. Shorter time durations of 2 ms have been attempted but were not successful. The shortest pulses used for this experiment are comparable to ELMs observed in JET.

In the evaluation of the heat flux $q(s,t)$, the heat transfer coefficient α acts as a dampening term. This can be understood if one looks at the effective temperature response T_{IR} resulting from a finite α (Equation 2.10). The observed temperature T_{IR} for a given heat flux q is increased in presence of a finite heat transfer coefficient α. In the deduction of the heat flux from the temperature time series, α has the opposing effect. For a rising (falling) heat flux, the estimated heat flux is reduced(increased).

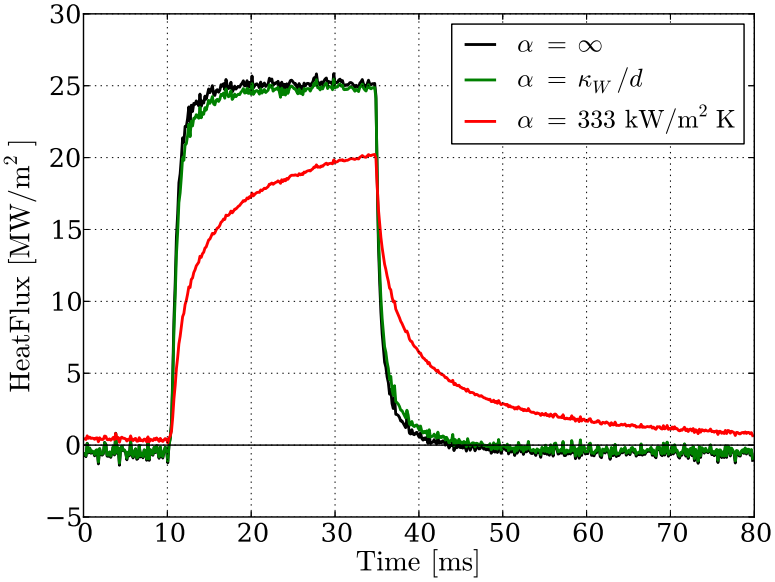

Figure 2.6: Evaluated heat flux for a 25 MW GLADIS pulse of 25 ms duration on a CFC target with a 20 µm tungsten coating, using different assumptions for the heat transfer coefficient α.

Figure 2.6 shows the evaluated heat flux of a CFC target with a 20 µm tungsten coating. In this example three different heat transfer coefficients have been assumed. The theoretical model $\alpha = \kappa_W/d$ (eq. 2.11), where κ_W is the heat conductivity and d the thickness of the tungsten layer, and the assumption that no layer is existent ($\alpha = \infty$) show little difference. This is expected because for the specified pulse the temperature correction is less than 2 percent of the temperature rise during the pulse. This is found to be true also for the tungsten coated fine graphite tiles used in ASDEX Upgrade. For the bulk tungsten tiles used in JET and for the new bulk tungsten divertor in ASDEX Upgrade no correction of the measured surface temperature was necessary to reproduce the heat flux pulses.

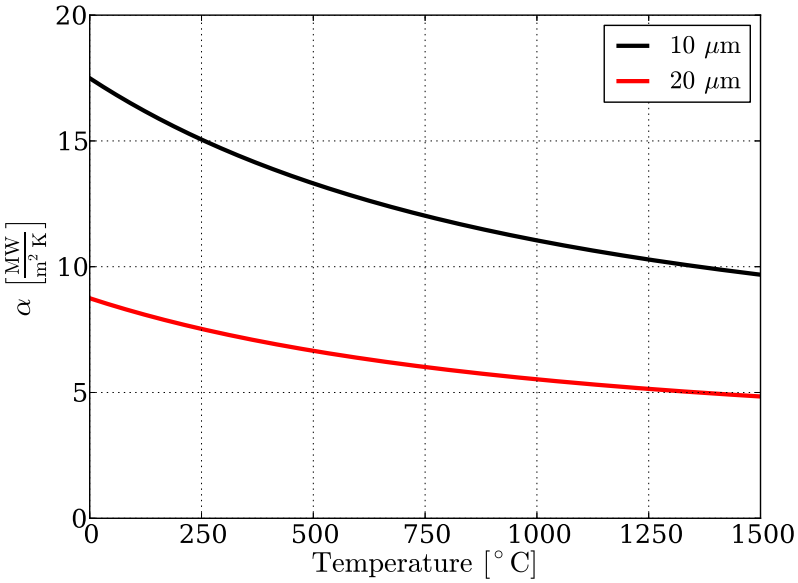

Figure 2.7: Heat transfer coefficient α for a tungsten coating with 10 and 20 µm.

The case with $\alpha = 333\,\mathrm{kW/m^2}$ has been included in figure 2.6 to show the influence of an underestimated α on the evaluation of the heat flux density. The rise and fall of the peak are not reproduced if α is too small. Furthermore it can be seen, that the absolute value of the peak heat flux is underestimated. This plays an important role if transient heat loads between discharges with different target materials are compared.

Note here that independent on the choice of α, the THEODOR code is energy conserving. This can be seen in the case with underestimated heat transfer coefficient α in figure 2.6 (red). During the pulse, the energy input is underestimated and after the pulse, the heat flux only gradually approaches zero and the *missing* energy is *deposited* on the target. For the comparison of transient heat loads between different machines this fact can be utilised if the exact α is unknown, by comparing the deposited energy fluency ϵ and choosing the integration interval sufficiently long to extent beyond the

transient event.

$$\epsilon(s) = \int_{t_0}^{t_1} q(s,t)dt \qquad \left[\frac{\mathrm{kJ}}{\mathrm{m}^2}\right] \tag{2.12}$$

Where t_0 is the beginning and t_1 the end of the integration interval. In the experiment the integration times are chosen in a way that the power load in the time interval is above $1/e$ of the peak power load of the transient event. In this section the validation of the heat flux evaluation using GLADIS pulses has been shown. Using the results for bulk tungsten and tungsten coated CFC and graphite, one is able to evaluate the peak heat flux of transient heat fluxes. Note that this validation does not cover deposited layers as observed on carbon surfaces [14]. Those layers are more difficult to asses because they develop and change during tokamak operation near the strike line, where no calibrated heat flux source is available.

Chapter 3

Experiments

In this chapter the experiments and diagnostics used for this thesis will be described. The measurements were obtained at the divertor tokamaks ASDEX Upgrade and JET. In addition experiments at the high heat flux test facility GLADIS were performed to validate the heat flux measurements obtained in both tokamaks.

		ASDEX Upgrade	**JET**	**ITER**
$\mathbf{R}$	[m]	1.65	3.2	6.2
$\mathbf{a}$	[m]	0.5	1.0	2.0
$\mathbf{B_{tor}}$	[T]	3.2	4.0	5.6
$\mathbf{I_p}$	[MA]	1.2	3.5	15

Table 3.1.: Major, minor radius, maximum toroidal magnetic field at the torus axis and maximum plasma current for ASDEX Upgrade, JET and ITER.

3.1. ASDEX Upgrade

ASDEX Upgrade (**A**xial **S**ymetric **D**ivertor **Ex**periment **Upgrade**) is a divertor tokamak in Garching, Germany, which is operated by the Max-Planck Institute for Plasma Physics since 1991. The plasma torus has a major radius of 1.65 m and a minor radius of 0.5 m. The plasma pulse length is around 10 s with a maximum external heating power of about 30 MW. The device has different heating systems available, the main contribution of 20 MW is held by neutral beam injection (NBI). In addition two wave heating systems are installed. Ion cyclotron resonance heating (ICRH) delivers up to 6 MW to the plasma and 4 MW of electron cyclotron resonance heating are installed.

ASDEX Upgrade started operation with carbon plasma facing components. Then it was successively changed into a tungsten device [15] and was the first tokamak to

demonstrate operation with a full tungsten wall in 2007 [1]. The possibility to operate a fusion device with a metal plasma facing components is important for the development of a fusion power plant. Tritium is a radioactive isotope of hydrogen which due to the short half-life of around 12.6 years has a high activity. Relatively small amounts of tritium ($\sim$ 700 g) are sufficient to exceed the safety limit set for the operation of a nuclear site [16, 17]. Since hydrogen and therefore also tritium chemically react with carbon, carbon plasma facing components are deemed inapplicable for the use in large fusion devices as they form hydrocarbon molecules deposited in the vessel and pumping systems.

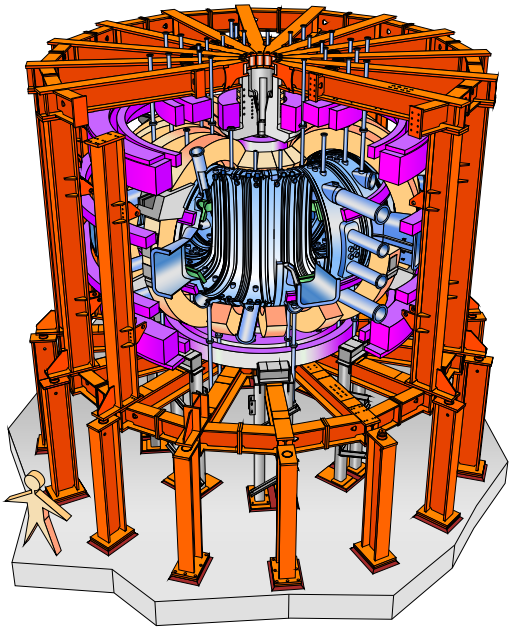

Figure 3.1: Cut away drawing of the ASDEX Upgrade tokamak [18].

3.1.1. Thermography

ASDEX Upgrade is equipped with several infrared (IR) diagnostics to observe the heat flux onto various parts of the divertor and first wall. The main diagnostics used are a fast 1D system observing the lower inner and outer divertor target and a fast 2D system observing the lower outer divertor target. For a detailed description of IR thermography refer to chapter 2.

1D System

The fast 1D IR system observes the lower inner and outer divertor target through a relay optic mounted at the bottom of the device. The detector is a 256 pixel line array with 12 bit resolution measuring in a wavelength range of $4 - 5.5$ µm. The smallest

achievable readout time for one line is 130 µs resulting in an effective sample rate of about 7.7 kHz. The integration time and the readout time are the same for this system meaning that the chosen sample rate sets the integration time.

2D System

The fast 2D IR system used in this thesis observes the outer divertor target from the outer mid plane using a mirror inside the vacuum vessel. The IR detector has an image format of 320x240 pixels with 14 bit resolution and a maximum achievable frame rate of up to 25 kHz for a small subframe. For the operation at ASDEX Upgrade with a spatial resolution on the target of about 1.3 mm per pixel the usable frame rate is reduced to about 7.3 kHz.

In contrast to the 1D system the integration time can be chosen independent of the frame rate. This adds flexibility to the system especially for discharges with high surface temperatures where a too long integration time would result in saturation of the detector.

3.1.2. Langmuir Probes

ASDEX Upgrade is equipped with a multitude of Langmuir probes for the measurement of the plasma density and temperature in front of the target tiles. Langmuir probes measure the current I which is drawn from the plasma in dependence on the voltage V that is applied to the probe [19]. For the measurement of the characteristic curve of the current a voltage ramp is used.

From the measurement of the $I - U$ characteristic several quantities can be deduced. In the boundary volume where the plasma touches the wall the so called sheath forms. Due to the higher mobility of the electrons compared to the ions the electrons induce a negative charge on the target. This charge creates a potential difference between the plasma and the wall which is called the plasma potential.

A strong negative voltage on the probe will repel the electrons and if the voltage is high enough only ions will be able to reach the probe. The ions will satisfy the Bohm criterion so that their velocity will be equal to the ion sound speed at the sheath edge.

$$c_s = \sqrt{\frac{ZT_e + \gamma_i T_i}{m_i}} \qquad \left[\frac{\mathrm{m}}{\mathrm{s}}\right] \tag{3.1}$$

Where T_e the electron temperature, T_i the ion temperature, m_i the ion mass and γ_i the adiabatic coefficient for the ions. Assuming quasi-neutrality the charge density is

given as en_e and the ion current density is given as:

$$j_i^{sat} = en_e c_s \qquad \left[\frac{\mathrm{A}}{\mathrm{m}^2}\right] \tag{3.2}$$

Knowing the surface area of the probe S the current on the probe is calculated as:

$$I_i^{sat} = S j_i^{sat} = S e n_e c_s \qquad [\mathrm{A}] \tag{3.3}$$

A further increase of the voltage will not increase the measured current. Therefore the current I_i^{sat} is called the *ion saturation current*.

Applying a strong positive voltage to the probe will lead to a similar behaviour but now the ions are repelled and the electrons carry the current. The corresponding *electron saturation current* in the probe is again calculated using the probe surface S.

$$I_e^{sat} = S e n_e \sqrt{\frac{T_e}{2\pi m_e}} \qquad [\mathrm{A}] \tag{3.4}$$

When the voltage applied to the probe is changed from strong negative to positive, then the current in the probe is a superposition of the current carried by the ions and the electrons. For the electron current the following relation was found.

$$I_e(U) = -S e n_e \sqrt{\frac{T_e}{2\pi m_e}} \exp\left(\frac{e\left(\Phi_p - U\right)}{T_e}\right) \qquad [\mathrm{A}] \tag{3.5}$$

Where Φ_p is the *plasma potential*. The total current I_{tot} on the probe is the sum of the ion saturation I_i^{sat} current and the electron current $I_e(U)$.

$$I_{tot}\left(U\right) = I_i^{sat} + I_e\left(U\right) \qquad [\mathrm{A}] \tag{3.6}$$

On the characteristic curve there exists one point where there is no current in the probe.

$$I\left(U_{fl}\right) = 0 \qquad [\mathrm{A}] \tag{3.7}$$

The potential at which this point lies is called the *floating potential*. For the measurement of the electron temperature T_e and electron density n_e three points on the characteristic are needed. Further assumptions are that the electron and ion temperature at the sheath edge are equal $T_e = T_i$ and the adiabatic coefficients are assumed to be $\gamma_i = 3$ and $\gamma_e = 1$.

For the first point a voltage is chosen to measure the ion saturation current.

$$I_1(U_1) = I_i^{sat} \qquad [\mathrm{A}] \tag{3.8}$$

The voltage of the second point is chosen in a way that the current in the probe is the negative ion saturation current.

$$I_2\left(U_2\right) = I_i^{sat} + I_e\left(U_2\right) = -I_i^{sat} \qquad [\mathrm{A}] \tag{3.9}$$

The third point is at the floating potential where the probe measures no current.

$$I_3\left(U_{fl}\right) = I_i^{sat} + I_e\left(U_{fl}\right) = 0 \qquad [\mathrm{A}) \tag{3.10}$$

Using the expressions for the ion saturation current (eq. 3.3) and the electron current (eq. 3.5) the electron temperature and the electron density are derived.

$$T_e = \frac{e\left(V_2 - V_3\right)}{\ln 2} \qquad [\mathrm{eV}] \tag{3.11}$$

$$n_e = \frac{I_i}{eS\sqrt{\frac{3T_i+T_e}{m_i}}} \qquad \left[\frac{1}{\mathrm{m}^3}\right] \tag{3.12}$$

3.2. JET

JET (**J**oint **E**uropean **T**orus) is a tokamak in Culham, UK. Since 2000 it is operated by the Culham Center for Fusion Energy (CCFE). It has a major radius of 3.2 m and minor radius of 1.0 m. JET started as a limiter tokamak in 1983 and was converted to a divertor tokamak in 1993. From 2009 - 2011 the inner wall of the machine was changed from CFC plasma facing components to an ITER-like design, with beryllium in the main chamber and tungsten in the divertor. For the heating of the plasma several external heating systems are installed with a total heating power of up to 49 MW. The main heating system is NBI heating with 32 MW of installed heating power. In addition 10 MW of ICRH and 7 MW of lower hybrid (LH) heating are installed. For the wave heating systems the effective heating power is reduced due to reduced coupling efficiency especially in H-mode discharges.

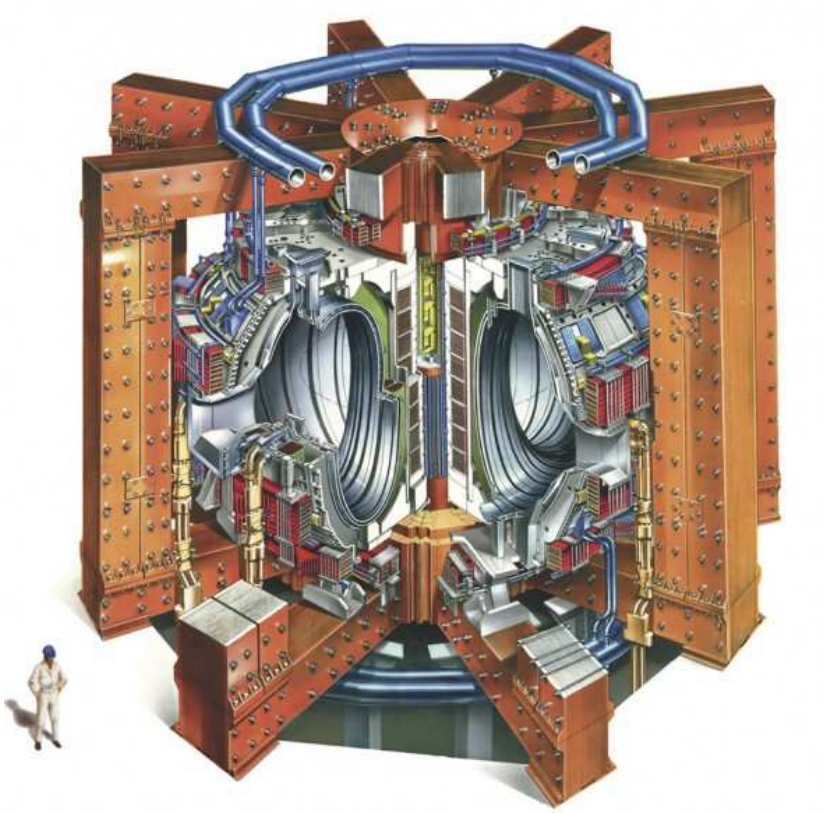

Figure 3.2: Cut away drawing of the Joint European Torus (JET) tokamak [6].

3.2.1. Divertor

Originally JET had been designed as a limiter tokamak. In contrast to other tokamaks at that time the toroidal field coils were not circular but D shaped. After ten years of operation with limited plasmas, JET has been equipped with a divertor. Opera-

tion with the divertor started in 1993. In the progress a variety of different divertor geometries have been tested in JET leading to the current design (fig. 3.3).

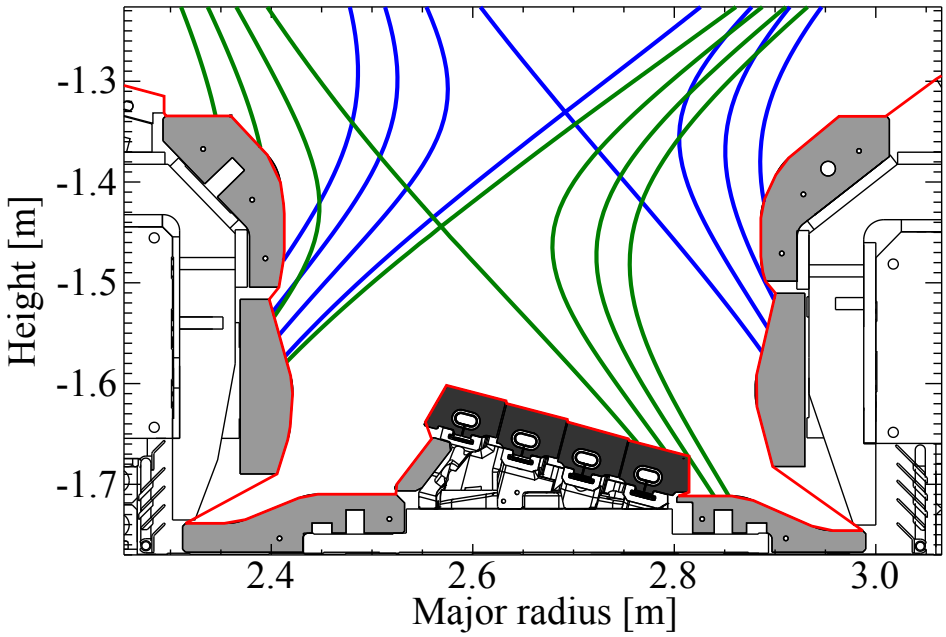

Figure 3.3: Sectional view of the divertor in JET-ILW, with tungsten coated CFC (light gray) and bulk tungsten (dark gray) plasma facing components. Open (green) and closed (blue) divertor configurations are indicated by exemplified magnetic equilibria.

The current divertor design allows the operation in two different configurations. Using the vertical inner and outer target a closed divertor configuration can be established (blue). An open configuration can be achieved using the inner vertical and outer horizontal target (green).

Since 2011 JET is equipped with the so called ITER-like wall (JET-ILW), which uses beryllium in the main chamber and tungsten coated CFC (light gray) and bulk tungsten (dark grey) in the divertor.

The change from CFC plasma facing components to the full metal wall was done to test this particular material mix for ITER which will also use beryllium in the main chamber and tungsten in the divertor. The bulk tungsten target in JET-ILW is not designed as one solid tungsten tile, but consists of four stacks of 24 separate lamellae. To span the whole toroidal circumference 96 tiles are installed. The temperature and heat flux measurements from JET-ILW shown in this thesis were taken on this bulk tungsten target.

3.2.2. Thermography

For thermography four 2D IR detectors [20] are installed at JET. Two detectors are installed in the mid plane, one observing the inner and outer vertical divertor targets and the other giving an overview of the main chamber. The other two detectors are

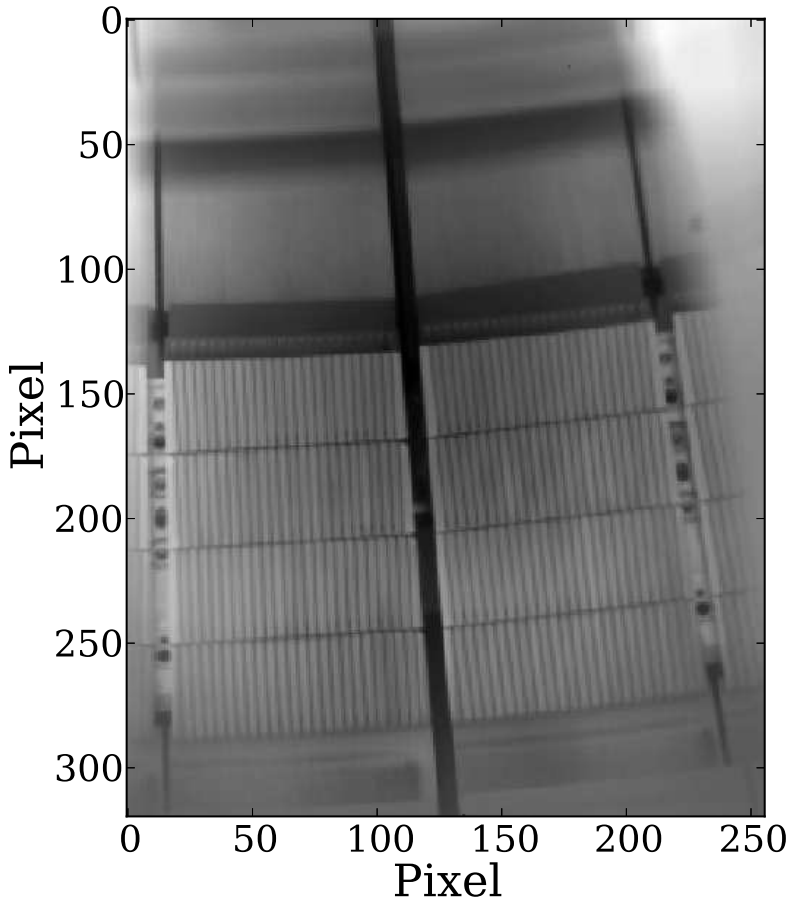

Figure 3.4: View of the IR system from the top of the machine. The castellated bulk tungsten target (fig. 3.3) is clearly visible.

positioned on top of the machine observing the horizontal bulk tungsten target on the bottom of the machine. The systems observing the horizontal divertor target are positioned at a toroidal angle of 135° in respect to each other. For the discussion in this thesis only the two top mounted cameras are used which have an image format of 320×256 pixel with a resolution of 14 bit. Both systems have a spatial resolution of about 1.6 mm on the target and can achieve frame rates of up to 20 kHz.

3.2.3. Thomson Scattering

For the measurement of the electron temperature and electron density in the plasma a **H**igh **R**esolution **T**homson **S**cattering (HRTS) system is installed at JET [21]. The

elastic scattering of light on free electrons is called Thomson scattering. In the diagnostic a high energy laser beam is passed through the plasma and the scattered light is detected. The high laser energy is needed because the scattering efficiency is very small.

The spatial resolution of the system is 15 mm over a radial range from $R = 2.9 - 3.9$ m. The laser source is a 5 Joule Nd:YAG laser with a repetition rate of 20 Hz.

3.3. GLADIS

GLADIS (**G**arching **La**rge **Di**vertor **S**ample Test Facility) is a high heat flux (HHF) test facility in Garching, Germany, which is operated by the Max-Planck Institute for Plasma Physics. It is capable of exposing large divertor samples with a heat flux between 3 and 55 MW/m^2 with steady state or pulsed operation [22]. GLADIS consists of a cylindrical vacuum vessel in which the sample is positioned. The heat flux source consists of two neutral beam injectors similar to the heating beams used at ASDEX Upgrade and JET. A picture of GLADIS is shown in figure 3.5a).

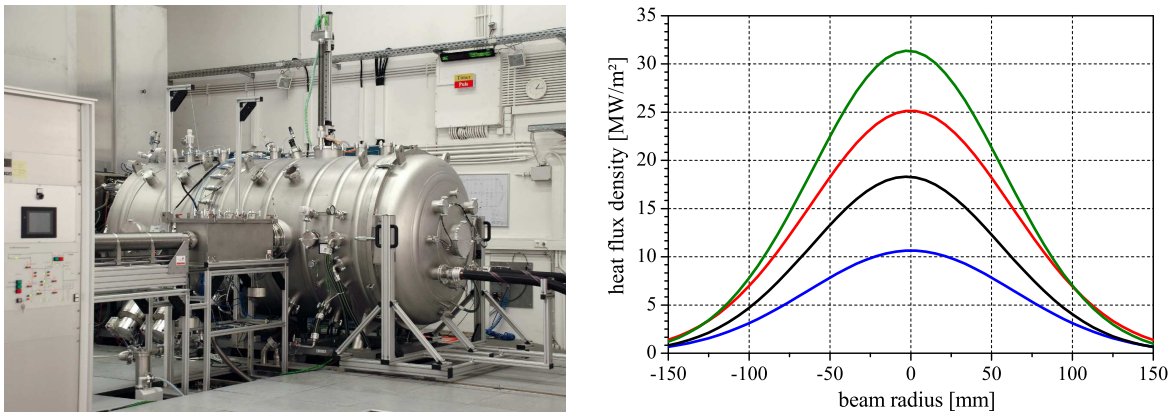

a) GLADIS b) Heat flux density profiles.

Figure 3.5: Picture of the HHF test facility GLADIS and examples of achievable heat flux density profiles on the target [22].

Figure 3.5b) shows examples of heat flux densities achievable in GLADIS. The heat flux profiles have a Gaussian shape with a profile with of around 70 mm.

For the measurements conducted during this thesis only one ion source was used giving a peak heat flux of about 25 MW/m^2 corresponding to the red profile in figure 3.5b). The goal of the experiments at GLADIS was to determine the heat transfer coefficient α for different divertor target materials. Therefore the targets were exposed to short well defined periodic heat flux pulses. The surface temperature response was measured using both pyrometers and a fast IR camera. The IR camera used is the same as used at ASDEX Upgrade (Section 3.1.1).

Figure 3.6 shows two JET-ILW bulk tungsten lamellae before and after heat flux exposure in GLADIS. The lamellae were mounted in a tungsten coated CFC mounting. It is seen that the beam also deposits energy onto the mounting. The pyrometers were aligned in a way only to measure on the surface of the lamellae. For the evaluation of the fast IR camera only regions observing the lamellae were used.

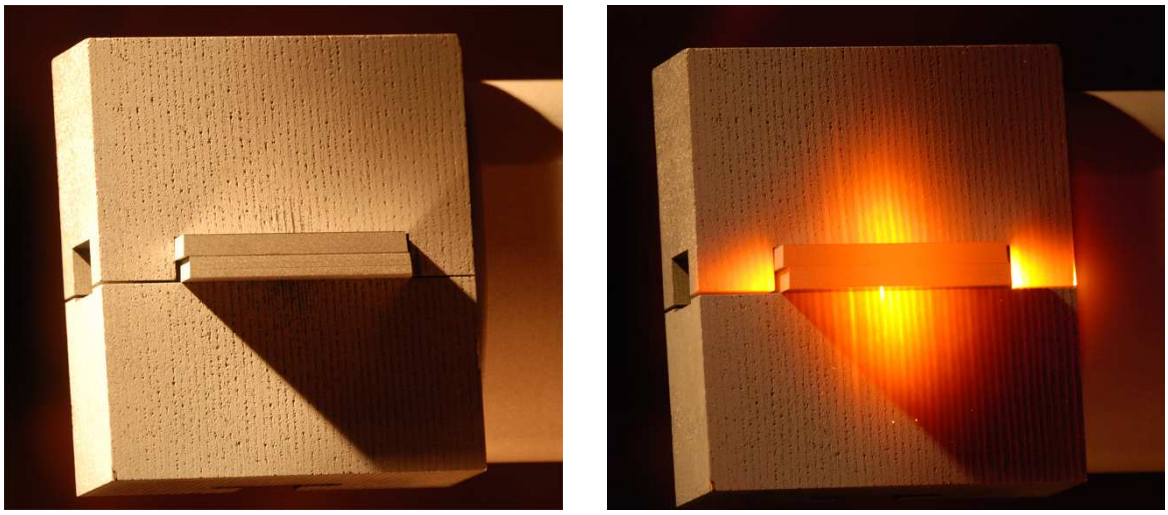

a) Before b) After

Figure 3.6: Visible-light images of two JET-ILW bulk tungsten lamellae in a tungsten coating CFC mounting before and after heat flux exposure in GLADIS.

Chapter 4

Power Exhaust

In this chapter a general overview over tokamak power exhaust is given. The power balance for steady state operation of a fusion device is discussed. A model for the measured heat flux profile on the target is presented. Using ITER as an example the critical quantities for the power exhaust are shown. The power load onto the first wall is estimated and limits for the mitigation of the divertor power load are elaborated. The two point model (Section 4.4) is introduced and used to discuss the influence of the heat diffusion in the divertor on the temperature distribution in the SOL. The necessary heat diffusion in the divertor for safe steady state operation is estimated.

4.1. Power Balance

During operation of a fusion device the plasma constantly loses energy. This energy loss has to be compensated to assure continuous plasma operation. The heating in a large fusion device like ITER or DEMO consists of two main contributions. The first one is heating by external heat sources such as neutral beam injection (NBI), electron cyclotron resonance (ECRH) and ion cyclotron resonance (ICRH) heating. For the following consideration the source of external heating is irrelevant and all heating methods are combined to the auxiliary heating power P_{aux}. The second contribution to the plasma heating is the fusion process itself. 20 % of the energy released by fusing deuterium and tritium are transfered to the resulting helium nucleus, also called α-particle. The α-particles interact with the plasma by collisions, transferring energy to the plasma. This contribution to the heating of the plasma is denominated with P_α. The remaining 80 % of the fusion energy are transfered to the neutrons. Since neutrons carry no electric charge they don't interact with the magnetic field inside the tokamak and can exit the confined plasma unhindered. The neutrons hit the wall of the tokamak an are stopped in the so called *blanket*, inducing a uniform power load

P_n.

Another power loss channel of the plasma is radiation. The radiation has a variety of contributions like line radiation, Bremsstrahlung or synchrotron radiation. The power loss by radiation is denominated as P_{rad}. A further power loss channel is the energy transport of the plasma itself. Important here is the power P_{sep} crossing over the *separatrix* from the confined plasma into the scrape-off layer. The power is carried by the plasma itself and flows along the field lines into the divertor region. This mechanism deposits the energy in a very narrow band (~ 1 cm) onto the divertor target plates. The resulting target power deposition process is the main focus of this thesis.

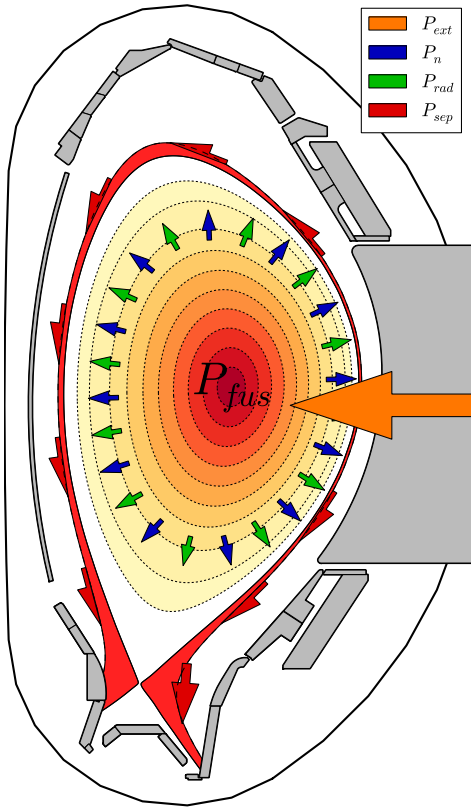

Figure 4.1: Depiction of the power fluxes inside a tokamak.

Summing up all these contributions the total power balance is written as:

$$P_{aux} + P_{fus} = P_n + P_{rad} + P_{sep} \tag{4.1}$$

Where P_{fus} is the total fusion power. Removing the neutron contribution from the power balance the plasma power balance can be formulated as:

$$P_{aux} + P_\alpha = P_{rad} + P_{sep} \tag{4.2}$$

For large fusion devices the α particle heating P_α will be the main contribution to this power balance. For ITER with a fusion power of 500 MW the α-particle heating will amount to 100 MW compared to the envisioned external heating power of 50 MW. With 50 MW DEMO is foreseen to have the same auxiliary heating power as ITER while having a significantly higher fusion power of 1790 MW resulting in about 360 MW of α-particle heating. The auxiliary heating power in DEMO is to both ignite the plasma and control the fusion gain during the ignited phase. Table 4.1 shows the heating power envisioned for ITER and DEMO.

	$\mathbf{P_{fus}}$ [MW]	$\mathbf{P_{ext}}$ [MW]	$\mathbf{P}_\alpha$ [MW]	$\mathbf{P}_\alpha/\mathbf{P_{ext}}$
ITER	500	50	100	2
DEMO	1790	50	358	~ 7.2

Table 4.1.: Comparison of the fusion and heating power for ITER and DEMO.

4.2. First Wall Power Load

Considering the power balance (eq. 4.1) the heat load onto the first wall can be estimated. Although the neutrons have no influence on the power balance of the plasma they cannot be neglected in the design of the devices. For a device like ITER where 500 MW of fusion power are envisioned, the neutrons carry 400 MW of power. This power is distributed onto the first wall. Assuming a first wall area of 660 m^2 the resulting heat flux density amounts to about 0.6 MWm^{-2}. In this discussion the additional heat generation in the blanket due to neutron activation and the power deposition of the neutrons in the volume of the first wall are neglected. Especially for future power plants (e.g. DEMO) that have both a large neutron flux and a long phases of continuous plasma operation this contribution might not be negligible.

4.3. Divertor Power Load

The remaining 150 MW of loss power are carried by both P_{sep} and P_{rad}. Since the radiative power exhaust also distributes the power about evenly onto the plasma facing components, it would be convenient to have radiative cooling only thus eliminating P_{sep} to mitigate the localised power deposition in the divertor. In reality this is not possible. The foreseen operational scenario for large fusion devices is the so called high confinement mode (H-mode). To reach H-mode an empirical threshold of the transition from L- to H-mode P_{LH} has been found which is based on the power crossing the separatrix P_{sep} [23].

$$P_{LH} = 0.049\, B_{tor}^{0.8}\, \bar{n}_e^{0.72}\, S^{0.94} \qquad \text{[MW]} \tag{4.3}$$

Where B_{tor} is the toroidal field in T, n_e the line averaged electron density in 10^{19} m^{-3} and S the surface of the confined plasma in m. For the foreseen operational point of ITER this results in an LH threshold of about 86 MW [23]. In order to have reliable H-mode operation a safety margin has to be considered for P_{sep}. Here a safety margin of 20 % for stable type I ELMy H-mode operation is assumed.

$$P_{sep} = 1.2 P_{LH} \qquad \text{[MW]} \tag{4.4}$$

Hence the power crossing the separatrix amounts to about 100 MW, assuming that 50 MW of power is radiated within the confined plasma, the net power in the core plasma needs to be 150 MW. Adding the radiated power to the neutron load on the first wall results in a heat flux density of about 0.7 MWm^{-2}. A reduction of the LH threshold was recently reported in ASDEX Upgrade with tungsten plasma facing

components [24] and JET with the ITER-like wall [25]. A reduced LH threshold power would allow for a higher radiated power in the confined plasma, further mitigating the heat flux into the divertor.

4.3.1. Heat Flux Model

For the steady state heat flux in L-mode and in H-mode in between ELMs without external magnetic perturbation, a model is used to describe the heat flux profile onto the outer divertor target plates [26]. The model assumes an exponentially decaying power profile at the divertor entrance (eq. 4.5) and diffusive heat transport perpendicular to the flux surfaces in the divertor region.

$$q_{\exp}(s) = q_0 \exp\left(-\frac{s - s_0}{\lambda_q f_x}\right) \qquad \text{for } s > s_0 \left[\frac{\text{MW}}{\text{m}^2}\right] \tag{4.5}$$

Where q_0 is the upstream peak heat flux, s the position on the target, s_0 the position of the separatrix on the target, λ_q is the upstream power fall-off length and f_x is the poloidal flux expansion. To get the target heat flux profile, this function is convolved with a Gaussian which models the diffusive process.

$$q(s) = \frac{q_0}{2} \exp\left(\left(\frac{S}{2\lambda_q}\right)^2 - \frac{s - s_0}{\lambda_q f_x}\right) \operatorname{erfc}\left(\frac{S}{2\lambda_q} - \frac{s - s_0}{S f_x}\right) \qquad \left[\frac{\text{MW}}{\text{m}^2}\right] \tag{4.6}$$

Here S is the width of the Gaussian. This function is fitted to the measured heat fluxes to get the power fall-off length λ_q and the divertor broadening S. An illustration of the heat flux profile with different values for the divertor broadening S is shown in fig. 4.2. Note here that this model does not include dissipative processes reducing the total power load on the divertor. Although no dissipation is included the peak heat flux density is decreasing with increasing divertor broadening S.

The divertor broadening S is interpreted as a competition between the heat transport parallel and perpendicular to the magnetic field lines.

$$S \sim L\sqrt{\frac{\chi_\perp}{\chi_{||}}} \qquad \text{[mm]} \tag{4.7}$$

Where L is the connection length between the X-point and the divertor target, $\chi_\perp$ the heat diffusivity perpendicular and $\chi_{||}$ parallel to the magnetic field lines.

For the power load distribution on the target, a universal quantity is defined as the integral power fall-off length λ_{int}, which is independent of the shape of the measured

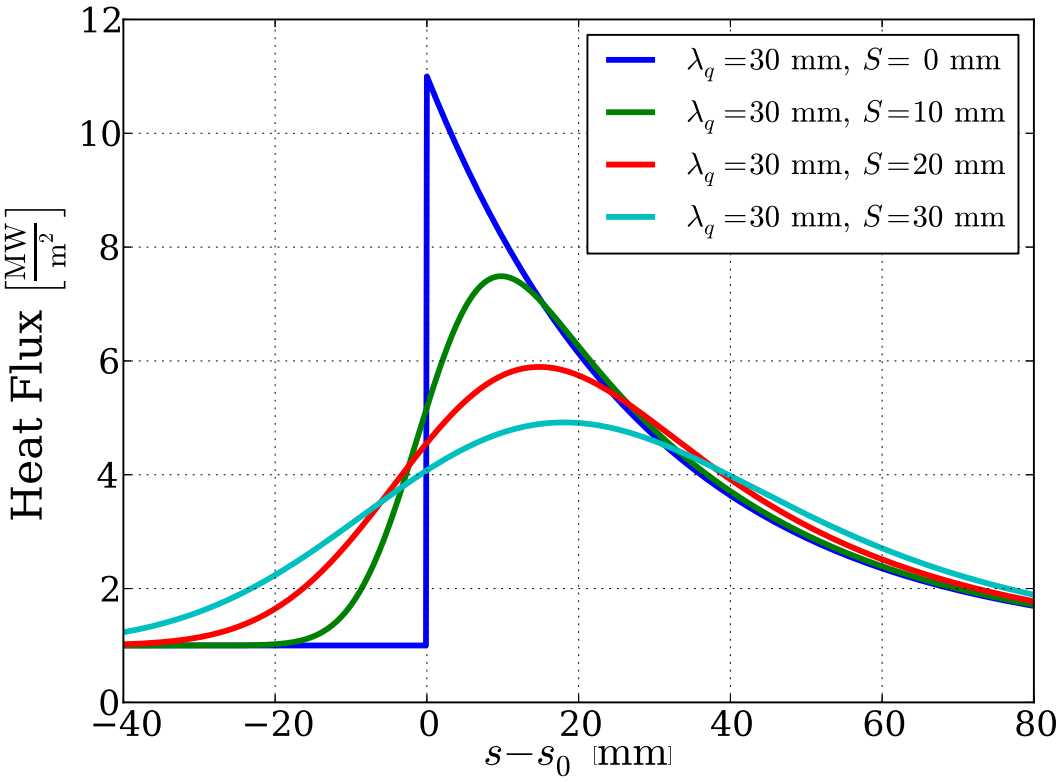

Figure 4.2: Illustration of the heat flux profile evolution from the divertor entrance towards the target plates.

heat flux profile $q(s)$.

$$\lambda_{int} = \frac{\int q(s)\mathrm{d}s}{q_{max}} \qquad [\mathrm{mm}] \tag{4.8}$$

Where q_{max} is the maximum of the heat flux profile $q(s)$ on target.

Using the heat flux model (eq. 4.6) one can approximate λ_{int} using the power fall-off length λ_q and the divertor broadening S [27].

$$\lambda_{int} \approx \lambda_q + 1.64\, S \qquad [\mathrm{mm}] \tag{4.9}$$

For the divertor design in large fusion devices λ_{int} is an important quantity. With it the peak heat flux density q_{max} is estimated for a given total power flux into the divertor P.

$$q_{max} = \frac{P}{2\pi R_{div}\left(s_{q=q_{max}}\right)\lambda_{int} f_x} \qquad \left[\frac{\mathrm{MW}}{\mathrm{m}^2}\right] \tag{4.10}$$

Where R_{div} is the major radius of the divertor target. To be able to predict λ_{int}, both the power fall-off length λ_q and the divertor broadening S need to be known.

4.3.2. Flux Expansion

The width of the heat flux profile on target is given by three independent mechanisms. The first mechanism is the heat transport in the SOL, this is the mechanism mainly forming the shape of the profile. The second mechanism is the *magnetic flux expansion* $f_{x,mag}$ [28].

$$f_{x,mag} = \frac{R_{mp}\, B_{pol}^{mp}}{R_{div}\, B_{pol}^{div}} \tag{4.11}$$

Where R is the major radius and B_{pol} the poloidal magnetic field at the outer mid plane (mp) and the divertor target (div) respectively. The magnetic flux expansion widens the heat flux profile perpendicular to the magnetic field lines. A schematic representation is shown in figure 4.3a). Looking at the magnetic equilibrium (fig. 4.3a)), it gets clear that the poloidal magnetic field decreases from the outer mid plane towards the X-point. Therefore the distance between a magnetic field line and the separatrix is larger near the X-point (green) compared to the outer mid plane (magenta, red). Between the X-point and the divertor target the poloidal magnetic field increases again due to the proximity of the (toroidal) divertor coil. This in turn again decreases the distance between the magnetic field line and the separatrix (blue). Since the divertor target is closer to the X-point than the outer mid plane, the distance between magnetic field line and separatrix is effectively increased on the target compared to the outer mid plane (magenta $\rightarrow$ blue).

In addition to the magnetic flux expansion the target geometry of the divertor itself influences the width of the measured heat flux profile (fig. 4.3b)). The target plate can have a poloidal inclination α_{pol} with respect to the magnetic field line, further increasing the distance between field lines. The geometric flux expansion $f_{x,geo}$ is calculated as:

$$f_{x,geo} = \frac{1}{\sin \alpha_{pol}} \tag{4.12}$$

Where α_{pol} is the angle between the target surface and the poloidal projection of the magnetic field line. Figure 4.3b) shows an illustration of the geometric flux expansion for different target inclinations. In the case where the poloidal projection of the field line is perpendicular to the target (black), the geometric flux expansion $f_{x,geo}$ is one. With decreasing target inclination angle (blue and green) the distance of two adjoined field lines (solid and dashed) increases on the target.

The total flux expansion f_x on the divertor target is the product of the magnetic and

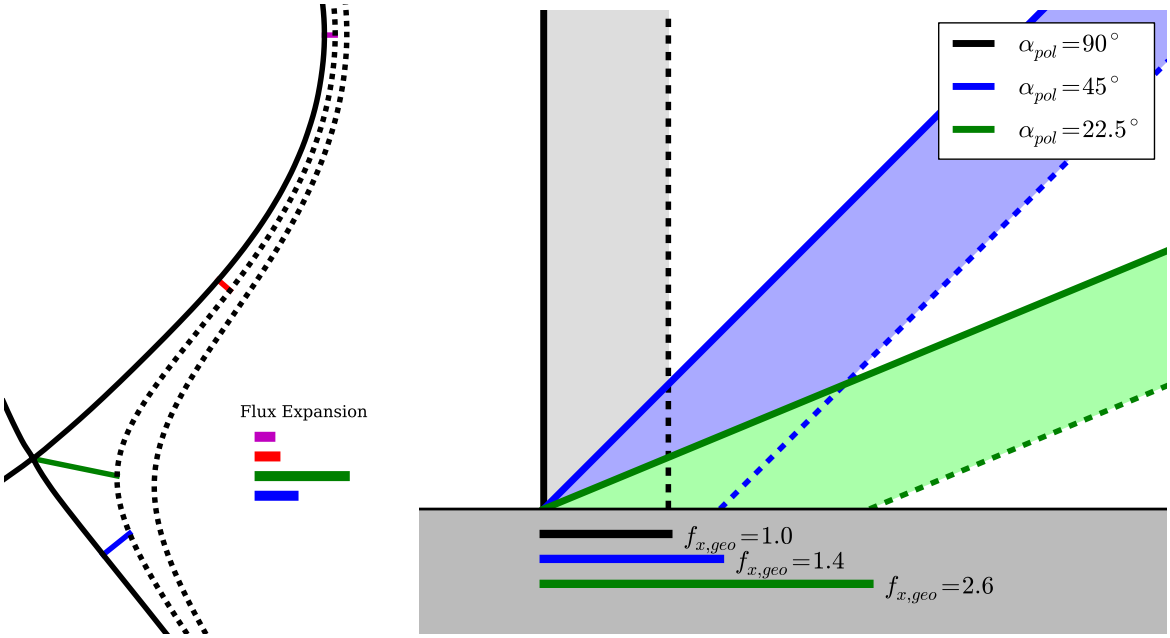

a) Magnetic flux expansion of the flux surfaces in the SOL.

b) Geometric flux expansion for different target inclination angles.

Figure 4.3: Illustration of the magnetic and geometrix flux expansion.

.

the geometric flux expansion.

$$f_x = f_{x,mag} \cdot f_{x,geo} = \frac{R_{mp} B_{pol}^{mp}}{R_{div} B_{pol}^{div}} \cdot \frac{1}{\sin \alpha_{pol}} \tag{4.13}$$

For typical discharges in ASDEX Upgrade and JET the flux expansion is of the order of 4–6. In order to make statements about the heat transport in the SOL and to be able to compare data between different devices and divertor geometries, the measured target heat flux widths have to be divided by the flux expansion f_x.

For any device it is beneficial to increase the flux expansion in order to spread the power load onto a wider area. The magnetic flux expansion is mainly given by the ratio between the poloidal magnetic field at the outer mid plane and the divertor target. This gain in magnetic flux expansion is limited. Decreasing the inclination α_{pol} between the magnetic field lines and the divertor target can increase the geometric flux expansion. However the smaller the inclination becomes the longer the divertor target needs to be, calling for a larger poloidal cross section of the device. The size of the machine in turn is limited by the size of the toroidal field coils.

Taking those limitations into account the flux expansion in future devices like ITER and DEMO cannot be larger than those achieved in present devices and will lie around 5.5–6.

Assuming a power distribution of one third to the inner divertor and two thirds to the outer divertor, the outer divertor has to be able to handle a heat flux of about 67 MW. This reasoning is assuming no radiative power losses in the scrape-off layer. In order to reduce the heat flux density on the target to 10 $\mathrm{MWm^{-2}}$ the power has to be distributed onto an area of 6.7 $\mathrm{m^2}$.

The divertor of ITER will have a major radius of 5.5 m. In order to prevent leading edges, which would receive a higher thermal load, the castellated tiles of the divertor are toroidally inclined in order to hide the neighbouring edge from the plasma. This so called *shadowing* reduces the effective area in the divertor which is exposed to the plasma. Due to manufacturing tolerances only 75 % of toroidal circumference will be exposed to the heat flux [29]. This fraction is the so called *toroidal wetted fraction* f_{tor}, which has to be taken into account for the calculation of the peak heat flux.

Using this the resulting power deposition width λ_{int} would be about 26 cm in order to achieve 10 $\mathrm{MWm^{-2}}$ on the target.

This deposition width is incompatible with recent studies suggesting a power fall-off length λ_q of around 1 mm for ITER in the outer mid plane [3, 30]. Taking into account the geometry of the magnetic field lines in the divertor and assuming no further broadening this would result in a target profile width of around 5.5 mm. Without radiative cooling in the scrape-off layer this would induce a heat flux density of nearly 470 $\mathrm{MWm^{-2}}$ on the target. From this it becomes clear that power needs to be radiated in the scrape-off layer and in the divertor in order to reduce the heat load onto the divertor target.

A point that will not be discussed in this work is the power load induced on the first wall by scrape-off layer radiation. Due to localised radiation close to the wall a high heat load can be induced. Weather or not this poses a possible threat for large devices needs to be assessed in further studies.

Assuming a power into the divertor of 8 MW which corresponds to a radiation of about 90 % in the scrape-off layer the target heat flux density would result in 56 $\mathrm{MWm^{-2}}$. From this it is clear that even with a high radiative power in the SOL a further profile broadening is needed to reduce the heat flux density on the target.

4.4. Two Point Model

For the description of the temperature and density distribution along field lines in the SOL, a successful approach is the so called two point model. In the two point model,

the SOL is assumed to be stretched between the upstream stagnation point, where there is no net particle flux, and the divertor target plates. For the parallel heat flux $q_{||}$ in the SOL classical heat conduction is assumed:

$$q_{||} = -\kappa \frac{\mathrm{d}T}{\mathrm{d}x} \qquad \left[\frac{\mathrm{MW}}{\mathrm{m}^2}\right] \tag{4.14}$$

Where κ is the heat conductivity. Assuming Spitzer-Härm conductivity [31] this equation is written as:

$$q_{||} = -\kappa_0 T^{\frac{5}{2}} \frac{\mathrm{d}T}{\mathrm{d}x} \qquad \left[\frac{\mathrm{MW}}{\mathrm{m}^2}\right] \tag{4.15}$$

Where κ_0 has a numerical value of about 2000 $\mathrm{Wm}^{-1}(\mathrm{eV})^{-3\,5}$. Under the assumption, that all the heat enters the SOL plasma at the upstream position ($x = 0$) the equation can be integrated along the SOL. With the knowledge of the target temperature T_d the upstream temperature T_u is calculated as,

$$T_u = \left(T_d^{\frac{7}{2}} + \frac{2q_{||}L}{7\kappa_0}\right)^{\frac{2}{7}} \qquad [\mathrm{eV}] \tag{4.16}$$

For low target temperatures T_d the following approximation is often used.

$$T_u \approx T_d + \left(\frac{2q_{||}L}{7\kappa_0}\right)^{\frac{2}{7}} \qquad [\mathrm{eV}] \tag{4.17}$$

For $T_d = 0$ the approximation is correct. So far this is the *classic* calculation of the two point model, where the heat flux density $q_{||}$ is assumed to be constant along field lines. For the divertor geometry this is not a valid approximation. In the divertor region between the X-point and the divertor target, the heat flux density is decreased by a diffusive process perpendicular to the magnetic field lines. This has an influence on the temperature profile along the magnetic field line. Starting from equation 4.15 the temperature distribution along the field line is calculated for arbitrary heat flux density distributions.

$$T(l) = \left(T_d^{\frac{7}{2}} + \frac{7}{2\kappa_0}\int_0^L q_{||}(l')\mathrm{d}l'\right)^{\frac{2}{7}} \qquad [\mathrm{eV}] \tag{4.18}$$

To show the influence of the reduced heat flux density in the divertor region a model calculation using ITER parameters is performed. It is assumed that 8 MW enter the SOL upstream, this is equivalent to a radiative cooling of about 90 % of the total power and two thirds of the power flowing towards the outer target. The effect of radiative cooling along the field lines is neglected. For the divertor broadening between the

X-point and the divertor target a linear increase is assumed. The λ_{int} profiles along the field lines used for the calculation are shown in figure 4.4. With this the peak heat

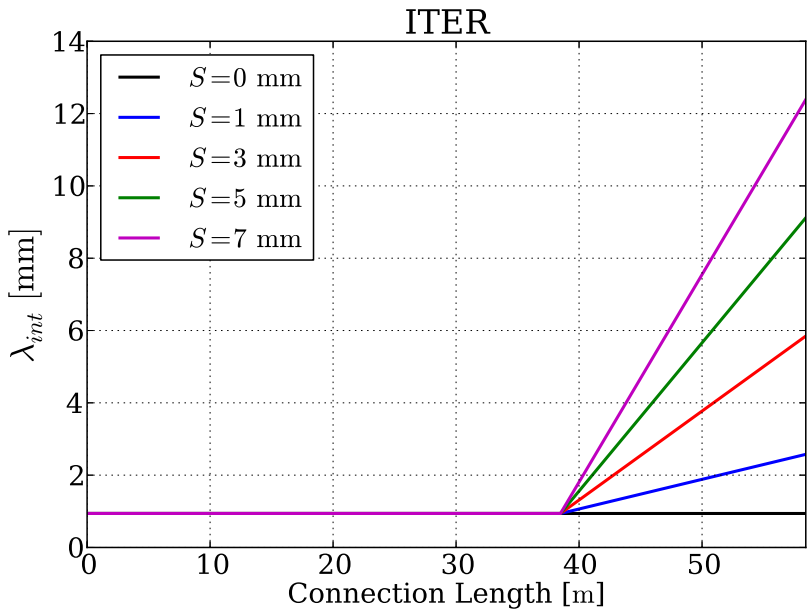

Figure 4.4: Assumed λ_{int} for different magnitudes of divertor broadening S in an ITER test case.

flux density (along the *hottest* field line) is calculated:

$$q = \frac{P}{2\pi R \lambda_{int}} \qquad \left[\frac{\mathrm{MW}}{\mathrm{m}^2}\right] \tag{4.19}$$

Figure 4.5 shows the resulting heat flux density. The absolute value shown resembles the target heat flux including the flux expansion, the parallel heat flux needed to calculate the temperature profile along the field line is considerably higher. It is seen that the profile broadening in the divertor volume strongly decreases the heat flux density. A profile width of about 6 mm (about 3.3 cm on the target) is sufficient to reduce the target heat flux density to about 10 MWm^{-2}. The green highlighted area indicates the material limit for steady state operation in ITER. A more detailed study of the heat transport in the SOL and the heat flux profile broadening in the divertor is presented in chapter 5.

Using these heat flux density distributions the temperature along the field line is calculated using equation 4.18. For the target temperature 10 eV is assumed. The resulting temperature distributions are shown in figure 4.6. For the case without broadening the upstream temperature reaches about 200 eV. The wider the broadening is the smaller is the temperature gradient in the divertor region becomes. Due to the high heat flux in the SOL outside the divertor the temperature gradient increases again and the upstream temperature is mostly recovered. For the temperature distribution in the divertor region it is seen that although the heat flux density is reduced it still reaches

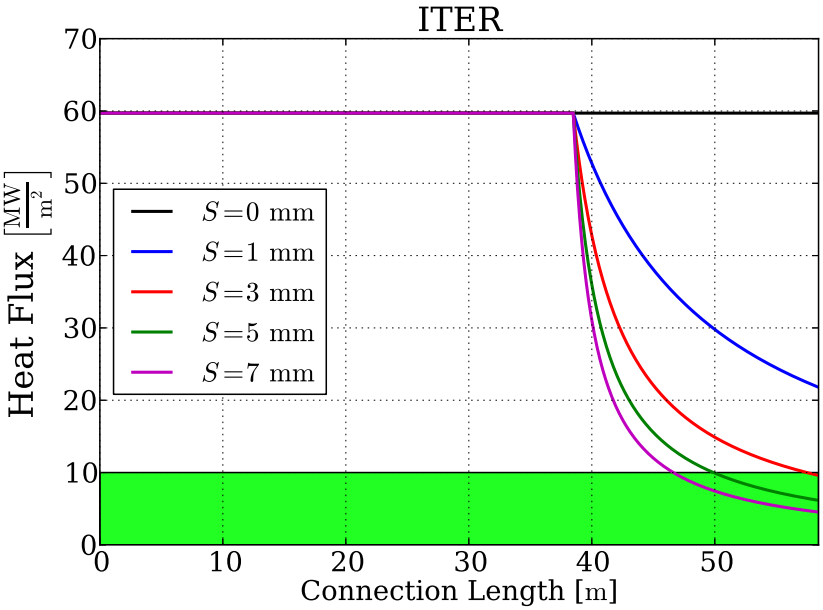

Figure 4.5: Heat flux density along the hottest field line in ITER assuming 8 MW of power entering the divertor. The heat flux shown resembles the target heat flux.

relatively high values of about 50 eV close to the divertor target. Due to these high temperatures it is questionable whether such a case is realistic. The area in which the plasma can efficiently lose momentum and pressure ($T < 15$ eV) would be close to the divertor target and the gain for the target heat flux due to radiation would be small. The black temperature distribution in figure 4.6 equals the result from equation 4.16. In the divertor region this result deviates significantly from the more realistic case with profile broadening.

Therefore it is concluded that the heat flux distribution along the field line needs to be taken into account in order to calculate the temperature distribution.

Using equation 4.15 the temperature gradient along the field line is calculated as:

$$\frac{\mathrm{d}T}{\mathrm{d}x} = -\frac{q_{||}}{\kappa_0 T^{\frac{5}{2}}} \qquad \left[\frac{\mathrm{eV}}{\mathrm{m}}\right] \tag{4.20}$$

From this it results that for low temperatures a comparably small heat flux density is sufficient to sustain a large temperature gradient. This is the reason for the steep temperature increase near the target in figure 4.6. In order to sustain low temperature conditions in a large volume of the divertor the power arriving in the divertor has to be reduced as far away from the target as possible. To achieve this under real operational conditions, radiators have to be found that can efficiently radiate power at temperatures between about 10 and 100 eV.

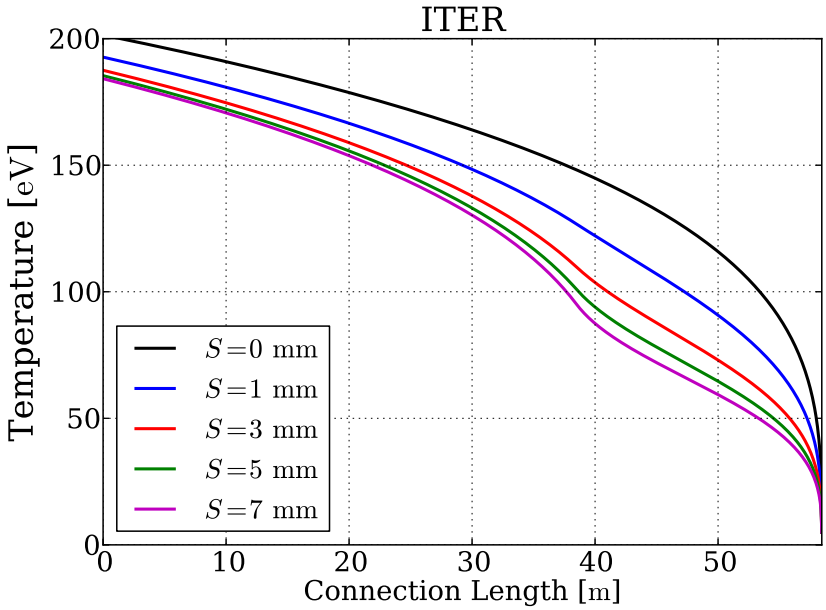

Figure 4.6: Temperature distribution along the hottest field line assuming a target temperature of 10 eV.

These considerations assumed steady state power loads and are not applicable to large transient heat loads as they are present during ELMs. For those the high heat flux will lead to a strong increase of the divertor temperature. Even for detached divertor conditions it is unlikely that the divertor will be able to radiate a large fraction of the ELMs energy. Therefore the ELM will deposit energy onto the divertor target. A more detailed analysis of the ELM heat load deposition is shown in chapter 6.

Chapter 5

Steady State Divertor Power Load

In this chapter the steady state heat load on the divertor target is reviewed. The data shown here was obtained at ASDEX Upgrade and JET in L-mode and in H-mode discharges. The power fall-off length λ_q in JET-ILW H-mode discharges is compared to a widely agreed scaling obtained in carbon devices. Using ASDEX Upgrade L-mode discharges the influence of the divertor conditions on the divertor broadening S is studied. An empirical scaling for S based on the divertor temperature is derived. In addition the measured S is compared to theoretical and empirical transport models. An extrapolation of the divertor heat flux towards ITER and DEMO is presented based on the empirical scalings of both λ_q and S.

5.1. Power Fall-Off Length

In the following section, the power fall-off length λ_q is discussed. The L-mode results shown in this section were partly obtained in the work of A.Scarabosio [32].

In figure 5.1 the heat flux profile on the outer divertor target in JET-ILW is shown before and after the LH-transition. It is seen that the L-mode profile (black) has a larger radial extend compared to H-mode (red). The heat flux model (Equation 4.6) was fitted to both profiles (solid lines), being able to match the profile shape of the measured heat flux in L- and H-mode.

5.1.1. L-mode

For the power fall-off length λ_q in L-mode an empirical scaling based on data from ASDEX Upgrade and JET with carbon plasma facing components was found, using

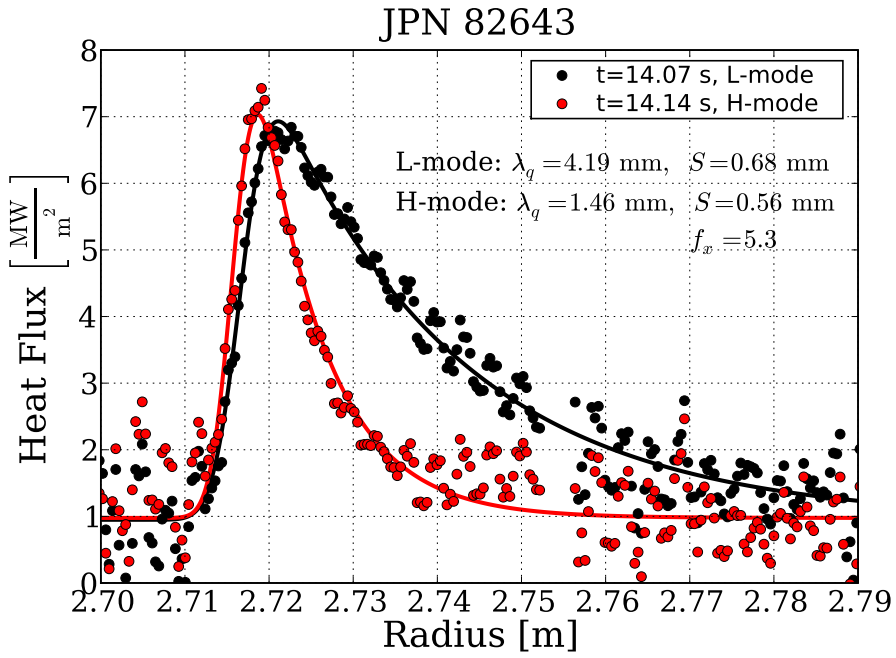

Figure 5.1: Heat load profiles on the outer divertor target in JET-ILW before and after the LH-transition. The solid lines show the fit of the heat flux model to the data.

the model described in section 4.3.1 [32].[1]

$$\lambda_{q,scal} = 1.44 \pm 0.67\, B_{tor}^{-0.80\pm0.32}\, q_{95}^{1.14\pm0.67}\, P_{SOL}^{0.22\pm0.10}\, R^{-0.03\pm0.28} \qquad [\mathrm{mm}] \qquad (5.1)$$

In the scaling λ_q decreases with increasing toroidal magnetic field B_{tor} and increases with increasing safety factor q_{95}. The safety factor q is defined as the number of toroidal turns a field line performs for one poloidal turn and can be expressed as follows.

$$q = \frac{r \cdot B_{tor}}{R \cdot B_{pol}} \qquad (5.2)$$

Where r and R are the minor and major radii of the flux surface containing the magnetic field line. q_{95} is the safety factor of the field line on the magnetic flux surface containing 95 % of the poloidal magnetic flux in the confined region. Most notably the upstream power fall-off length λ_q shows no dependence on the major radius R. Furthermore the L-mode scaling for the power fall-off length λ_q shows no dependence on the power crossing the separatrix into the SOL P_{SOL}.

This result is interesting to keep in mind, since it has similar parametric dependencies as the power fall-off length in H-mode (eq. 5.3). The main difference to the H-mode scaling is the prefactor of the scaling whose value is about twice as large for L-mode.

[1] For the scaling B_{tor} in T, P_{SOL} in MW and R in m was used.

5.1.2. H-mode

In H-mode the steady state heat flux is interrupted by periodically occurring transient heat loads, which are induced by ELMs. The evaluation of the power fall-off length is conducted in-between the ELMs where the power load is stationary. A separate discussion of the ELM induced divertor power load is given in chapter 6.

Using data from ASDEX Upgrade and JET with carbon plasma facing components an empirical scaling has been found [3] for H-mode discharges.

$$\lambda_{q,scal} = 0.73 \pm 0.38\, B_{tor}^{-0.78\pm0.25}\, q_{cyl}^{1.20\pm0.27}\, P_{SOL}^{0.10\pm0.11}\, R^{0.02\pm0.20} \qquad \text{[mm]} \qquad (5.3)$$

q_{cyl} is the cylindrical safety factor, which is similar to the generic safety factor (5.2) but takes the poloidal shape of the plasma into account:

$$q_{cyl} = \frac{2\pi a \epsilon B_{tor}}{\mu_0 I_p} \cdot \frac{(1+\kappa^2)}{2} \qquad (5.4)$$

Where a is the minor radius, ϵ the aspect ratio R/a, I_p the plasma current and κ the elongation of the plasma. Similar to the L-mode case, in the scaling the power fall-off length λ_q decreases with increasing toroidal magnetic field B_{tor} and increases with the cylindrical safety factor q_{cyl}. The power crossing the separatrix into the SOL widens the power fall-off length, however, the exponent is not very large with a value of about 0.1. Notably the scaling does not exhibit a dependence on the major radius R. This is important because it implies that no beneficial widening of the upstream power fall-off length occurs when increasing the machine size.

The scaling (eq. 5.3) has been obtained in devices with carbon plasma facing components. Since carbon is deemed inapplicable for the use in fusion reactors, the use of metals for plasma facing components has been studied, especially in all tungsten ASDEX Upgrade and JET with the ITER-like wall. In this context it is important to study the power fall-off length in an all metal environment. The following results were obtained in JET-ILW on the bulk tungsten outer divertor target (fig. 3.3).

Figure 5.2 shows the measured power fall-off length λ_q in JET-ILW compared to the empirical scaling (eq. 5.3) in H-mode discharges with toroidal magnetic fields between 1.0 and 3.1 T and plasma currents ranging from 1.0 to 3.5 MA. It is found, that the power fall-off length in JET-ILW for attached divertor conditions, can be described by the empirical scaling (eq. 5.3) found in carbon ASDEX Upgrade and JET. The measured values for λ_q span a range between 0.7 and 3.3 mm. For ITER the predicted value for λ_q is about 1 mm. This is notable since the predicted value for ITER lies within the range of the values measured in JET-ILW.

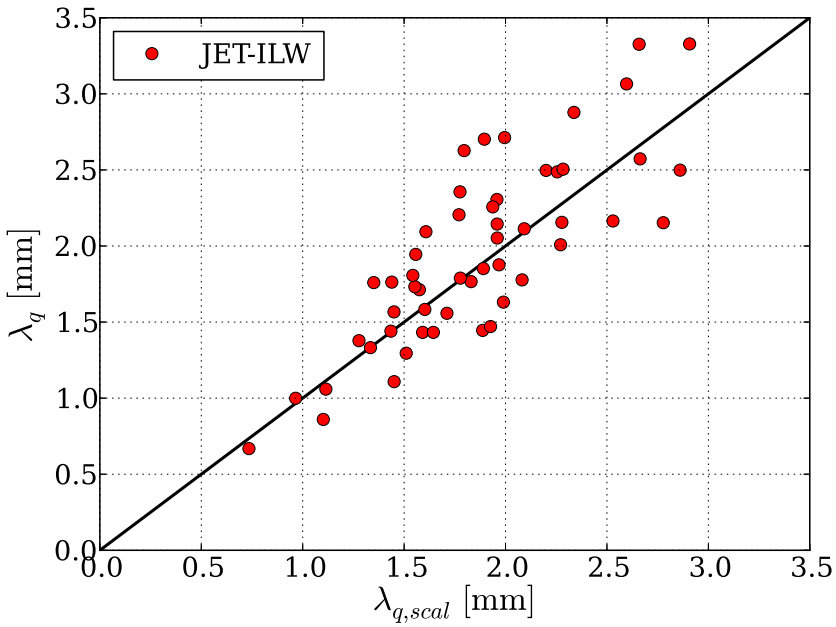

Figure 5.2: Comparison of the measured power fall-off length λ_q [33] in JET-ILW with the empirical scaling obtained in JET and ASDEX Upgrade with carbon plasma facing components (eq. 5.3).

The results from a nonlinear regression analysis using JET-ILW data alone gives a similar scaling as found in JET and ASDEX Upgrade with carbon plasma facing components (eq. 5.3).

$$\lambda_q = 0.42 \pm 0.22\, B_{tor}^{-1.17\pm0.24}\, q_{cyl}^{1.29\pm0.28}\, P_{SOL}^{0.48\pm0.14} \qquad \text{[mm]} \qquad (5.5)$$

Since JET-ILW data alone was used for this regression, the major radius R is not included in the evaluation and no statement can be made on its influence on the power fall-off length λ_q. In the scaling the power fall-off length decreases with increasing toroidal magnetic field B_{tor} and increases with the cylindrical safety factor q_{cyl}. For the power entering the SOL (P_{SOL}) a positive value for the exponent has been found which is close to a square root dependence.

Within the uncertainties the scaling obtained in JET-ILW confirms the scaling found in the carbon devices (eq. 5.3). The only difference is the slightly higher exponent of the power in JET-ILW compared to the data set from machines with carbon plasma facing components.

Note here that the difference in the exponent of P_{SOL} in the scaling for the power fall-off length λ_q has a significant effect on the divertor power load due to the large

change in P_{SOL} when comparing JET and ITER.

$$P_{SOL}^{JET} \approx 10 \text{ MW} \tag{5.6}$$

$$P_{SOL}^{ITER} \approx 100 \text{ MW} \tag{5.7}$$

P_{SOL} in ITER is about 10 times higher than in JET. Using both the scaling obtained in carbon ASDEX Upgrade and JET (eq. 5.3) and in JET with the ITER-like wall (eq. 5.5) the following power fall-off lengths are predicted for ITER:

$$\lambda_{q,ITER}^{C} = 0.9 \text{ mm} \tag{5.8}$$

$$\lambda_{q,ITER}^{ILW} = 1.5 \text{ mm} \tag{5.9}$$

The power fall-off length predicted by the scaling obtained in JET-ILW is about 70 % larger compared to the prediction made with the scaling from ASDEX Upgrade and JET with carbon plasma facing components. No conclusion is drawn whether the higher dependence on P_{SOL} is a direct result from the metal wall in JET-ILW or a result of the higher gas fueling rate JET-ILW needs to be operated with compared to JET-C in order to prevent impurity accumulation.

5.2. Divertor Broadening S

The divertor broadening S is the width of the Gaussian resulting from the heat diffusion process in the divertor. A point source at the X-point would result in a Gaussian shaped profile on the divertor target with a width of $S \cdot f_x$, where f_x is the flux expansion of the divertor with respect to the outer mid plane (eq. 4.13).

5.2.1. Results from ASDEX Upgrade L-mode discharges

For the study of the divertor broadening, dedicated discharges with low to medium recycling divertor conditions [34] have been conducted in L-mode at ASDEX Upgrade with tungsten plasma facing components. L-mode discharges were chosen for this study to obtain stable divertor conditions which are not influenced by transient events such as ELMs. Values for the divertor broadening S reaching from 0.3 to 1.1 mm have been observed. An overview of the global parameters covered in the data set is shown in table 5.1.

	Min	Max	Unit
$\mathbf{I_p}$	0.6	1.0	MA
$\mathbf{B_{tor}}$	1.4	2.5	T
$\mathbf{B_{pol}}$	0.2	0.3	T
$\mathbf{B_{tot}}$	1.4	2.7	T
$\mathbf{q_{95}}$	3.1	6.8	
$\mathbf{P_{tot}}$	0.6	1.7	MW
$\mathbf{n_{e,ped}}$	8.5	21.9	$10^{18}\,\mathrm{m}^{-3}$
$\mathbf{n_{0,div}}$	4.2	11.8	$10^{21}\,\mathrm{m}^{-3}$
$\mathbf{T_{e,tar}}$	10	45	eV
$\mathbf{n_{e,tar}}$	1.5	4.7	$10^{18}\,\mathrm{m}^{-3}$

Table 5.1.: Overview of the parameter range for the ASDEX Upgrade L-mode discharges. The indices *ped*, *div* and *tar* indicate the measurement regions pedestal, divertor volume and target respectively.

Dependence on Machine Parameters

As a first step the dependence of the divertor broadening S on global discharge parameters is investigated. Therefore nonlinear regressions using various plasma parameters are conducted.

$$S = C_{S_0}\, n_{e,ped}^{C_{n_{e,ped}}} \left[10^{19}\mathrm{m}^{-3}\right] \cdot B_{pol}^{C_{B_{pol}}} [\mathrm{T}] \cdot n_{0,div}^{C_{n_{0,div}}} \left[10^{22}\mathrm{m}^{-3}\right] \qquad [\mathrm{mm}] \qquad (5.10)$$

To show the influence of the different quantities on S different parameter combinations were analysed. The result of the regression analysis is shown in (tab. 5.2).

	$\mathbf{C_{S_0}}$	$\mathbf{C_{n_{e,ped}}}$	$\mathbf{C_{B_{pol}}}$	$\mathbf{C_{n_{0,div}}}$	$\mathbf{R^2}$
Set 1	0.086 (07)	1.015 (97)	−1.025 (80)	−0.067 (71)	0.89
Set 2	0.090 (07)	1.018 (07)	−1.012 (32)		0.93
Set 3	0.062 (05)		−1.632 (50)	0.556 (05)	0.83
Set 4	0.217 (09)	1.947 (09)		−0.559 (75)	0.76

Table 5.2.: Regression results of the divertor broadening S in low recycling L-modes in all tungsten ASDEX Upgrade. The numbers in parenthesis give the uncertainty of the least significant figures.

One important quantity for the characterisation of the upstream conditions is the electron density at the separatrix $n_{e,sep}$. Due to the steep gradients at the separatrix and the limited resolution of the diagnostics the determination of $n_{e,sep}$ is difficult. The pedestal electron density $n_{e,ped}$ is used instead of $n_{e,sep}$ since it is more accessible for the diagnostics.

The regression results, using different combinations of the parameters, all indicate a strong dependence of the divertor broadening on the pedestal electron density $n_{e,ped}$

and the averaged poloidal magnetic field B_{pol}, which is defined as follows.

$$B_{pol} = \frac{\mu_0 I_p}{2\pi a \sqrt{\frac{1+\kappa^2}{2}}} \qquad [\mathrm{T}] \tag{5.11}$$

The divertor broadening S is increasing with the pedestal electron density $n_{e,ped}$ and decreasing with the poloidal magnetic field B_{pol} in all cases. The absolute value of the exponent of the poloidal magnetic field B_{pol} and the pedestal electron density $n_{e,ped}$ alone increase in combination with the neutral pressure $n_{0,div}$ in the divertor (Set 3,4). At the same time the exponent of the neutral density is positive in the case of the poloidal magnetic field B_{pol} (Set 3) and negative in the case with the pedestal electron density $n_{e,ped}$ (Set 4).

For the case where all three quantities $n_{e,ped}$, $n_{0,div}$ and B_{pol} are included in the evaluation, the neutral density in the divertor $n_{0,div}$ shows no influence on the divertor broadening having an exponent close to zero. The divertor broadening S increases about linear with the pedestal density $n_{e,ped}$ and decreases about linear with the poloidal magnetic field B_{pol}.

The coefficient of determination R^2 gives a quantity to qualify the ability of a given model Y to describe the available data y_i.

$$R^2 = 1.0 - \frac{\sum (Y_i - y_i)^2}{\sum (y_i - \bar{y})^2} \tag{5.12}$$

Where y_i is the measured data, Y_i is the estimated data of the model and $\bar{y}$ is the mean average of the measured data.

Set 2 in table 5.2 has been found to describe the measured divertor broadening S best, giving a coefficient of determination of $R^2 = 0.93$. The regression results of *set 2* are shown in figure 5.3. Note that no isotope dependence has been observed in this data set. Given that only three discharges in hydrogen were conducted for this study, no conclusions are drawn from this data set regarding the isotope dependence of the divertor broadening S.

Perpendicular Heat Diffusion

Using the measured divertor broadening S the perpendicular heat diffusivity $\chi_\perp$ in the SOL is deduced. Assuming the heat transport along the field lines is governed by a diffusive process the divertor broadening is interpreted as follows:

$$S = L\sqrt{\frac{\chi_\perp}{\chi_{||}}} \qquad [\mathrm{mm}] \tag{5.13}$$

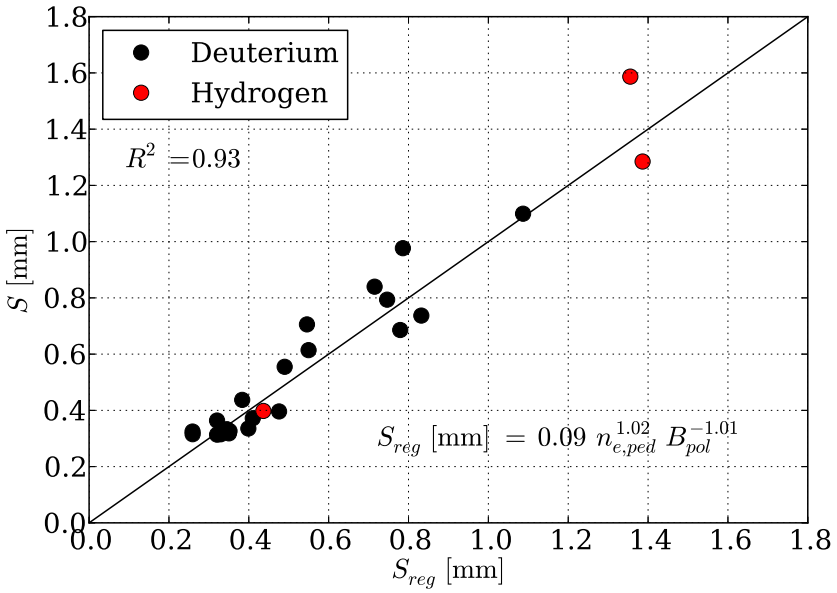

Figure 5.3: Regression result for the divertor broadening S in low density L-modes in ASDEX Upgrade [33].

Where L is the connection length in the SOL and $\chi_{||}$ the parallel heat diffusivity in the SOL. This relation is easy to understand given the underlying transport geometry. The diffusion width S is expressed in terms of the perpendicular diffusivity $\chi_{\perp}$ and the parallel diffusion time $\tau_{||}$.

$$S = \sqrt{\tau_{||}\,\chi_{\perp}} \qquad [\text{mm}] \tag{5.14}$$

The parallel diffusion time $\tau_{||}$ is estimated using the parallel heat diffusivity $\chi_{||}$ and the connection length L.

$$\tau_{||} \approx \frac{L^2}{\chi_{||}} \qquad [\text{s}] \tag{5.15}$$

Inserting this relation into equation 5.14 for the divertor broadening S results in equation 5.13. For both the ions and the electrons the parallel heat diffusion coefficient is estimated:

$$\chi_{e,||} = \kappa_0 \frac{T_e^{5/2}}{n_e} \qquad \left[\frac{\text{m}^2}{\text{s}}\right] \tag{5.16}$$

$$\chi_{i,||} = c_s\, L = \frac{T_e^{1/2}}{m_p^{1/2}} L \qquad \left[\frac{\text{m}^2}{\text{s}}\right] \tag{5.17}$$

Where T_e is the electron temperature, n_e the electron density, m_p the proton mass, L the connection length, κ_0 is about 2000 $\text{Wm}^{-1}\,(\text{eV})^{-3.5}$ and c_s is the ion sound speed. For the ion heat diffusivity, a pure deuterium plasma has been assumed with $T_e = T_i$.

Under these assumptions the ratio of electron and ion heat diffusivity follows as:

$$\frac{\chi_{e,||}}{\chi_{i,||}} = \frac{\kappa_0 m_p^{1/2}}{L} \frac{T_e^2}{n_e} \tag{5.18}$$

The ratio of parallel electron and ion heat diffusivity for the deuterium discharges in ASDEX Upgrade L-mode are shown in figure 5.4. It is seen that for all cases the parallel electron heat diffusivity is larger then the ion heat diffusivity. The smallest ratio observed in this dataset corresponds to the largest divertor broadening S.

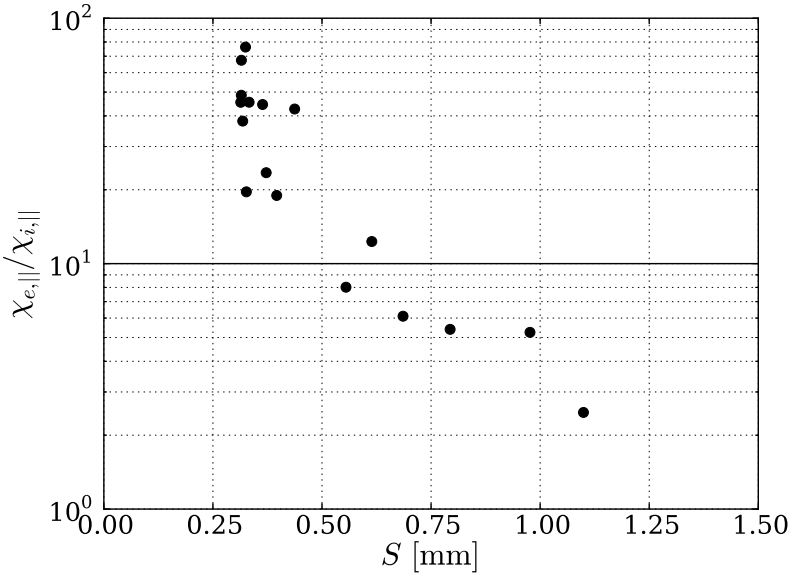

Figure 5.4: Ratio of parallel electron and ion heat diffusivity in dependence of the divertor broadening S for low recycling deuterium L-mode discharges in ASDEX Upgrade.

In the following the parallel heat diffusion in the SOL is assumed to be carried mainly by the electrons. Using parallel electron heat diffusivity for the parallel transport in equation 5.13, the perpendicular heat diffusivity $\chi_\perp$ is estimated as:

$$\chi_\perp = \chi_{e,||} \left(\frac{S}{L}\right)^2 \qquad \left[\frac{\mathrm{m}^2}{\mathrm{s}}\right] \tag{5.19}$$

Note that due to the changing flux expansion along a field line in the SOL, it is difficult to answer whether the measured target profile broadening or a mapped quantity should be used for the calculation of the perpendicular heat diffusivity. Since the assumption of the diffusive heat transport model is that the broadening of the heat flux profile only takes place in the region between the X-point and the target, the following method of mapping is used, as illustrated in figure 5.5.

The measured target electron temperature and density (blue dots) are mapped to half the poloidal distance between the X-point and the strike line position on the target (red

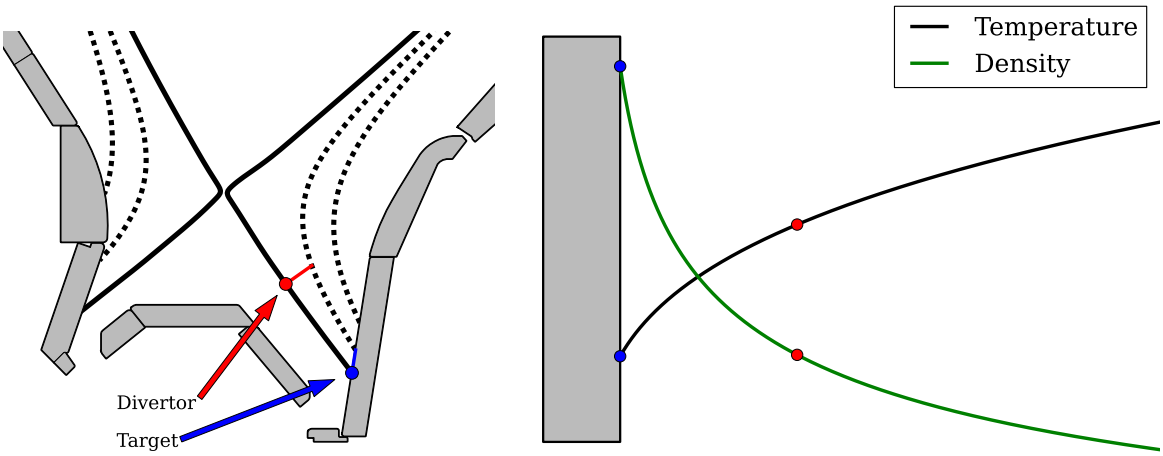

a) Geometric mapping of the target (blue) and divertor (red) positions.

b) Schematic temperature and density evolution along a magnetic field line from the target to the X-point.

Figure 5.5: Geometric mapping used for the evaluation of the divertor broadening.

dots) along the field lines using the measured parallel heat flux q_0 and the assumption that the two point model is valid (Section 4.4). For the connection length L, the distance between the X-point and the divertor target l_x is used for a field line starting close to the separatrix (distance d = 5 mm at the outer mid plane). This is done to identify any *artificial* temperature dependence of the perpendicular heat diffusivity which could result from different parallel temperature gradients close to the target. Figure 5.6 shows the electron temperature distribution along a field line in the divertor region for different discharges calculated from the two point model (eq. 4.16).

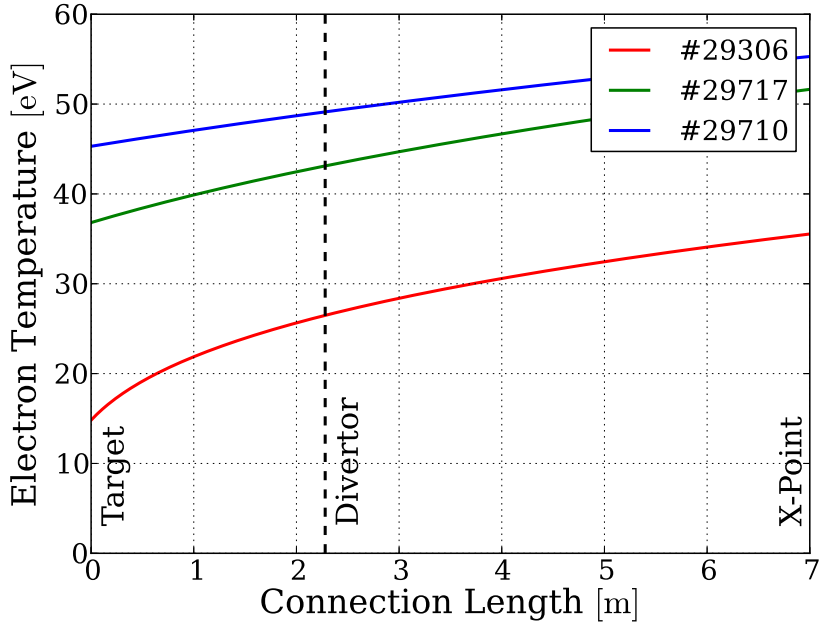

Figure 5.6: Electron temperature distribution along a field line between the target and the X-point for the discharges with the lowest (red), highest (blue) and median (green) electron temperature at the divertor target.

As a first step the influence of the divertor conditions, namely the electron temperature and density, on S is investigated. Therefor a nonlinear regression for the divertor broadening has been performed.

$$S = S_0 \, T_e^{C_T} \, n_e^{C_n} \qquad \text{[mm]} \tag{5.20}$$

Where T_e is the electron temperature in eV, n_e the electron density in 10^{19} m^{-3} and C_n, C_T are the corresponding exponents. It is found that the electron density in the divertor has no significant influence on S. This is illustrated in figure 5.7.

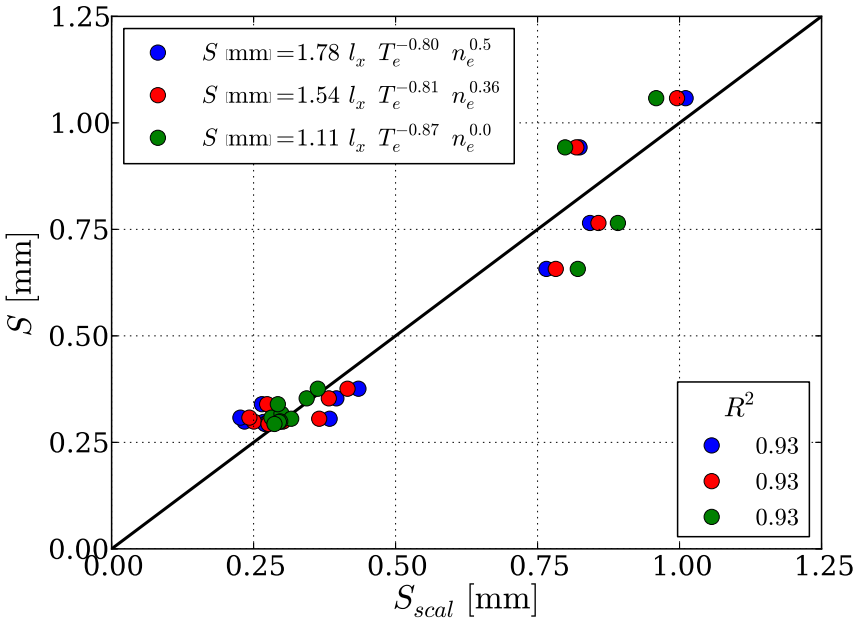

Figure 5.7: Results of the nonlinear regression of the divertor broadening S using the divertor temperature and density.

Here three cases are shown. The results shown in red are obtained by fitting both exponents C_n and C_T. In the other two cases the exponent of the density was set to 0.5 (blue) and 0 (green). The case with $C_n = 0.5$ corresponds to a perpendicular heat diffusivity $\chi_\perp$ which is independent of the density. Assuming no density dependence of S ($C_n = 0$) corresponds to a linear decrease of $\chi_\perp$ with the density.

All three cases have the same coefficient of determination R^2 and the dependence on the temperature does not change withing the error bars. From this it is concluded that for the available data the density has no influence on the divertor broadening.

Knowing this, an elegant way to study the influence of the divertor temperature on S is to assume a dependence of $\chi_\perp$ on the electron temperature and the electron density

similar to the parallel electron heat diffusivity $\chi_{e,||}$:

$$\chi_\perp = \chi_{\perp,0}\frac{T_e^{C_{T_e,\chi_\perp}}}{n_e} \qquad \left[\frac{\mathrm{m}^2}{\mathrm{s}}\right] \tag{5.21}$$

Where $C_{T_e,\chi_\perp}$ is the unknown exponent of the temperature dependence. Using this parametrisation the density dependence in the parallel and perpendicular heat diffusivity chancel each other in the calculation of S.

Generic heat conduction gives one possible explanation for the density dependence of $\chi_\perp$. For the heat conductivity κ and the heat diffusivity χ the following relation is given [35].

$$\chi = \frac{\kappa}{\rho c_p} \qquad \left[\frac{\mathrm{m}^2}{\mathrm{s}}\right] \tag{5.22}$$

Where ρ is the density and c_p is the specific heat capacity. For a plasma the heat capacity ρc_p is proportional to the electron density n_e resulting in:

$$\chi = \frac{\kappa}{n_e} \qquad \left[\frac{\mathrm{m}^2}{\mathrm{s}}\right] \tag{5.23}$$

If the heat conductivity κ is independent of the electron density then χ would decrease linearly with n_e. Having exploited this no conclusion is drawn about the density dependence of S.

Due to a strong correlation between the total magnetic field and the target electron temperature in this data set (fig. 5.8), no attempt is made to obtain the dependence of the perpendicular diffusivity on the magnetic field. A discussion of the dependence on the magnetic field is made in section 5.3, where SOL heat transport models are compared to the measured divertor broadening S.

Under the assumption expressed in equation 5.21 the model for the divertor broadening S is written as follows using equation 5.13.

$$S = l_x\sqrt{\frac{\chi_{\perp,0}\frac{T_e^{C_{T_e,\chi_\perp}}}{n_e}}{\kappa_0\frac{T_e^{\frac{5}{2}}}{n_e}}} \qquad [\mathrm{mm}] \tag{5.24}$$

$$= l_x\sqrt{\frac{\chi_{\perp,0}}{\kappa_0}}T_e^{\frac{C^{T_e,\chi_\perp}}{2}-\frac{5}{4}} \tag{5.25}$$

$$= l_x\sqrt{\frac{\chi_{\perp,0}}{\kappa_0}}T_e^{C_{T_e,S}} \tag{5.26}$$

The exponent $C_{T_e,S}$ for the temperature dependence of the divertor broadening S is

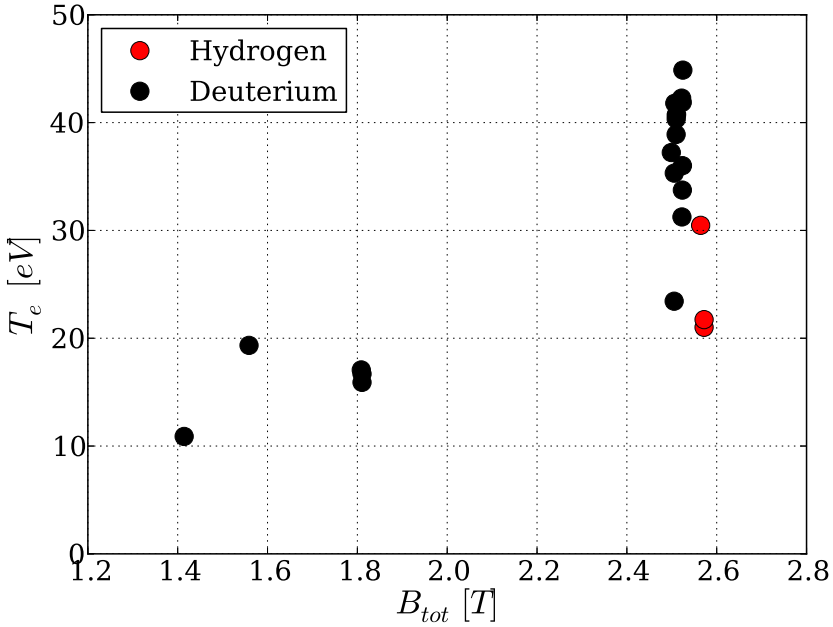

Figure 5.8: Target electron temperature T_e and total magnetic field B_{tot} in ASDEX Upgrade for the available data set.

the result of the difference between the exponent of the temperature dependence of the perpendicular and parallel heat diffusivities.

$$C_{T_e,S} = \frac{C_{T_e,\chi_\perp} - \frac{5}{2}}{2} \tag{5.27}$$

Using the described models for the perpendicular heat diffusivity (eq. 5.21) and the divertor broadening S (eq. 5.24) the sensitivity of the temperature dependence has been studied. The exponent of the temperature dependence $C_{T_e,\chi_\perp}$ has been varied between 0 and 5/2 corresponding to a change of $C_{T_e,S}$ between -1.25 and 0. For every value of $C_{T_e,\chi_\perp}$ the prefactor $\chi_{\perp,0}$ has been adapted to give the best fit to the data. The results of this study are shown in figure 5.9 for both target (black) and divertor (red) mapping.

For both the target and the divertor data set, the parametrisation of the perpendicular heat diffusivity $\chi_\perp$ (eq. 5.21) is able to describe the measurement to a good extend, having values for the coefficient of determination R^2 close to one. For the perpendicular heat diffusivity (fig. 5.9b)) the R^2 profiles are broad and it is difficult to draw conclusions about the value of $C_{T_e,\chi_\perp}$. For the divertor broadening S (fig. 5.9a)) the R^2 profiles are narrower compared to the profiles of the perpendicular heat diffusion. For both evaluations (S, $\chi_\perp$) the maximum of the R^2 profiles are shifted between the target (black) and divertor (red) data.

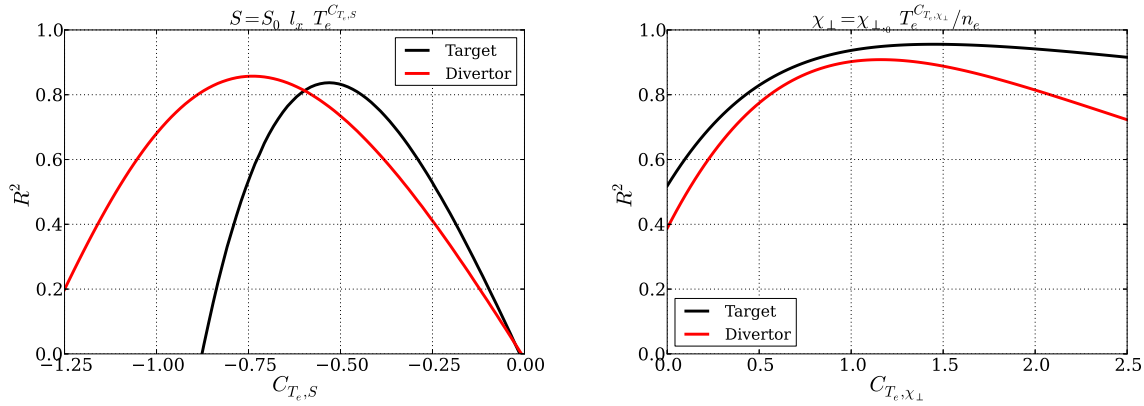

a) Divertor broadening. b) Perpendicular heat diffusivity.

Figure 5.9: Coefficient of determination R^2 in dependence on the exponent of the electron temperature dependence in the respective model for the divertor broadening S and the perpendicular heat diffusivity $\chi_\perp$.

Flux Expansion

For the comparison with different machines, the geometric factors of the divertor and the magnetic equilibrium have to be taken into account. Identical to the procedure for the power fall-off length λ_q (Section 4.3.2) the measured divertor broadening is divided by the flux expansion f_x (eq. 4.13). Since the division by the flux expansion maps the divertor broadening S at the target and in the divertor to the outer mid plane, the values will now be the same for both data sets. The electron temperature and density, however, still differ for both data sets since they are not affected by this geometric mapping. The same sensitivity study shown in figure 5.9 has been conducted for these data sets, the results are shown in figure 5.10.

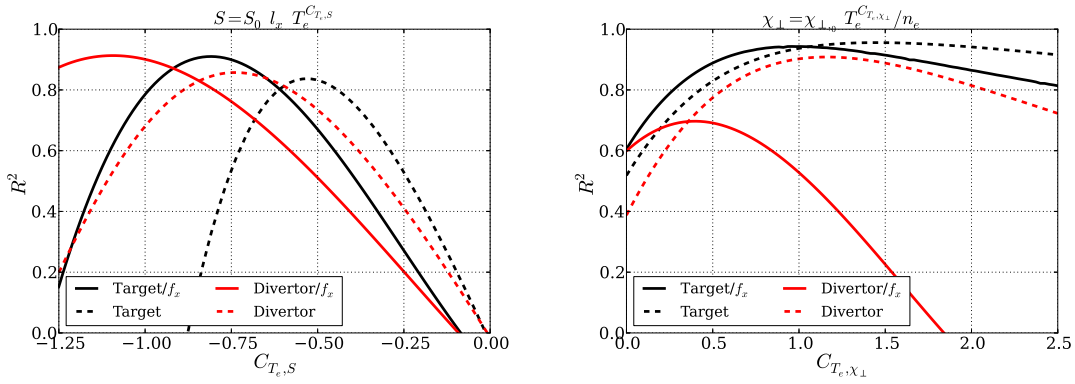

a) Divertor Broadening. b) Perpendicular heat diffusivity.

Figure 5.10: Coefficient of determination R^2 in dependence on the exponent of the electron temperature dependence in the respective model. Solid lines show the data where the measured divertor broadening has been divided by the flux expansion, dashed lines show the values obtained before (fig. 5.9) at the target and in the divertor.

The numerical value of the exponent $C_{T_e,\chi_\perp}$ for the temperature dependence of the perpendicular heat diffusivity changes by roughly 0.5. For the divertor broadening the exponent changes accordingly, following equation 5.27. Furthermore the value of R^2 for the best fit of the divertor broadening increases for both the divertor and the target data when divided by the flux expansion. For the perpendicular heat diffusivity (fig. 5.10b)) the maximum value of R^2 stays about the same for the target (black) but decreases for the divertor data (red).

The reason for the change in the exponent of the temperature dependence becomes obvious when looking at the flux expansion (fig. 5.11). For the data set available the flux expansion and the target electron temperature are correlated (fig. 5.11). Whether this has any physical reason or is just coincidence is left for further studies.

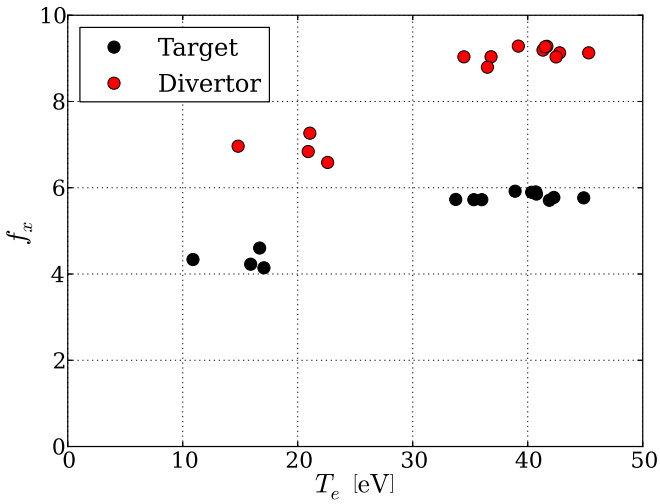

Figure 5.11: Flux expansion on the target and in the divertor volume in dependence on the corresponding electron temperature T_e.

In the following discussion both the divertor broadening with and without flux expansion are shown to give a complete picture. Noted here that the absolute value of the perpendicular heat diffusivity $\chi_\perp$ changes significantly dependent on which geometric mapping for the divertor broadening S is used for the evaluation. In this work no attempt is made to answer which mapping is closest to the real magnitude of the heat transport process in the divertor. Since the measurement on the divertor target plates only results in an *effective* divertor broadening, incorporating the whole diffusive process from the X-point to the divertor target, detailed modelling may reveal the local diffusive processes in the divertor.

The following evaluations were performed for the divertor broadening including the flux expansion. Figure 5.12 shows the fitting results using the model described in equation 5.21 for the perpendicular heat diffusivity for both target (black) and divertor (red) data. Both fits are able to reproduce the derived perpendicular heat diffusivity (eq.

5.19) and the divertor broadening. Note here that the measured divertor temperature alone is able to reproduce the measured divertor broadening S.

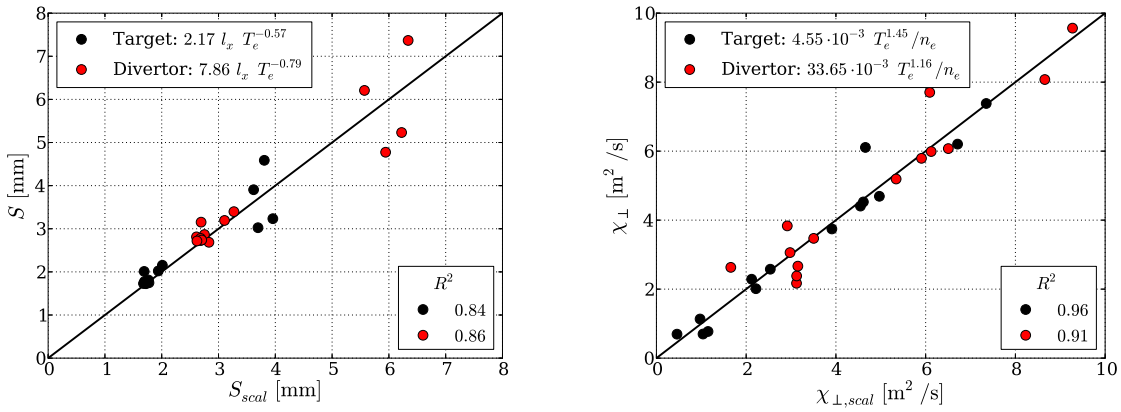

a) Divertor Broadening. b) Perpendicular heat diffusivity.

Figure 5.12: Fitting results for the target and divertor data without flux expansion compensation.

The results for the perpendicular heat diffusivity are as follows:

$$\chi_{\perp,tar} = 4.55 \cdot 10^{-3} \frac{T_e^{1.45}}{n_e} \quad \left[\frac{\mathrm{m}^2}{\mathrm{s}}\right] \tag{5.28}$$

$$\chi_{\perp,div} = 3.37 \cdot 10^{-2} \frac{T_e^{1.16}}{n_e} \quad \left[\frac{\mathrm{m}^2}{\mathrm{s}}\right] \tag{5.29}$$

The exponent of the temperature dependence of the perpendicular heat diffusivity varies roughly between 1 and 3/2 depending on the reference area (target, divertor). The difference of the exponent of the temperature dependence is reduced by a factor of two, since the square root of the perpendicular heat diffusivity enters into the divertor broadening S (eq. 5.13).

$$S_{tar} = 2.17\, l_x\, T_e^{-0.57} \quad [\mathrm{mm}] \tag{5.30}$$

$$S_{div} = 7.86\, l_x\, T_e^{-0.79} \quad [\mathrm{mm}] \tag{5.31}$$

In the following the same study is repeated for the divertor broadening S divided by the flux expansion f_x. The results for the perpendicular heat diffusivity and the divertor broadening are shown in figure 5.13. The fits are able to reproduce the measured perpendicular heat diffusivity well both for the target and the divertor data. The comparably low value of R^2 for the divertor data is presumably be explained in the low value of the exponent of the temperature dependence of this data set of 0.4 (eq. 5.32) in combination with the small relative change in the data of about a factor of two. The measured divertor broadening is reproduced for both fits with equally high values of R^2.

The results for the perpendicular heat diffusivity with the divertor broadening taken

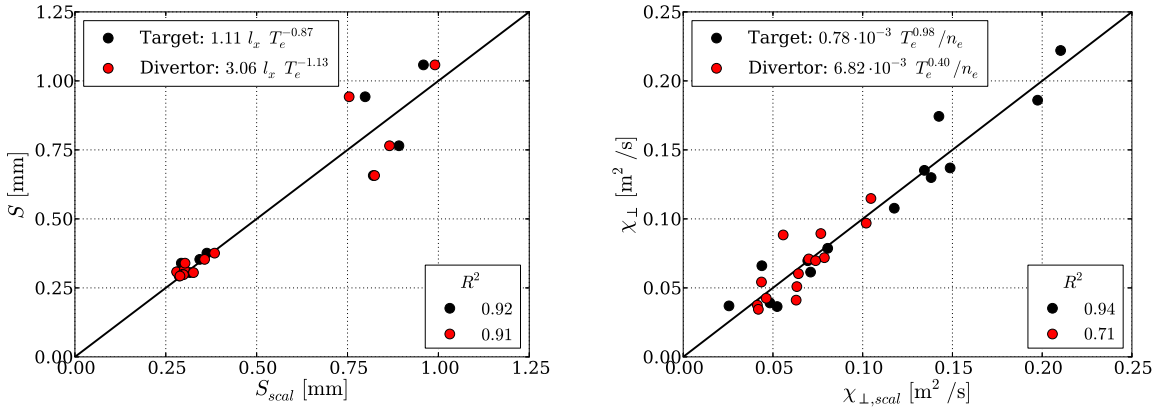

a) Divertor Broadening. b) Perpendicular heat diffusivity.

Figure 5.13: Fitting results for the target and divertor data with flux expansion compensation.

into account are as follows:

$$\chi_{\perp,tar} = 0.78 \cdot 10^{-3} \frac{T_e^{0.98}}{n_e} \quad \left[\frac{\mathrm{m}^2}{\mathrm{s}}\right] \tag{5.32}$$

$$\chi_{\perp,div} = 6.82 \cdot 10^{-3} \frac{T_e^{0.40}}{n_e} \quad \left[\frac{\mathrm{m}^2}{\mathrm{s}}\right] \tag{5.33}$$

For both data sets the exponent of the temperature dependence is reduced compared to the case including the flux expansion (Equations 5.28, 5.29). This is expected considering the correlation between the target electron temperature and the flux expansion in the data set.

$$S_{tar} = 1.11\, l_x\, T_e^{-0.87} \quad [\mathrm{mm}] \tag{5.34}$$

$$S_{div} = 3.06\, l_x\, T_e^{-1.13} \quad [\mathrm{mm}] \tag{5.35}$$

For the divertor broadening the results show that the exponent of the temperature dependence lies roughly between $-3/4$ and -1. The difference in the temperature dependence between target and divertor data can be attributed to the existence of a strong temperature gradient in front of the divertor target for low target temperatures. This study indicates that the temperature dependence of the perpendicular heat diffusivity in the SOL lies between a square root and a linear dependence. Further experimental studies and comparison to simulations are needed to give further insight into the heat transport mechanisms in the SOL. Such studies need to use volumetric parameters, e.g. from divertor HRTS, but are difficult and expensive in nature.

Note here that the increased divertor broadening S for low temperature divertor conditions is not a result of an increased perpendicular transport but the result of the strongly reduced parallel transport. The dependence of the parallel transport on the temperature is larger than for the perpendicular transport. When the temperature

decreases the parallel transport decreases more strongly than the perpendicular transport, increasing the divertor broadening S which is dependent on the ratio between perpendicular and parallel transport (eq. 5.13).

5.3. Comparison to Divertor Transport Models

In the course of time different theoretical and empirical models have been derived for the heat transport of a plasma in the presence of a magnetic field. The measured divertor broadening S is compared to the predictions made by those models. For the following discussion a pure deuterium plasma is assumed where the electron temperature T_e equals the ion temperature T_i.

5.3.1. Classic Heat Diffusion

The first theoretical model looked at is the *classic heat diffusion*. Classic heat diffusion calculates the heat conductivity parallel and perpendicular to the magnetic field for electrons and ions. For the transport along the magnetic field lines the heat conductivity results in [19]:

$$\kappa_{||}^{e} = 4.142 \sqrt{\frac{\pi}{2m_e}} \frac{12\pi\epsilon_o^2}{Z^2 \ln\Lambda\, e} T_e^{\frac{5}{2}} \qquad \approx 4.02 \cdot 10^4 \frac{T_e^{\frac{5}{2}}}{\ln\Lambda} \left[\frac{\mathrm{W}}{\mathrm{m\ eV}}\right] \tag{5.36}$$

$$\kappa_{||}^{i} = 5.53 \sqrt{\frac{\pi}{2m_i}} \frac{12\pi\epsilon_0^2}{Z^4 \ln\Lambda\, e} T_i^{\frac{5}{2}} \qquad \approx 884.5 \frac{T_e^{\frac{5}{2}}}{\ln\Lambda} \left[\frac{\mathrm{W}}{\mathrm{m\ eV}}\right] \tag{5.37}$$

$$\frac{\kappa_{||}^{e}}{\kappa_{||}^{i}} = 0.749 \sqrt{\frac{m_i}{m_e}} \qquad \approx 45 \tag{5.38}$$

Due to the difference between the electron and the ion mass, the contribution of the electrons to the heat conductivity is about 45 times larger than that of the deuterium ions.

$$\kappa_{\perp}^{e} = 6.6 \sqrt{\frac{m_e}{\pi}} \frac{\ln\Lambda\, n_e^2 e^3}{12\pi\epsilon_0^2 B^2} T_e^{-\frac{1}{2}} \qquad \approx 1.24 \cdot 10^{-41} \frac{n_e^2\ \ln\Lambda}{B^2 T_e^{\frac{1}{2}}} \left[\frac{\mathrm{W}}{\mathrm{m\ eV}}\right] \tag{5.39}$$

$$\kappa_{\perp}^{i} = 2 \sqrt{\frac{m_i}{\pi}} \frac{\ln\Lambda\, n_i^2 e^3}{12\pi\epsilon_0^2 B^2} T_i^{-\frac{1}{2}} \qquad \approx 2.27 \cdot 10^{-40} \frac{n_i^2\ \ln\Lambda}{B^2 T_i^{\frac{1}{2}}} \left[\frac{\mathrm{W}}{\mathrm{m\ eV}}\right] \tag{5.40}$$

$$\frac{\kappa_{\perp}^{i}}{\kappa_{\perp}^{e}} \approx 0.3 \sqrt{\frac{m_i}{m_e}} \qquad \approx 18 \tag{5.41}$$

In contrast to the parallel heat transport the main contribution to the perpendicular heat transport is held by the ions. Using the relation between heat conductivity and

heat diffusivity in a plasma (eq. 5.23) the corresponding heat diffusivities are written as.

$$\chi_{||}^{e} = 4.142 \sqrt{\frac{\pi}{2m_e}} \frac{12\pi\epsilon_o^2}{n_e Z^2 \ln\Lambda\, e} T_e^{\frac{5}{2}} \qquad \left[\frac{\mathrm{m}^2}{\mathrm{s}}\right] \tag{5.42}$$

$$\chi_{\perp}^{i} = 2 \sqrt{\frac{m_i}{\pi}} \frac{\ln\Lambda\, n_i^2 e^3}{12\pi\,\epsilon_0^2\, B^2\, n_e} T_i^{-\frac{1}{2}} \qquad \left[\frac{\mathrm{m}^2}{\mathrm{s}}\right] \tag{5.43}$$

Applying the parallel electron and perpendicular ion heat diffusivity to the model of the divertor broadening S (eq. 5.13) the following result is obtained:

$$\begin{aligned} S_{classic} &= l_x \sqrt{\frac{\chi_{\perp}^{i}}{\chi_{||}^{e}}} \qquad [\mathrm{m}] \\ &= l_x \sqrt{\frac{2}{4.142}} \frac{(2m_e m_i)^{\frac{1}{4}}}{\sqrt{\pi}} \frac{Ze^2 \ln\Lambda\, n_i}{12\pi\epsilon_0^2 B} T_e^{-\frac{3}{2}} \\ &\approx 7.52 \cdot 10^{-23} \frac{l_x \ln\Lambda\, n_i}{B T_e^{\frac{3}{2}}} \end{aligned} \tag{5.44}$$

Assuming classic heat diffusion as the transport mechanism, the divertor broadening increases with the electron density n_e, decreases with the magnetic field B and the electron temperature T_e. Figure 5.14 shows the comparison between the classically predicted and the measured divertor broadening S in ASDEX Upgrade L-mode. The measured divertor broadening has been divided by the flux expansion f_x to remove the broadening due to the magnetic and geometric shape of the poloidal flux surfaces and the divertor target.

The classical prediction underestimates the measured divertor broadening. Especially for small values of $S < 0.5$ mm the discrepancy between measurement and prediction is large with factor of about 10–20. From this it is concluded that the perpendicular heat transport in the divertor is not governed by classic diffusion.

5.3.2. Bohm Diffusion

Already in the early years of fusion research Bohm proposed an empirical scaling for the diffusion of a plasma in a magnetic field which is based on the assumption of turbulent transport [36].

$$\chi_{\perp,Bohm} = \frac{1}{16} \frac{T}{eB} \qquad \left[\frac{\mathrm{m}^2}{\mathrm{s}}\right] \tag{5.45}$$

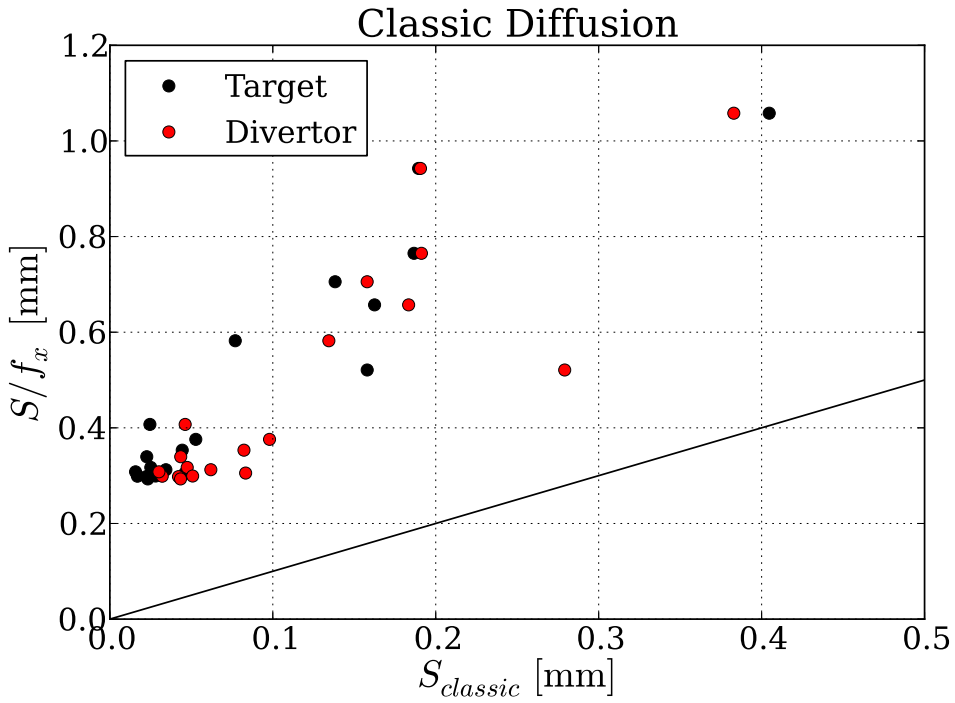

Figure 5.14: Comparison between the divertor broadening as predicted by classic diffusion and measured values for ASDEX Upgrade L-mode discharges.

In contrast to classic predictions, the Bohm heat diffusivity increases with the temperature and decreases only linear with the magnetic field, as compared to the quadratic dependence of classic perpendicular heat diffusion (eq. 5.43). Assuming electron conduction as the parallel heat transport mechanism the divertor broadening results in:

$$S_{Bohm} = l_x \sqrt{\frac{\chi_{\perp,Bohm}}{\chi_{||,e}}} \quad [\text{m}] \tag{5.46}$$

$$= \frac{l_x}{4} \sqrt{\frac{\ln\Lambda Z^2}{4.142 \cdot 12\pi\epsilon_0^2}} \left(\frac{2m_e}{\pi}\right)^{\frac{1}{4}} \frac{n_e^{\frac{1}{2}}}{B^{\frac{1}{2}} T_e^{\frac{3}{4}}} \tag{5.47}$$

$$\approx 4.99 \cdot 10^{-13} \frac{\ln\Lambda^{\frac{1}{2}} n_e^{\frac{1}{2}}}{B^{\frac{1}{2}} T_e^{\frac{3}{4}}} \tag{5.48}$$

The divertor broadening increases with the electron density n_e and decreases with the electron temperature T_e and the total magnetic field B. In figure 5.15 the comparison between the predicted and the measured divertor broadening S is shown.

It is seen that Bohm diffusion overestimates the divertor broadening by a factor of about 2–5. Since the prefactor in the diffusion coefficient (eq. 5.45) has been obtained empirically by fitting measured data, the same has been performed for the divertor broadening S. Fitting the Bohm-like model to the data using by adapting the prefactor results in an about one order of magnitude smaller effective diffusion coefficient in the

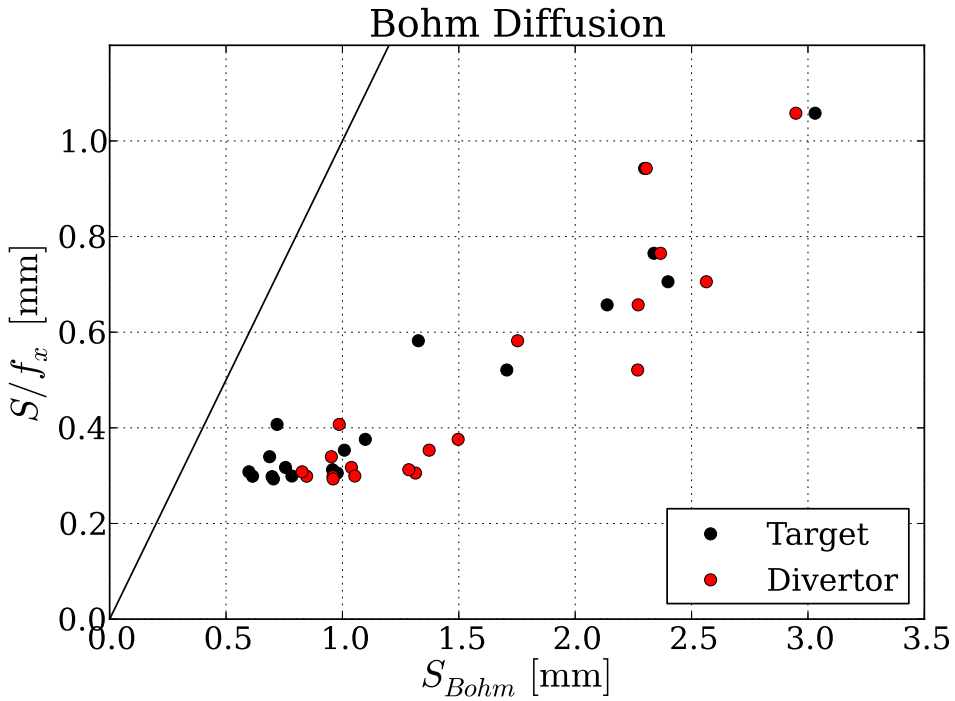

Figure 5.15: Comparison between the measured divertor broadening S and the predicted value using Bohm diffusion.

divertor.

$$\chi_{\perp,Bohm,tar} = 7.7 \cdot 10^{-3} \frac{T}{eB} \quad \left[\frac{\mathrm{m}^2}{\mathrm{s}}\right] \tag{5.49}$$

$$\chi_{\perp,Bohm,div} = 6.0 \cdot 10^{-3} \frac{T}{eB} \quad \left[\frac{\mathrm{m}^2}{\mathrm{s}}\right] \tag{5.50}$$

The results of the fit are shown in figure 5.16. For both the target and the divertor data the measured divertor broadening can be matched by adjusting the pre factor of the perpendicular heat diffusivity. The fitted heat diffusivity reproduces the measured divertor broadening S for both small and larger values.

5.3.3. Gyro-Bohm Diffusion

For the description of measured temperature and density profiles of the confined plasma, especially in JET discharges, the empirical Bohm diffusion has been extended. The main temperature and magnetic field dependence T/eB has been adopted for the new model. In addition a scaling factor was introduced using the ion gyro radius r_g and the typical perpendicular temperature gradient length L_{T_e}. The proposed model

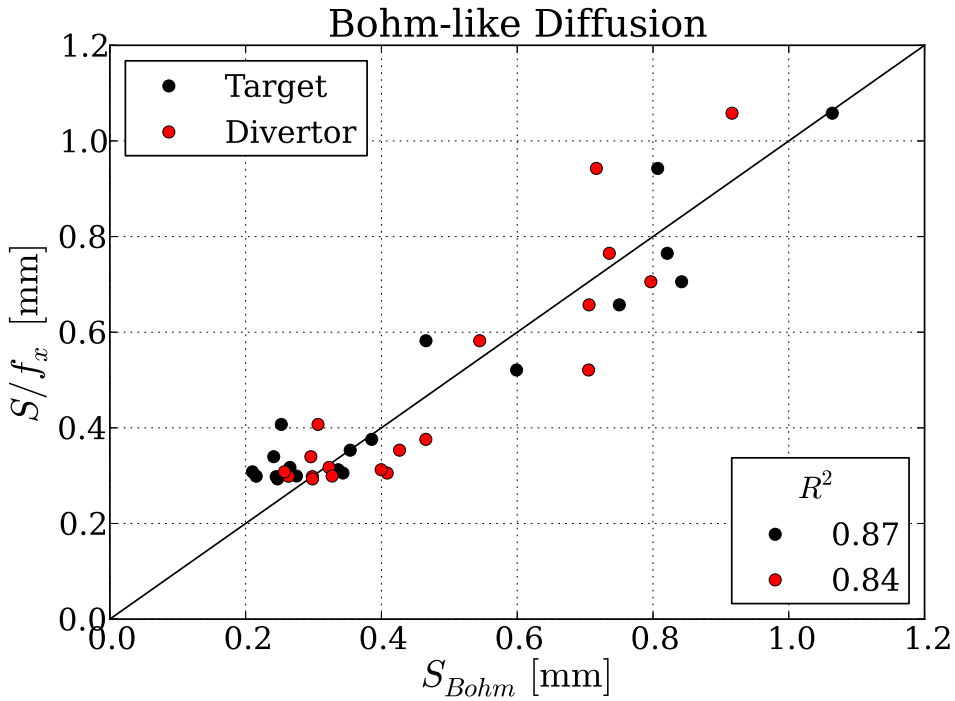

Figure 5.16: Results of the Bohm like fit to the measured divertor broadening.

for Gyro-Bohm diffusion is given as [37]:

$$\chi_\perp = \alpha \frac{T_e}{eB} \frac{r_g}{L_{T_e}} \qquad \left[\frac{\mathrm{m}^2}{\mathrm{s}}\right] \tag{5.51}$$

The temperature gradient length L_{T_e} is defined as follows:

$$L_{T_e} = \frac{T_e}{|\nabla T_e|} \qquad [\mathrm{m}] \tag{5.52}$$

Where $|\nabla T_e|$ is the absolute value of the temperature gradient perpendicular to the magnetic field lines. In order to calculate the perpendicular heat diffusivity the temperature gradient length needs to be known. For the measurements conducted in ASDEX Upgrade L-mode the downstream power fall-off length has been measured which is mapped to the upstream λ_q using the flux expansion f_x. From the two point model (eq. 4.15) the following relation between the power fall-off length λ_q and the temperature fall-off length λ_T is derived for the upstream region [38], assuming that all the power enters the SOL at the upstream position.

$$\lambda_T = \frac{7}{2}\lambda_q \qquad [\mathrm{m}] \tag{5.53}$$

In the following this relation will be used for the temperature gradient length L_{T_e}. With this the perpendicular heat diffusivity is written as follows.

$$\chi_\perp = \alpha \frac{T_e}{eB} \frac{2r_g}{7\lambda_q} \qquad \left[\frac{\mathrm{m}^2}{\mathrm{s}}\right] \tag{5.54}$$
$$= \alpha \frac{(2T_e)^{\frac{3}{2}} \sqrt{m_d}}{7eB^2 q \lambda_q}$$

For the calculation of the heat diffusion the factor α needs to be known. Using equation 5.13 and assuming Gyro-Bohm diffusion for the perpendicular heat transport the divertor broadening S is written as:

$$S_{GB} = l_x \sqrt{\frac{4}{4.142}} \frac{\alpha^{\frac{1}{2}} (m_i m_e)^{\frac{1}{4}} Z \ln\Lambda^{\frac{1}{2}} n_e^{\frac{1}{2}}}{\sqrt{7} B \lambda_q^{\frac{1}{2}} \sqrt{12\pi\epsilon_0^2} T_e^{\frac{1}{2}}} \qquad [\mathrm{m}] \tag{5.55}$$

Since this is an empirical model, α is chosen to get the best fit to the measured divertor broadening. For the target and divertor data the following factors have been found.

$$\alpha_{tar} = 4.5 \cdot 10^{-2} \tag{5.56}$$
$$\alpha_{div} = 3.2 \cdot 10^{-2} \tag{5.57}$$

The comparison between measured and fitted divertor broadening S is shown in figure 5.17. Gyro-Bohm diffusion is able to reproduce the measured divertor broadening S for both small and large values.

5.3.4. Model Summary

In this section the measured divertor broadening S has been compared to SOL transport models. Classic diffusion underestimates the perpendicular heat transport significantly and gives the wrong trend. Therefore it can be deduced that the SOL transport is not governed by classic heat transport. Bohm and Gyro-Bohm like empirical scalings have been derived for ASDEX Upgrade L-modes, both models are able to describe the measured data. The Bohm like model is slightly better in describing the data, having a larger coefficient of determination R^2. However the difference in fit quality is not significant, so that no model is ruled out.

The implication of both models on future devices is discussed. The dependence on the

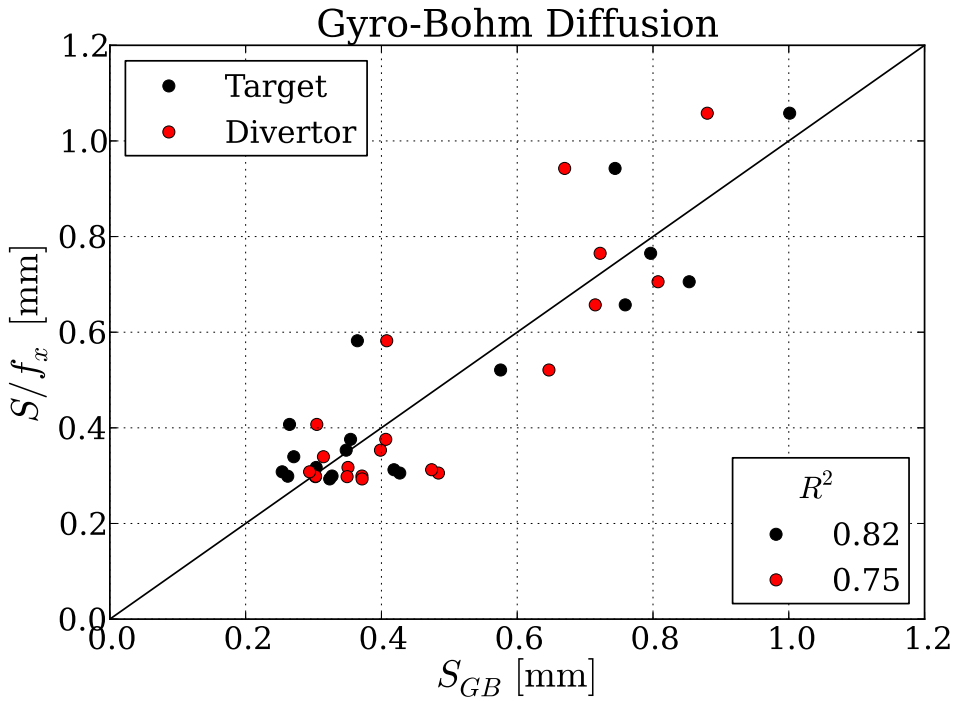

Figure 5.17: Comparison between the measured divertor broadening S and the predicted value using Gyro-Bohm diffusion.

temperature and magnetic field is different for both models:

$$\chi_{\perp,Bohm} \propto \frac{T_e}{B} \tag{5.58}$$

$$\chi_{\perp,Gyro-Bohm} \propto \frac{T_e^{\frac{3}{2}}}{B^2} \tag{5.59}$$

Bohm is inversely proportional to the magnetic field whereas Gyro-Bohm is inversely proportional to the square of the magnetic field. For the temperature an additional square root dependence of the temperature is introduced in Gyro-Bohm compared to the linear dependence of Bohm diffusion. Assuming electron conduction for the parallel heat transport the following dependencies for S can be derived using equation 5.13:

$$S_{Bohm} \propto \frac{n_e^{\frac{1}{2}}}{B^{\frac{1}{2}} T_e^{\frac{3}{4}}} \tag{5.60}$$

$$S_{Gyro-Bohm} \propto \frac{n_e^{\frac{1}{2}}}{B T_e^{\frac{1}{2}}} \tag{5.61}$$

The implications of this is seen when the divertor broadening S in ITER is calculated. Results for assumed low and high density divertor conditions in ITER are shown in table 5.3.

For ITER the Bohm like model estimates a divertor broadening S that is about a

	$\mathbf{T_e}$ [eV]	$\mathbf{n_e}$ [10^{21}m^{-3}]	$\mathbf{S_{Bohm}}$ [mm]	$\mathbf{S_{GB}}$ [mm]
Low Density	20	0.5	1.32	0.73
High Density	10	1.5	3.60	1.67

Table 5.3.: Estimated divertor broadening S for ITER assuming Bohm and Gyro-Bohm like heat diffusion [39].

factor of two larger than the Gyro-Bohm like model. This is the result of the different dependence on the magnetic field. For the operation of ITER the Bohm-like model would be more beneficial. In the next section the empirical scalings (Equations 5.34, 5.35) obtained in section 5.2.1 will by applied to ITER and DEMO to discuss the influence of the divertor broadening S on the target power load.

5.4. ITER and DEMO

Using the scalings for the power fall-off length λ_q (eq. 5.3) and the divertor broadening S (Equations 5.34, 5.35) estimates for the integral power fall-off length λ_{int} and the resulting divertor heat load for ITER and DEMO are attempted. For the scaling towards larger machines, it is assumed that the mechanism causing the divertor broadening is independent on the confinement regime. This is justified by the different location the broadening mechanism acts on compared to the upstream power-fall off length. The H-mode is caused by an edge transport barrier inside the last closed flux surface, whereas it is assumed that the divertor broadening is caused by a diffusive process in the divertor volume between the X-point and the divertor target.

		ITER	**DEMO**
$\mathbf{R}$	[m]	6.2	9.0
$\mathbf{R_{div}}$	[m]	5.5	9.0
$\mathbf{a}$	[m]	2.0	3.0
$\mathbf{l_x}$	[m]	20	30
$\mathbf{B_{tor}}$	[T]	5.3	6.5
$\mathbf{I_p}$	[MA]	15.0	20.3
$\mathbf{P_{fus}}$	[MW]	500	1790
$\mathbf{P_{heat}}$	[MW]	50	50
$\mathbf{P_{SOL}}$	[MW]	120	408
$\mathbf{P_{div,out}}$	[MW]	80	272
$\mathbf{P_{tar,out}}$	[MW]	8.0	27.2

Table 5.4.: Machine parameter of ITER and DEMO. For P_{SOL} and $P_{div,out}$ no radiation was taken into account, $P_{tar,out}$ is the result using 90 % radiative cooling.

Table 5.4 shows various machine parameters for ITER and DEMO. For the power crossing the separatrix P_{SOL} and the power entering the outer divertor $P_{tar,out}$ no

radiative cooling was included. Only for the power arriving onto the outer target $P_{tar,out}$ 90 % of radiative cooling was included. The fraction of radiative cooling is limited by the empirical finding that a sustained H-mode needs a certain amount of power crossing the separatrix [23, 24, 25]. If a too high fraction is radiated in the confined plasma then the plasma will lose its confinement and go into L-mode.

Note that both ITER and DEMO need to be operated with a high fraction of radiative cooling. How this radiative cooling is done in detail and/or where the power is radiated is discussed elsewhere [40, 41, 42, 43, 44]. The divertor connection length l_x is an estimate for both machines including the size of the machine and the typical connection length of ASDEX Upgrade and JET. Using this information and assuming no further size dependence the divertor broadening is calculated (fig. 5.18a)).

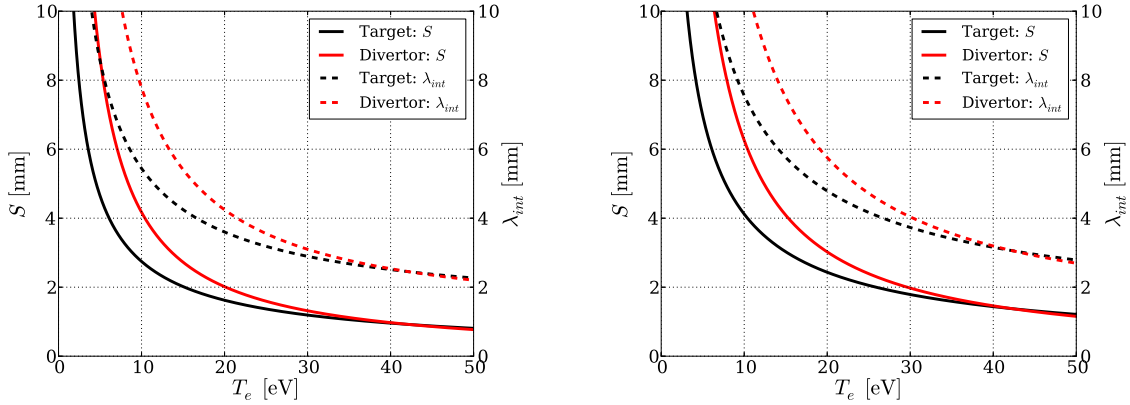

a) ITER b) DEMO

Figure 5.18: Predicted divertor broadening S and resulting λ_{int} for ITER and DEMO in dependence on the respective electron temperature.

The results show a strong increase of the divertor broadening and with it the power deposition width λ_{int} for cold divertor conditions ($T_e < 20$ eV). The discrepancy between the divertor and target data for low temperatures can be explained by the non negligible temperature gradient along the field lines for those conditions. It also becomes apparent, that for low divertor temperatures, which are envisioned for the operation of ITER, the divertor broadening S is the main contribution to the power deposition width λ_{int} (eq. 4.9).

$$\lambda_{int} = \lambda_q + 1.64\,S \qquad \overset{S \gg \lambda_q}{\longrightarrow} \qquad \lambda_{int} \approx 1.64\,S \tag{5.62}$$

The critical value for the design and operation of large fusion devices is not mainly the power deposition width λ_{int} but the resulting peak heat flux density q_{max} on the target. For ITER we have a steady state limit of about 10 $\mathrm{MWm^{-2}}$, for DEMO with about 5 $\mathrm{MWm^{-2}}$ the limit is estimated to be lower due to the high neutron irradiation.

To underline the importance of the divertor broadening S for the heat flux onto the

divertor target an example calculation is performed for ITER and DEMO. Using the power fall-off length λ_q (eq. 5.3) of about 0.9 mm for ITER and about 0.8 mm for DEMO the expected heat flux on the divertor target in the absence of any divertor broadening is calculated.

$$q = \frac{P}{2\pi\, R_{div}\, \lambda_{int}\, f_x\, f_{tor}} \qquad \left[\frac{\mathrm{MW}}{\mathrm{m}^2}\right] \tag{5.63}$$

For the case without radiation the heat flux onto the outer target will be about 600 MWm^{-2} for ITER and over 1.6 GWm^{-2} for DEMO.

Performing the calculation for the case with 90 % radiative cooling results in a heat flux density of about 60 MWm^{-2} for ITER and about 160 MWm^{-2} for DEMO. The heat flux is still too high to be acceptable for steady state operation. These values do not take into account the divertor broadening S. The predictions for the divertor broadening S in dependence on the electron temperature T_e are shown in figure 5.18.

For both devices the divertor broadening increases strongly if the electron temperature at the target (black) falls below 10 eV, which is the lowest temperature available in the L-Mode data used for the scaling of S. In addition, it is seen that even for hot divertor conditions (about 50 eV) with $S \approx 1$ mm, the integral power fall-off length λ_{int} is significantly larger than the upstream power fall-off length. Under these conditions ($T_e \sim 50$ eV) the target heat flux is reduced to about 25 MWm^{-2} for ITER and about 47 MWm^{-2} for DEMO.

For a steady state operation hot divertor conditions are not tolerable due to increased tungsten sputtering, therefore the electron temperature in front of the target has to be low ($T_e < 10$ eV) even if the heat flux at higher electron temperatures would still be tolerable.

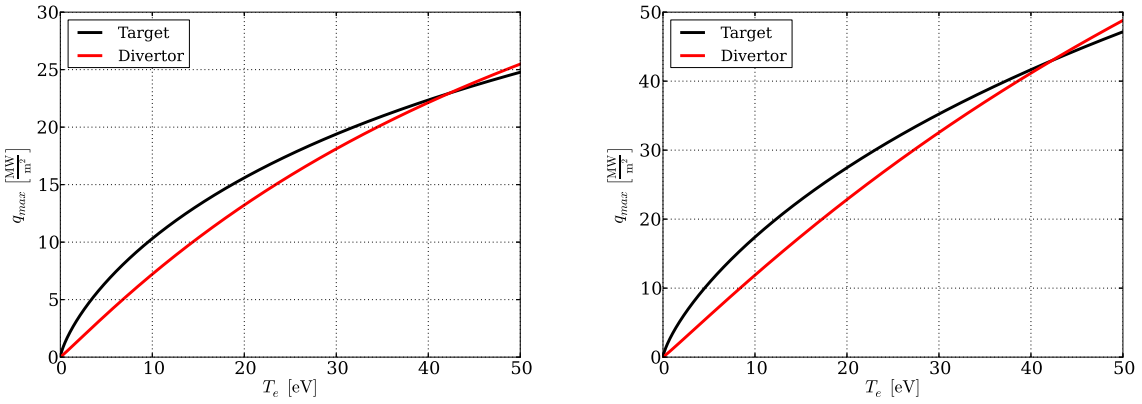

a) ITER b) DEMO

Figure 5.19: Predicted target heat flux for ITER and DEMO depending on the target (black) and divertor (red) temperature, assuming 90 % radiated power.

Using the heat flux limits of 10 $\mathrm{MWm^{-2}}$ for ITER and 5 $\mathrm{MWm^{-2}}$ for DEMO for steady state heat loads, the required divertor electron temperature is calculated, under the assumption of attached divertor conditions and the scalings from equations (5.3) and (5.34). For ITER 10 $\mathrm{MWm^{-2}}$ or less are reached for 10 eV or less. The requirement to reach 5 $\mathrm{MWm^{-2}}$ for DEMO is more challenging resulting in a target temperature of about 2 eV only (fig. 5.19). Note that the assessment of the power load made here does not include the induced target power loads due to radiation and neutrons. Adding these heat fluxes further decrease the acceptable plasma induced heat flux. However, these predictions are based on data with low- and medium recycling divertor conditions. For high-recycling and partially detached divertor conditions λ_{int} in current devices is always observed to increase further.

This study concludes that the current scaling of S leads to the necessity to operate ITER and DEMO with detached divertor conditions ($T_e < 10\,\mathrm{eV}$) and at least 90 % radiative cooling. Whether or not such low temperature divertor conditions can be reached throughout a discharge and sufficiently controlled under reactor conditions will have to be investigated in the future and technical measures have to be developed to ensure safe operation.

Chapter 6

Transient Divertor Power Load

In this section the transient power load onto the divertor target plates induced by edge localised modes (ELM) is discussed. In H-mode plasmas periodic bursts of energy and particles are ejected from the confined plasma, inducing thermal loads on the plasma facing components in the divertor region. While ELMs are tolerable for small and medium sized machines such as ASDEX Upgrade and JET, they pose a possible threat for large devices such as ITER and DEMO [45, 46]. Therefore a detailed understanding of such induced thermal loads is necessary in order to be able to make predictions towards larger machines. The data used for this study was obtained in JET with both carbon [47] and metal plasma facing components. An overview of the parameter range is given in table 6.1.

		JET	
		ITER-like wall	**Carbon**
$\mathbf{B_{tor}}$	[T]	1.0 – 3.1	1.5 – 3.2
$\mathbf{I_p}$	[MA]	1.0 – 3.5	1.5 – 3.5
$\mathbf{P_{SOL}}$	[MW]	3.0 – 22.0	2.2 – 20.3
$\mathbf{T_{e,ped}}$	[keV]	0.3 – 1.2	0.5 – 2.3
$\mathbf{n_{e,ped}}$	[$10^{19}\,\mathrm{m}^{-3}$]	2.0 – 7.0	2.7 – 5.0
$\mathbf{f_{ELM}}$	[Hz]	12 – 109	5 – 78

Table 6.1.: Overview of the parameter range for the JET discharges with both carbon and ITER-like plasma facing components.

6.1. Edge Localised Modes

In the following section a brief introduction into edge localised modes is given based on the review by H.Zohm [48]. In discharges with high confinement the occurrence of fast ($\sim$ ms) periodic events ejecting energy and particles from the confined plasma

is observed in a multitude of devices (e.g. DIII-D, ASDEX, ASDEX Upgrade, JET). These ejections are caused by so-called edge localised modes (ELMs), which are magnetohydrodynamic (MHD) instabilities in the edge of the confined plasma.

Depending on the plasma conditions different types of ELMs exhibiting different characteristics occur. The first classification of different ELM types was given for DIII-D [49]. Three difference ELM types were classified based on:

- The frequency f_{ELM} with which the ELMs occur in dependence on the heating power P.
- The presence of magnetic precursors.
- The MHD stability of the plasma edge with respect to the ideal ballooning criterion [50].

The number for each ELM type has no physical motivation but is a historical convention based on the order in which the ELM types were first observed or discussed.

Type I ELMs exhibit an increasing frequency f_{ELM} with increasing heating power P. At the time of the classification no detectable MHD precursor had been found. The plasma edge is found to be close to the ideal ballooning stability limit [50]. More recent studies in different devices (e.g. ASDEX Upgrade [51], MAST [52], JET [53], JT-60U [54]), however, observed precursors in various signals measuring the electron temperature and density as well as magnetic probes.

Type II ELMs occur in discharges with high triangularity and elongation of the plasma. The frequency is increased compared to type I ELMs and the size is decreased. Type II ELMs are observed in DIII-D and found in high density discharges in ASDEX Upgrade [55].

Type III ELMs show a decrease in frequency f_{ELM} when the heating power P is increased. In addition a magnetic precursor oscillation is observed with a frequency of $50 - -70$ kHz.

Despite the fact that ELMs eject energy from the confined plasma and pose a possible threat for the plasma facing components, they are useful to control the impurity content in the confined plasma. It has been found that only ELMy H-modes become stationary [56]. For future fusion devices such as ITER or DEMO the type I ELMy H-mode is foreseen as the operational scenario.

For type I ELMs an important observation regarding the total ELM energy loss of the plasma has been made for various devices. The product of ELM frequency f_{ELM} and

loss of plasma stored energy due to the ELMs (ΔW) is about constant [57].

$$P_{ELM} = \Delta W \cdot f_{ELM} \approx (0.3 \pm 0.1)\, P_{heat} \qquad \text{for } P_{heat} \gg P_{LH}\,[\text{MW}] \tag{6.1}$$

Where P_{heat} is the total heating power injected into the plasma and P_{LH} the threshold for the LH transition. From this observation it seems favourable to have a high ELM frequency in order to reduce the ejected energy of every single ELM. This relation is the reason why various ELM mitigation techniques are investigated (e.g. pellet pacing, kicks, external magnetic perturbation) aiming for an increase of the ELM frequency.

Figure 6.1 shows the total ELM energy loss in dependence on the ELM frequency for JET with both carbon (JET-C) and metal (JET-ILW) plasma facing components as measured by IR thermography. The trend that the ELM energy loss is decreasing with the ELM frequency is confirmed for both JET-C and JET-ILW. The relation between ELM energy loss and ELM frequency is similar when comparing JET-C (blue) with JET-ILW (red). The average ELM loss power P_{ELM} is about 20 % higher in JET-ILW compared to JET-C, but agree with each other within the uncertainties.

$$P_{ELM,ILW} = 8.0 \pm 3.5 \qquad [\text{MW}] \tag{6.2}$$

$$P_{ELM,CFC} = 6.6 \pm 2.4 \qquad [\text{MW}] \tag{6.3}$$

Considering the scatter in the data we conclude that the type I ELM behaviour is the same for both JET with carbon plasma facing components and JET with ITER-like wall.

The dependence of the ELM energy loss on the ELM frequency gives an estimation for the total energy loss of an ELM for one device only. However, such a scaling does not provide sufficient information to be able to draw conclusions about the resulting heat load of the ELM on the divertor target. In the following sections the critical quantities describing the ELM impact on the target material are defined and discussed.

6.2. Definitions

In this chapter various representative quantities of the ELM induced divertor power load are defined. The benefits and disadvantages with respect to diagnostic access of each quantity are discussed additionally.

IR thermography measures the surface temperature evolution $T(s,t)$ of the target during a discharge. Using the evaluation code THEODOR (Chapter B) the heat flux density $q(s,t)\,[\text{Wm}^{-2}]$ onto the divertor target is derived.

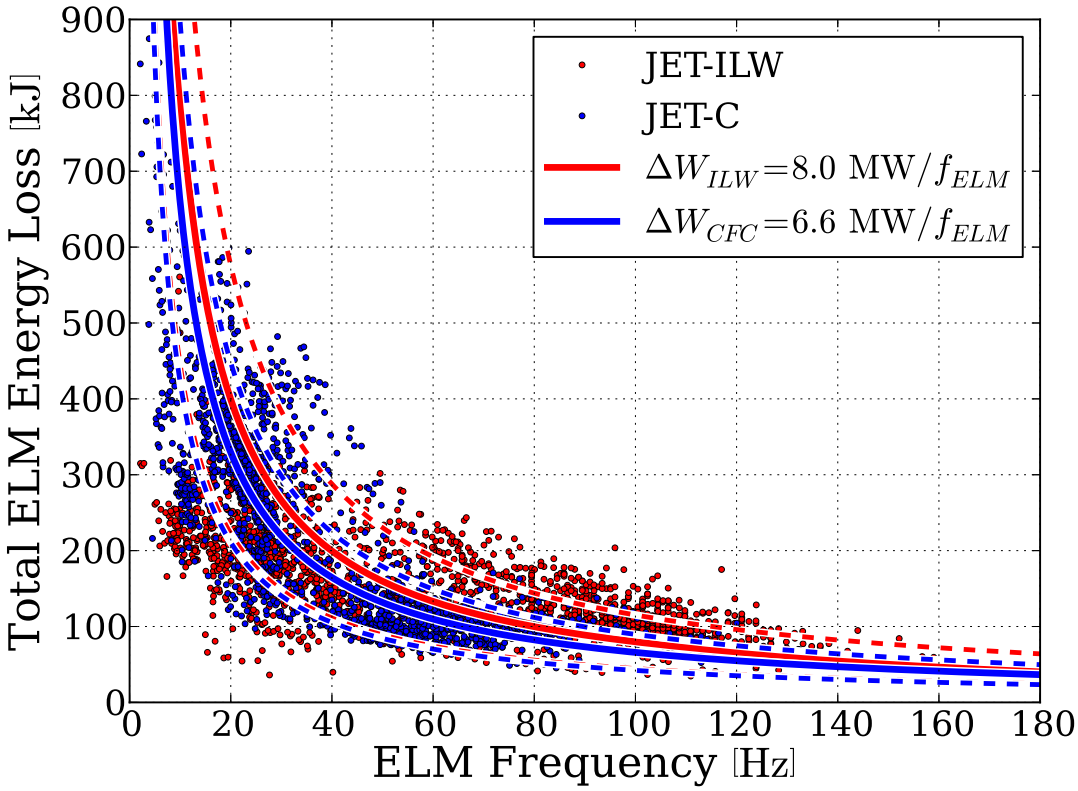

Figure 6.1: Total ELM energy loss in dependence on the ELM frequency for JET-C (blue) and JET-ILW (red).

Figure 6.2 shows the temporal evolution of the heat flux density including an ELM event measured in JET-ILW on the outer divertor target. The nature of the energy deposition of the ELM differs significantly from the steady state heat flux (discussed in chapter 5). The radial energy deposition of one ELM cannot be described with one power fall-off length. The heat flux density exhibits strong local peaks whose locations change with time. These local peaks are attributed to the existence of filaments in the SOL that transport particles and energy into the divertor [58, 59] and onto the first wall. To be able to quantify the load onto the divertor target induced by an ELM, the radial distribution in which the energy is deposited needs to be taken into account.

6.2.1. Peak Heat Flux Density

Since the THEODOR code directly calculates the heat flux density, one quantity that is often used to quantify ELMs [60, 61, 62] is the peak heat flux density q_{max}.

$$q_{max} = \max_{ELM} q(s,t) \qquad \left[\frac{\mathrm{MW}}{\mathrm{m}^2}\right] \tag{6.4}$$

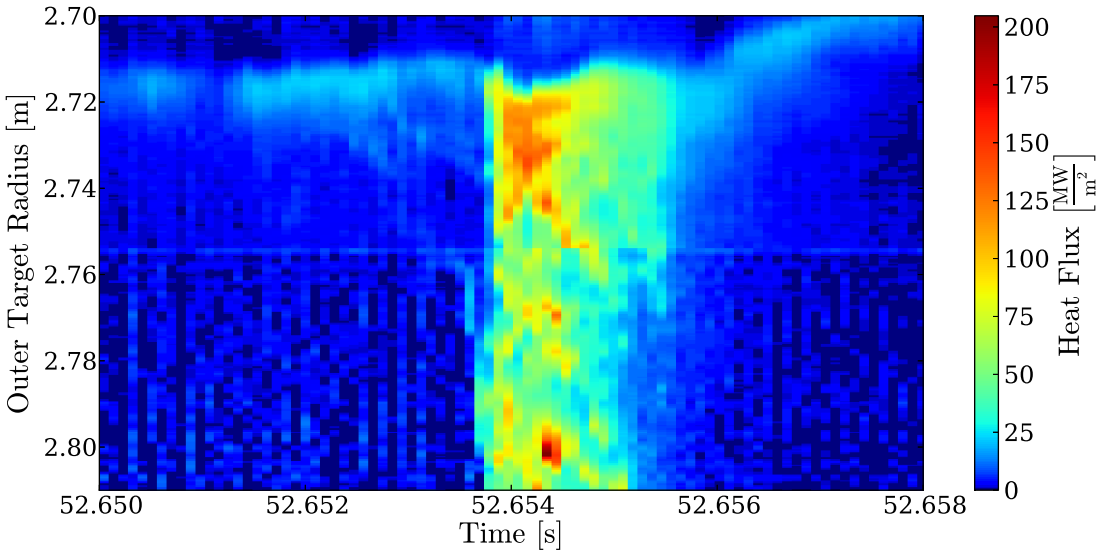

Figure 6.2: Divertor target heat flux in JET-ILW during an ELM.

Note here that the absolute value of the peak heat flux density is influenced strongly by the heat transfer coefficient α as discussed in section 2.4. A detailed discussion of the measured peak heat flux density in JET-ILW and JET-C is given in section 6.5.1.

6.2.2. Peak Power Load

The total power load $P(t)$ onto the divertor target is calculated by integration of the heat flux density $q(s,t)$ over the surface of the divertor target.

$$P(t) = 2\pi R_{div} f_{tor} \int_{target} q(s,t)\mathrm{d}s \qquad [\mathrm{MW}] \qquad (6.5)$$

Where R_{div} is the major radius of the divertor and f_{tor} is the toroidal wetted fraction. In order to prevent the toroidal edges of the target tiles from overheating the tiles are inclined toroidally to shadow the leading edges of each tile by the neighbouring tile. This inclination reduces the toroidal circumference that is exposed to the plasma effectively reducing the target area. The ratio between actual plasma exposed target area and the area if the target would consist of one large seamless surface is called the *toroidal wetted fraction* f_{tor}. For ITER with castellated targets the achievable wetted fraction is around 75 % [63], for JET-ILW it is about 50 %.

Having calculated the divertor power load $P(t)$ the peak power load during an ELM is determined.

$$P_{max} = \max_{ELM} P(t) \qquad [\mathrm{MW}] \qquad (6.6)$$

The peak power load denotes a target integrated quantity, the total energy flux into the divertor. When using this quantity one has to be careful to interpret it correctly. There are two main challenges which have to be considered. The first one becomes obvious when looking at the measurement of the ELM heat flux density.

Figure 6.2 shows an ELM measured in JET-ILW. The ELMs radial power deposition has a larger extent compared to the inter-ELM heat flux and the IR system has to be able to capture the whole area that energy is deposited onto. This has to be taken into consideration when comparing measurements from different machines, experiments (strike line position) and/or IR systems. The second difficulty is the assumed toroidal symmetry of the energy deposition. Whereas toroidal symmetry is a valid assumption for the inter-ELM heat transport in absence of external magnetic perturbations, ELM heat transport is carried by filaments together with the occurrence of ergodic structures close to the separatrix. These transport mechanisms are toroidally asymmetric so that the toroidally localised IR measurement is not able to cover the whole energy deposition process. Therefore the peak power load has to be handled with care and systematic short comings have to be taken into consideration.

6.2.3. ELM Duration

So far in this thesis only one reference time has been used to characterise the ELM either by the peak heat flux q_{max} or the peak power load P_{max}. It is seen in figure 6.2 that an ELM has a temporal extent during which energy is deposited above the steady state level. The exact determination when the ELM starts and when it ends is elusive because the understanding of the development of ELMs is incomplete and moreover not measured precisely. Since this work is focusing on the ELM energy deposition on the target, the ELM duration is defined using the measured heat flux onto the divertor target.

For the operation of JET-ILW and JET-C [47] a robust signal to determine the ELM duration is the power load $P(t)$.

Figure 6.3 shows the temporal evolution of the power load $P(t)$ for three ELMs in different discharge in JET-ILW. The duration of the increased power load varies significantly ($\sim$ factor 3) among the different ELMs, but in all cases the temporal profile shows a pronounced maximum. The shape of the ELM power load has a distinct maximum. This facilitates to define the beginning and end of the ELM. A convenient reference time for ELMs is the time t_0 when the peak power load P_{max} is present.

$$P(t = t_0) = P_{max} \qquad [\mathrm{MW}] \qquad (6.7)$$

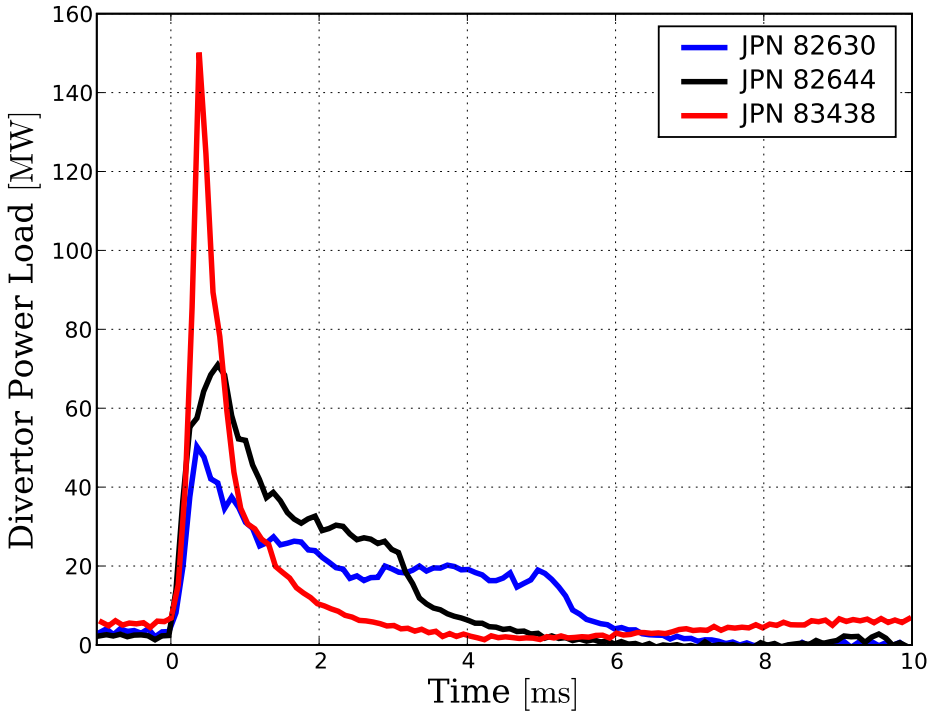

Figure 6.3: Example of the temporal power load evolution for ELMs with different durations.

The beginning of the ELM is defined when the power load first exceeds $1/e$ of the peak power load of the ELM.

$$P\left(t_{begin}\right) = \frac{P_{max}}{e} \qquad t < t_0\,[\mathrm{MW}] \tag{6.8}$$

For the end of the ELM the according definition is chosen, namely when the power load falls below $1/e$ of the peak power load.

$$P\left(t_{end}\right) = \frac{P_{max}}{e} \qquad t > t_0\,[\mathrm{MW}] \tag{6.9}$$

The ELM duration is now given as the difference between ELM end and begin.

$$\tau_{ELM} = t_{end} - t_{begin} \qquad [\mathrm{s}] \tag{6.10}$$

Note here that this definition of the ELM duration does not represent a generalized description of the beginning and end of the ELM. It was chosen to give a robust estimate of the ELM duration over a large number of discharges for the interpretation of the ELM heat fluxes. For a more detailed insight in the onset and termination of ELMs fast upstream diagnostics have to be consulted.

6.2.4. Energy

Having defined the ELM duration, the ELM deposited energy is calculated by integrating the power load $P(t)$ over the ELM duration t_{ELM}.

$$W_{ELM} = \int_{t_{begin}}^{t_{end}} P(t)\mathrm{d}t \qquad [\mathrm{kJ}] \tag{6.11}$$

For the available discharges only the outer divertor target has been observed and the limitations discussed for the power load $P(t)$ occurring due to the narrow view of the IR system apply here as well. To have a complete picture of the ELM energy loss both the inner and outer divertor should be observed eventually. It is reported, that the same or more energy of an ELM is deposited on the inboard target [11].

6.2.5. Energy Fluency

The energy fluency $\epsilon(s)$ is obtained by integrating the heat flux density $q(s,t)$ over the ELM duration t_{ELM}.

$$\epsilon(s) = \int_{t_{begin}}^{t_{end}} q(s,t)\mathrm{d}t \qquad \left[\frac{\mathrm{kJ}}{\mathrm{m}^2}\right] \tag{6.12}$$

The energy fluency $\epsilon(s)$ is the deposited energy density on the target and therefore contains information about the local load induced by the ELM. For the quantification of the ELM the peak value is used similar to the peak heat flux density q_{max} (eq. 6.4).

$$\epsilon_{max} = \max_{ELM} \epsilon(s) \qquad \left[\frac{\mathrm{kJ}}{\mathrm{m}^2}\right] \tag{6.13}$$

Figure 6.4 shows an example of the energy fluency $\epsilon(s)$ of a single ELM (fig. 6.2) in JET-ILW (black) together with the corresponding inter-ELM energy fluency integrated over the same duration before the ELM event.

The energy density deposited during the ELM (black) is significantly higher than for the reference inter-ELM time interval (red). The ELM energy fluency profile exhibits a multitude of localised maxima associated with the filaments transporting the energy to the target. The radial extent of the energy deposition is considerably larger than for the inter-ELM transport.

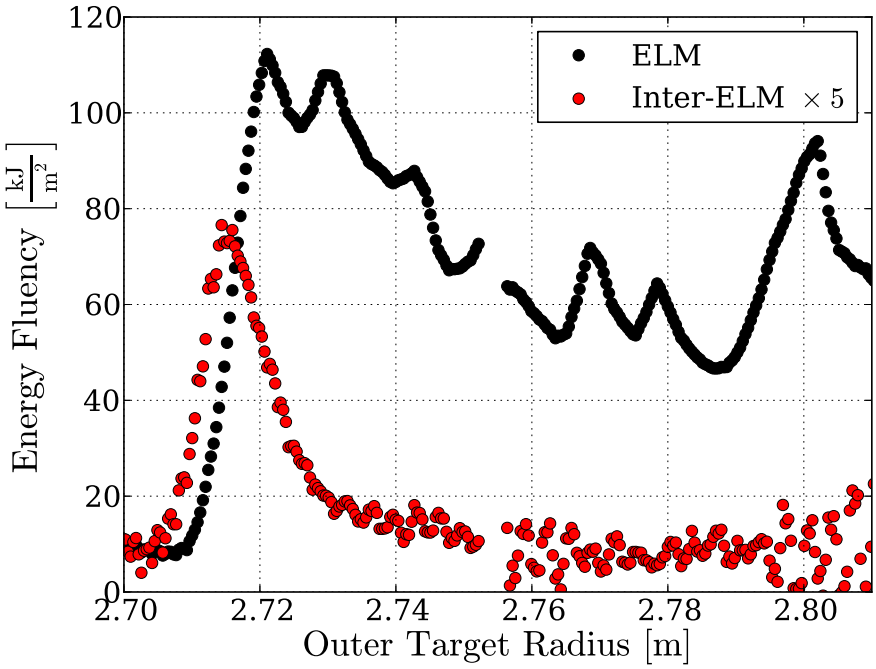

Figure 6.4: Example for the ELM deposited energy fluency (black) and the corresponding inter-ELM fluency (red) in JET-ILW.

6.3. Heat Impact Factor

For the evaluation of the fatigue induced onto the divertor target plates one first has to know the crucial limits of the target. The fatigue/damage of the target material caused by transient heat loads is in zeroth order proportional to the transiently reached surface temperature [64].

For short events ($\sim$ ms) the heat diffusion in the target plate can be assumed to be mainly perpendicular to the surface and the temperature rise is calculated using the one dimensional semi-infinite approach [12]:

$$\Delta T_{surf} = \frac{2}{\sqrt{\pi}} \frac{q}{\sqrt{\kappa \rho c_p}} \sqrt{t} \qquad \text{[K]} \qquad (6.14)$$

Where q is the heat flux density and t the duration of the ELM. κ is the heat conductivity, ρ the density and c_p the specific heat capacity of the target. Note here that a constant heat flux density q needs to be assumed for the calculation of the temperature rise ΔT_{surf}.

Equation 6.14 allows the estimation of the temperature increase for a given heat flux density q and deposition duration t. This quantity is called the *heat impact factor*.

For a temporal constant heat flux density the following relation is valid:

$$\epsilon = q \cdot t \qquad \left[\frac{\mathrm{kJ}}{\mathrm{m}^2}\right] \tag{6.15}$$

Applying this relation to equation 6.14 the heat impact factor is expressed in dependence of the energy fluency ϵ.

$$\Delta T_{surf} = \frac{2}{\sqrt{\pi}} \frac{\epsilon}{\sqrt{\kappa \rho c_p}} \frac{1}{\sqrt{t}} \qquad [\mathrm{K}] \tag{6.16}$$

For the same deposited energy density ϵ on the target, the surface temperature increase ΔT_{surf} decreases with the square root of the ELM duration. For an acceptable life time of the divertor target in ITER, a limit of the ELM deposited energy fluency of $\epsilon = 500\ \mathrm{kJm^{-2}}$ has been found, assuming an ELM duration of 750 µs [64, 65].

This consideration already reveals an important feature when discussing transient heat loads. The impact on the target is not dependent on the total amount of energy deposited on the target, but depends on the local energy density. In terms of material fatigue there is no difference between a large ELM depositing its energy on a large area compared to a small ELM depositing on an equally small area. This has to be taken into account when discussing e.g. ELM mitigation, where a pure reduction of the total ELM loss energy might not be sufficient to protect the divertor target if the area of the energy deposition shrinks in the same way keeping the energy fluency constant.

6.4. Database

For the study of ELM induced transient heat loads on the outer horizontal divertor target plates, dedicated discharges have been performed in JET-C. After the change to the ILW, those discharges have been repeated (Figures 6.5 and 6.6). The discharges in JET-ILW were conducted with a higher gas fueling rate Γ_D compared to JET-C to prevent impurity accumulation [66]. A first set of first comparison discharges were conducted with low heating power of up to 10 MW (fig. 6.5).

The pedestal conditions reached in these low power discharges in JET-ILW were different compared to JET-C. The pedestal electron density $n_{e,ped}$ was higher for JET-ILW, while the pedestal electron temperature $T_{e,ped}$ was lower compared to JET-C.

In a second set of discharges using higher heating power of up to 26 MW, the pedestal conditions in JET-ILW were closely matched to those observed in JET-C (fig. 6.6). However the highest pedestal pressure achieved in JET-C could still not be reproduced in JET-ILW.

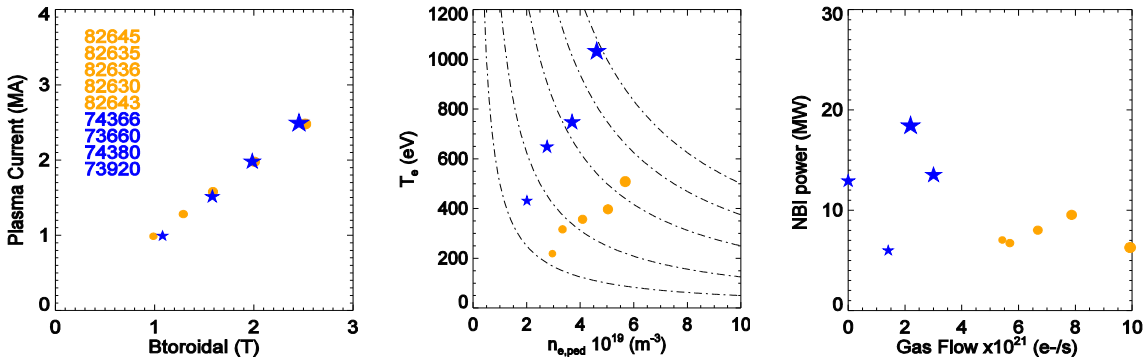

Figure 6.5: Comparison of dedicated discharges between JET-C and JET-ILW at low heating power ($P_{heat} < 10$ MW).

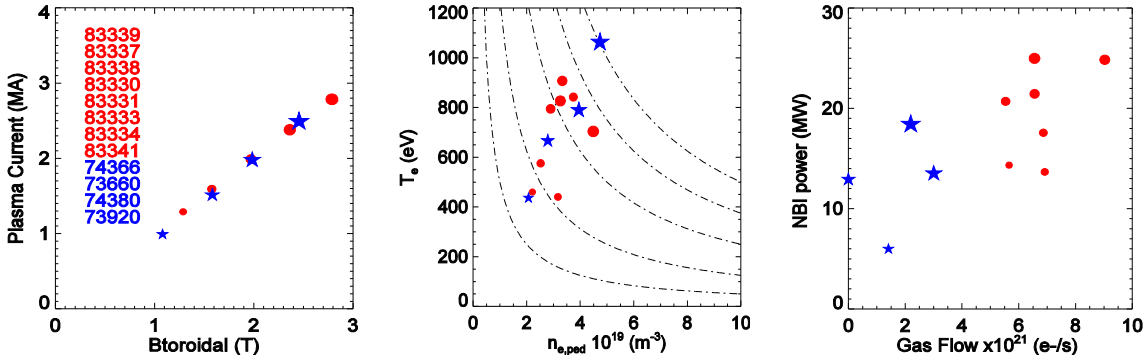

Figure 6.6: Comparison of dedicated discharges between JET-C and JET-ILW at high heating power ($P_{heat} > 10$ MW).

It is observed, that the higher gas fueling in JET-ILW requires a higher heating power, in order to reach the same pedestal conditions as reached in JET-C with lower (or no) gas fuelling. For all discharges the pedestal conditions were evaluated using the **H**igh **R**esolution **T**homson **S**cattering (HRTS) system [21].

The discharges in the database used for the following discussion are type-I ELMy H-modes. Discharges using advanced scenarios or external ELM triggering (pellets, kicks, etc) were not considered.

6.5. Experimental Results

In the following section the previously defined quantities peak heat flux, ELM duration and energy fluency are presented using data from both JET-C and JET-ILW. The differences and similarities between JET-C and JET-ILW are shown. Possible extrapolations towards larger devices are discussed.

6.5.1. Heat Flux

As stated earlier, one of the most common quantity to specify the ELM impact on the divertor target is the heat flux $q(s,t)$. At the first look this quantity might seem appropriate as a qualifier, however, one has to take into account the nature of ELMs. In contrast to the steady state power load, the ELM power load is not evenly distributed onto the divertor target (fig. 6.2).

During ELMs short lived filaments (~ 100 µs) deposit energy very localised (~ 1 mm) on the divertor target. These filaments themselves are distributed on a large area compared to the inter-ELM wetted area (fig. 6.2). In addition ergodic structures deposit energy on the target. Both these processes are not toroidally symmetric. Since the IR system is observing a fixed toroidal position in the tokamak the heat flux measured during an ELM is not necessarily the maximum heat flux over the entire toroidal circumference.

Another critical point that has to be taken into consideration when using the heat flux $q(s,t)$ is the measurement itself. As discussed in section 2.4 the measured value during transient heat loads is sensitive to the surface conditions of the target. Not knowing the heat transfer coefficient α for the target can result both in over- or underestimated heat fluxes. This error source is especially pronounced on carbon targets where the surface properties change due to layer deposition [14]. For this reason the results from JET-C are omitted in the discussion of the heat flux and only JET-ILW data is shown.

For the energy and particle exhaust during ELMs the so called **F**ree **S**treaming **P**article (FSP) approach was proposed [67, 68]. This model assumes that the energy during ELMs is transported along the magnetic field lines by free streaming ions. Under the assumption of a Maxwellian velocity distribution upstream and an energy/particle ejection time that is shorter than the parallel transport time in the SOL the parallel peak power load of the ELM follows as [67]:

$$\begin{aligned} q_{||,FSP} &= 0.27\, c_s\, p_{e,ped} && \left[\frac{\mathrm{MW}}{\mathrm{m}^2}\right] \\ &= 0.27 \sqrt{\frac{T_{e,ped}}{m_p}}\, p_{e,ped} \\ &= 0.27\, T_{e,ped}^{3/2}\, n_{e,ped}\, m_p^{-1/2} \end{aligned} \tag{6.17}$$

Where c_s is the ion sound speed in m/s, $p_{e,ped}$ the pedestal top pressure in Pa, $T_{e,ped}$ the corresponding electron temperature in eV, $n_{e,ped}$ the electron density in $10^{19}\mathrm{m}^{-3}$ and m_p is the proton mass in eV/c^2. For energy/particle ejection times that are longer than the parallel SOL transport time the factor 0.27 changes to about 0.55 [69]. The

comparison between predicted and the measured divertor power load in JET-ILW is shown in figure 6.7.

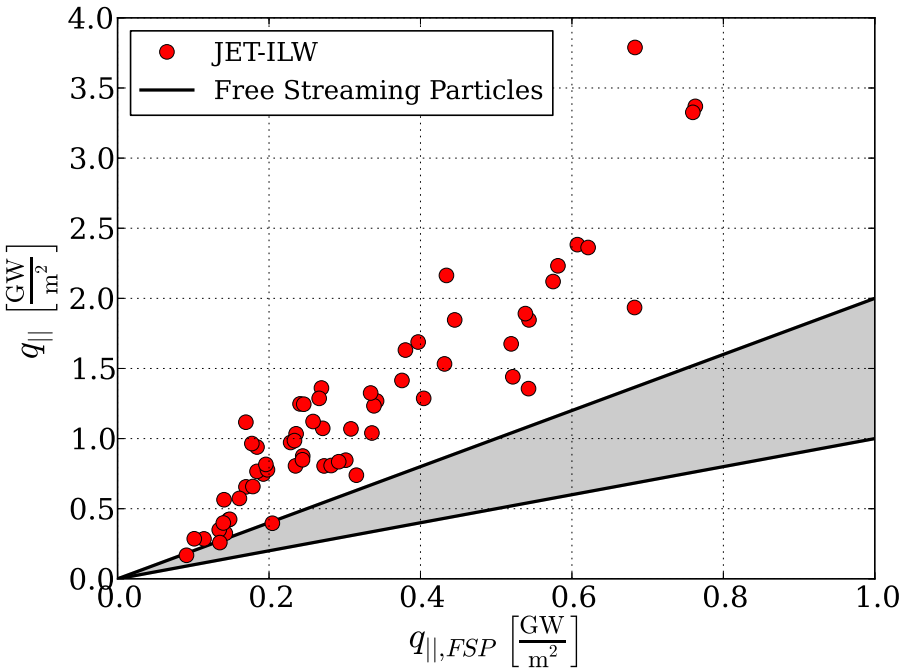

Figure 6.7: Measured peak power load in JET-ILW against the prediction using the free streaming approach during ELMs.

The prediction (gray) of the peak heat flux systematically underestimates the measured peak heat flux by about a factor of two. The relative scatter of the data lies within the expected scatter due to different ELM durations. The overall trend of the peak heat flux is reproduced by the free streaming particle approach. Further studies of the peak heat flux including data from other machines (e.g. ASDEX Upgrade) have to be conducted in order to gain further insight in the ELM energy transport.

6.5.2. ELM Duration

For the assessment of the ELM induced load onto the divertor target the heat impact factor is an important quantity (eq. 6.16), which is dependent on the ELM duration t_{ELM}. In order to assess the ELM duration in dependence of the plasma conditions, pedestal data obtained by HRTS is used. Figure 6.8 shows a comparison of the pedestal conditions (electron temperature $T_{e,ped}$ and density $n_{e,ped}$) reached in JET-C and JET-ILW. The probability distributions of the ELM duration are shown in figure 6.8b). The average ELM duration observed in JET-ILW of ~ 2 ms is longer compared to JET-C with ~ 750 µs.

For the database the width of the distribution is larger for JET-ILW compared to JET-

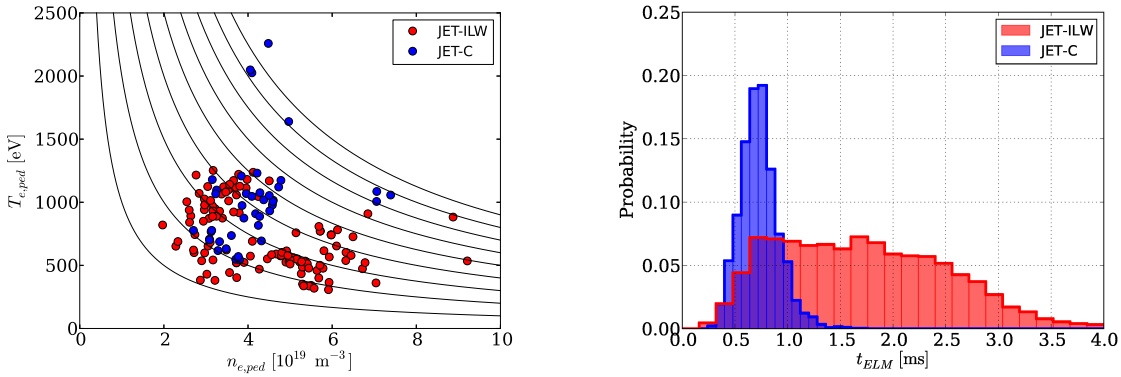

a) Pedestal electron temperature and density with lines of constant pressure (black).

b) Probability distribution of the observed ELM duration [33].

Figure 6.8: Pedestal conditions (electron temperature and density) and observed ELM duration for the dedicated discharges in JET-C (blue) and JET-ILW (red).

C. However, the shortest ELMs observed in JET-ILW have a duration comparable to that observed in JET-C.

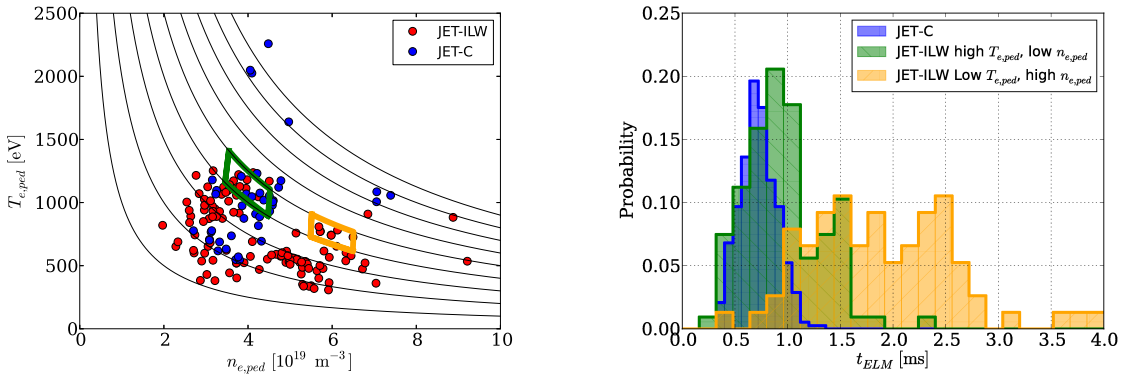

a) Pedestal electron temperature and density with lines of constant pressure (black).

b) Probability distribution of the observed ELM duration.

Figure 6.9: Pedestal conditions (electron temperature and density) and observed ELM duration for the dedicated discharges in JET-C (blue) and JET-ILW (red) [33].

The pedestal conditions observed in the JET-ILW database differ from those observed in JET-C. The composition of the pedestal pressure $p_{e,ped}$ is different. For JET-C the pedestal temperature reached high values ($T_{e,ped} \sim 2$ keV) with pedestal densities around $4 \cdot 10^{19}$ m^{-3}. In JET-ILW the pedestal pressure is formed by a higher pedestal density of up to $9 \cdot 10^{19}$ m^{-3} and electron temperatures of up to 1.2 keV. For the study of the influence of the wall material on the ELM duration, discharges with similar pedestal conditions are compared.

Figure 6.9 shows the comparison of JET-ILW and JET-C with similar pedestal condi-

tions (green). For those conditions the average ELM duration in JET-ILW is similar to the ELM durations observed in JET-C. The ELMs in JET-ILW are slightly longer and the distribution is wider but there is no significant difference of the ELM duration between the two wall materials. The ELM duration in JET-ILW at a constant pedestal pressure, but higher pedestal density (gold), shows longer ELMs with a wider distribution.

For a more detailed analysis of the ELM duration at JET only baseline H-mode discharges without external ELM triggering (e.g. pellets, kicks) are considered. The measured ELM duration τ_{ELM} has been fitted using the following nonlinear regression.

$$\tau_{ELM,reg} = \tau_0 \, T_{e,ped}^{C_T} \, n_{e,ped}^{C_n} \left(\frac{\Delta W}{W}\right)^{C_{\Delta W}} \quad \text{[ms]} \tag{6.18}$$

Where $T_{e,ped}$ is the pedestal temperature in eV, $n_{e,ped}$ the pedestal density in $10^{19}\mathrm{m}^{-3}$ and $\Delta W/W$ the relative loss of stored energy in percent. C_T, C_n and $C_{\Delta W/W}$ are the respective exponents used for the fitting. The results of the nonlinear regression are shown in table 6.2.

	$\boldsymbol{\tau_0}$ [ms]	$\mathbf{C_T}$	$\mathbf{C_n}$	$\mathbf{C_{\Delta W/W}}$	$\mathbf{R^2}$
JET-ILW	11.68 ± 6.70	$-0.48\,(07)$	$0.53\,(09)$	$0.12\,(11)$	0.69
	14.12 ± 7.57	$-0.48\,(07)$	$0.53\,(09)$		0.69
	90.91 ± 48.77	$-0.65\,(09)$			0.50
	0.46 ± 0.09		$0.79\,(11)$		0.45
JET-C	1.57 ± 0.87	$-0.03\,(09)$	$-0.33\,(20)$	$-0.12\,(09)$	0.23
	1.84 ± 1.01	$-0.07\,(09)$	$-0.41\,(19)$		0.19
	1.86 ± 1.08	$-0.15\,(09)$			0.08
	1.28 ± 0.30		$-0.47\,(17)$		0.18
JET-ILW + JET-C	43.52 ± 23.64	$-0.70\,(07)$	$0.61\,(10)$	$0.04\,(10)$	0.67
	43.06 ± 23.30	$-0.69\,(07)$	$0.61\,(11)$		0.67
	302.97 ± 149.55	$-0.85\,(09)$			0.55
	0.23 ± 0.06		$-1.11\,(16)$		0.32

Table 6.2.: Results of nonlinear regressions of the ELM duration for JET.

The regressions using the JET-ILW and JET-ILW + JET-C data show a similar trend. The ELM duration increases with density and decreases with temperature. Regressing JET-C alone does not give a useful result since the data has only a small variation in the ELM duration. The ELM duration is independent of the relative loss of stored energy. The results with either temperature or density alone do not reproduce the measured ELM duration. It is concluded that the ratio of the pedestal density and temperature determine the duration of the ELM. The result from the regression using both datasets and the pedestal temperature and density is shown in figure 6.10.

It is seen that the ELM duration in JET-ILW covers a larger span compared to the

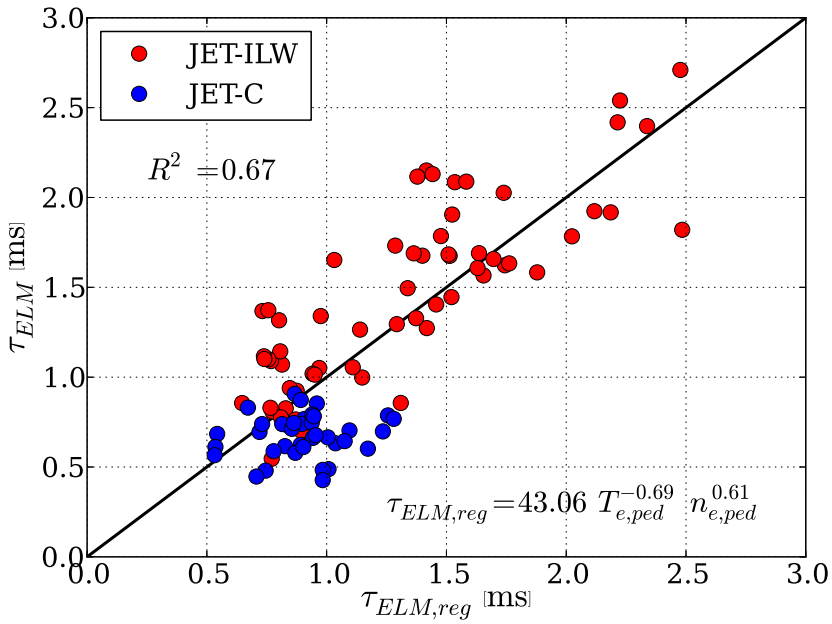

Figure 6.10: Regression results for the duration of the ELM heat deposition using data from JET-C and JET-ILW.

ELM duration in JET-C and are in average longer. The shortest ELMs in JET-ILW however are in the range of the JET-C ELMs. From this it can be seen, that the ELM duration in JET-ILW behaves the same way as the ELM duration in JET-C. The difference is a result of the different pedestal composition encountered in data analysed for JET-ILW.

In the following a linear dependence of the ELM duration on the machine size R due to the increasing connection length in the SOL is assumed. The empirical scaling using the pedestal temperature and density is applied to the foreseen pedestal temperatures and densities in ITER and DEMO.

		ITER	**DEMO**
$\mathbf{T_{e,ped}}$	[keV]	4.3	8.0
$\mathbf{n_{e,ped}}$	[10^{19} m^{-3}]	8.0	7.3
$\boldsymbol{\tau}_{\mathbf{ELM,ILW,C}}$	[ms]	0.94	0.85
$\boldsymbol{\tau}_{\mathbf{ELM,ILW}}$	[ms]	1.52	1.57

Table 6.3.: ELM duration for ITER and DEMO resulting from the empirical scaling found using combined data from JET-ILW and JET-C (tab. 6.2).

For ITER the empirical scaling using JET-ILW data alone results in an ELM duration of around 1.52 ms, for DEMO the result is about 1.57 ms. The scaling using both data from JET-ILW and JET-C results in an ELM duration of about 940 µs and 850 µs for ITER and DEMO respectively. The scaling using both data sets results in an ELM duration that is about a factor of two smaller than the JET-ILW alone scaling predicts.

Note here that the scaling using both JET-ILW and JET-C predicts ELM durations which are close to the estimation for the energy deposition times for ITER [64, 65] used for material testing. No conclusion is drawn which of the two scaling is more suitable to predict the ELM duration for future devices. Further studies including different devices are necessary to gain further insight into the dependence of the ELM duration on the plasma conditions and the machine size.

6.5.3. Energy Fluency

In the heat impact factor (eq. 6.16) the energy fluency ϵ (eq. 6.12) is an important quantity. Having a detailed understanding of the dependence of the energy fluency on the plasma conditions is critical to estimate the life time of the divertor target. In the following the peak energy fluency (eq. 6.13) is used as a measure for the ELM induced energy fluency. To be able to compare different geometries, the effective toroidal pitch angle has to be taken into account, which results in the energy fluency parallel to the magnetic field lines $\epsilon_{||,max}$.

Figure 6.11 shows the measured parallel peak energy fluency $\epsilon_{||,max}$ on the outer divertor target for JET-C (blue) and JET-ILW (red) in dependence on the electron pedestal pressure $p_{e,ped}$. For both data sets the pressure is able to order the measured peak energy fluency. The peak energy fluency in JET-ILW shows overlap with the data obtained in JET-C. This finding is interesting since the ELM duration in JET-ILW is on average longer than in JET-C (fig. 6.8).

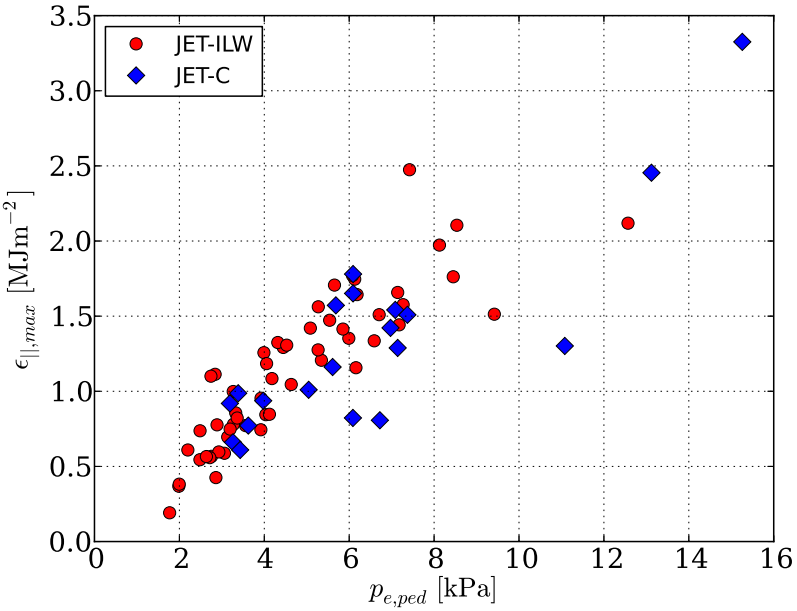

Figure 6.11: Parallel ELM peak energy fluency $\epsilon_{max,||}$ in dependence of the pedestal top electron pressure $p_{e,ped}$ for JET-C and JET-ILW.

For a more detailed understanding of the dependence of the ELM deposited energy fluency a nonlinear regression using the pedestal temperature $T_{e,ped}$, density $n_{e,ped}$ and the relative loss in plasma stored energy $\Delta W/W$ has been performed.

$$\epsilon_{||,scal}(T_{e,ped}, n_{e,ped}) = \epsilon_{||,0}\, T_{e,ped}^{C_{T_e}}\, n_{e,ped}^{C_{n_e}} \left(\frac{\Delta W}{W}\right)^{C_{\Delta W/W}} \qquad \left[\frac{\mathrm{MJ}}{\mathrm{m}^2}\right] \tag{6.19}$$

Where the electron density $n_{e,ped}$ is used in units of 10^{19} m^{-3}, the electron temperature $T_{e,ped}$ in eV and the relative loss in plasma stored energy $\Delta W/W$ in percent. The results for both data sets alone and combined are shown in table 6.4.

	$\epsilon_{\|\|,0}$ $\left[\frac{\mathrm{kJ}}{\mathrm{m}^2}\right]$	C_{T_e}	C_{n_e}	$C_{\Delta W/W}$	R^2
JET-ILW	0.15 ± 0.10	0.89 (07)	1.33 (10)	0.50 (12)	0.85
	0.56 ± 0.32	0.80 (07)	1.41 (11)		0.80
	62.21 ± 55.11	0.39 (13)			0.13
	223.45 ± 57.36		0.84 (16)		0.35
JET-C	0.23 ± 0.20	1.11 (12)	−0.20 (41)	0.43 (20)	0.75
	0.20 ± 0.19	1.18 (13)	0.16 (41)		0.71
	0.22 ± 0.19	1.20 (12)			0.70
	107.13 ± 106.77		0.84 (16)		0.35
JET-ILW + JET-C	0.59 ± 0.30	0.77 (06)	1.26 (14)	0.19 (10)	0.69
	0.54 ± 0.28	0.81 (06)	1.34 (14)		0.68
	4.76 ± 2.99	0.77 (09)			0.37
	270.55 ± 76.03		0.77 (18)		0.17

Table 6.4.: Results of the nonlinear regression of the parallel peak energy fluency for JET-ILW and JET-C.

The results of the nonlinear regression for JET-ILW alone and combined JET-ILW and JET-C are similar. The result from JET-C alone deviates from that, exhibiting a weak density dependence compared to the other results. This can be explained by the parameter space the JET-C data set covers. The density variation is small and does not allow to draw conclusions on the density dependence using this data set alone. In addition the JET-C data is well reproduced using either of the other to regression results.

Notable is the dependence of the relative loss in stored energy $\Delta W/W$ on the peak energy fluency. For both JET-ILW and JET-C alone the dependence is close to the square root. The combined data set exhibits a smaller exponent $C_{\Delta W/W}$ compared to the separated regressions for JET-C and JET-ILW.

Figure 6.12 shows the relative ELM energy loss $\Delta W/W$ in dependence of the parallel peak energy fluency $\epsilon_{||}$. It is seen that the data from JET-CFC exhibit a correlation between the relative ELM energy loss and the parallel peak energy fluency. Including the data from JET-ILW reduces this correlation. No conclusion is drawn whether

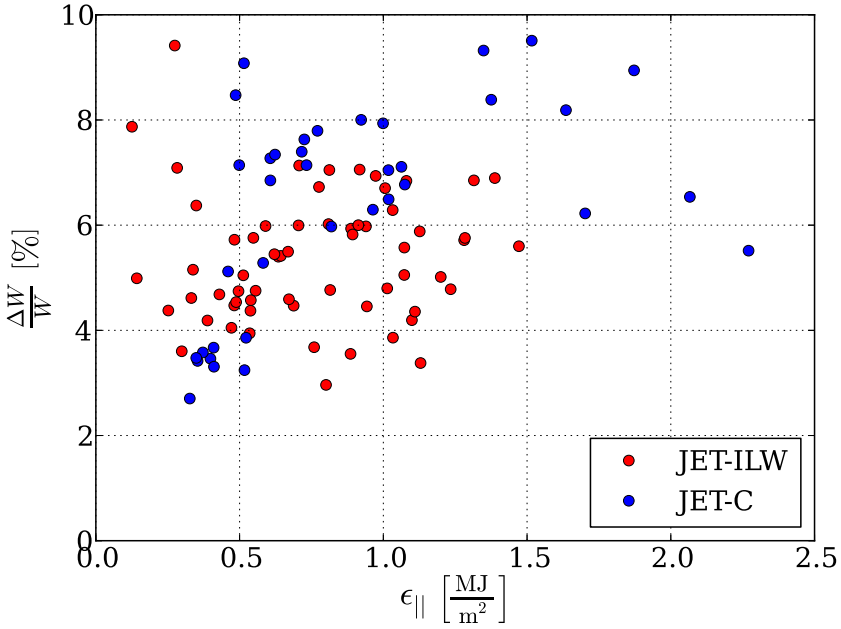

Figure 6.12: Relative ELM energy loss in dependence of the parallel peak energy fluency for both JET-C (blue) and JET-ILW (red).

the residual exponent $C_{\Delta W/W}$ is correct or an artifact of the database. However all regressions allow the conclusion that the dependence of the deposited energy fluency on the target increases less than linear with the relative size of the ELM $\Delta W/W$.

Chapter 7

Summary and Conclusion

In this work the investigation of the divertor power load for two of the largest tokamaks, ASDEX Upgrade and JET, in L- and H-mode is reported. Although for present day devices the occurring power loads in the divertor are tolerable, this will not be the case for future fusion devices such as ITER and DEMO. In the latter devices measures have to be developed to reduce the heat flux onto the plasma facing components in order to have reliable and sustained operation.

For the design of large fusion devices, the energy transport processes in the scrape-off layer of the confined plasma have to be understood. The measurements shown in this work were conducted in ASDEX Upgrade with tungsten plasma facing components and JET with the ITER-like wall (ILW) which consists of beryllium in the main chamber and bulk tungsten as well as tungsten coated CFC in the divertor. Although ITER will have a metal wall, the currently available data on power exhaust stems from machines with a carbon wall. Therefore a comparison to previous findings made in ASDEX Upgrade and JET with carbon plasma facing components with the data obtained in all metal devices is highly required.

Using IR thermography, the heat flux density onto the divertor target plates was measured. Several essential improvements were developed to enable measurements in full metal devices. The heat fluxes in JET exhibit transients in the order of 100 MWm^{-2} for a duration of about 1 ms which is beyond any industrial capabilities available today. Therefore the material properties for the evaluation of the heat flux density were validated using the high heat flux test facility GLADIS. From this we gain:

- A database on the divertor power load for JET with the ITER-like wall with divertor target and upstream plasma measurements, exploiting technical capabilities of this largest fusion device in the world.

- Material properties for heat flux evaluation validated using GLADIS.

The distribution of the heat flux profile on the divertor target is commonly described by a diffusive model. The model contains the upstream power fall-off length λ_q and the divertor broadening S which both contribute to the total width of the profile on the target. To predict the peak heat flux density onto the divertor target plates of a fusion device both λ_q and S have to be known.

For the power fall-off length λ_q in H-mode plasmas, a commonly agreed empirical scaling law obtained in carbon devices exists [3]. Using data from JET with the ILW this scaling is confirmed for an all metal device. Thus it is found that the wall material has no influence on the upstream power fall-off length.

So far, a commonly agreed scaling for the divertor broadening S stayed elusive. For the study of the divertor broadening, L-mode discharges were conducted in ASDEX Upgrade with tungsten plasma facing components.

The measured divertor broadening S is compared to theoretical and empirical predictions. It is found that the perpendicular heat transport in the SOL is not described by classical theory. Both Bohm- and Gyro-Bohm-like heat transport perpendicular to the magnetic field are able to describe the measured data, with a more favorable scaling towards large devices for Bohm diffusion. In both models the perpendicular heat diffusivity depends linear on the temperature. Bohm diffusion is inversely dependent on the total magnetic field whereas Gyro-Bohm diffusion is inversely dependent on the square of the total magnetic field.

In addition to the compared transport models the dependence of the divertor broadening S on the divertor conditions is studied. Most notably using the target electron temperature T_e alone, a scaling is derived which reproduces S. In contrast to classical theory the perpendicular heat diffusivity is found to increase with increasing temperature. This is in agreement with the Bohm- and Gyro-Bohm like models.

The broadening of the heat flux in the divertor region results from the competition between parallel and perpendicular heat transport. It is concluded that the main effect for the broadening S is the decreased parallel heat transport for decreased temperatures.

Using the existing scaling for λ_q and the new scaling for S a prediction for the heat flux in ITER now becomes possible. Assuming a linear dependence of the divertor broadening S on the machine dimensions and a radiative cooling of 90 % it is found that the material limit of 10 $\mathrm{MWm^{-2}}$ is met for a target temperature below 10 eV. This scenario is notably compatible with the requirement for low temperatures at the divertor target in order to prevent tungsten sputtering.

For DEMO it is found that the heat flux limit of 5 MWm^{-2} is more challenging requiring a target temperature below 2 eV. Such low temperatures are commonly associated with detached divertor conditions where the plasma loses energy and momentum before reaching the divertor target. The measurements taken in this work were obtained in attached divertor conditions with low to medium recycling. For low target temperatures and partially detached divertor conditions it is observed that the heat flux profile width on the target increases further. Therefore the heat flux density is expected to be reduced further under those conditions. For steady state heat loads the following can be summarized:

- Empirical scaling for the H-mode power fall-off length λ_q in carbon devices confirmed in JET with an all metal wall.
- Conducted L-mode discharges in ASDEX Upgrade with an all tungsten wall for the study of the divertor heat transport perpendicular to the magnetic field lines.
- Bohm and Gyro-Bohm-like models reproduce the measured divertor broadening.
- Based on the scalings for λ_q and S the consequences for future fusion devices are discussed using the examples ITER and DEMO and for ITER the operation with divertor power loads below 10 MWm^{-2} are predicted to be possible.

H-mode discharges exhibit short periodic burst releasing particles and energy from the confined plasma into the SOL. These bursts are induced by edge localised modes (ELMs). While in present day devices such ELMs do not exceed the threshold thermal load, over which material damage would occur, they might not be acceptable in future fusion devices as their absolute loss energy scales approximately with the plasma volume of the device (R^3). Despite the danger for the plasma facing components an ELMy H-mode is envisioned for future devices. This is done because of the good confinement associated with the H-mode and the fact that ELMs eject impurities from the confined plasma enabling steady state operation. To mitigate the impact of the transient heat loads onto the divertor target plates the current objective is to reduce the total energy loss per ELM. However, published results miss to assess the actual thermal load on the plasma facing components. In other words, they assume a purely linear ratio between energy loss and deposited energy density.

In this work different quantities describing the transient heat load are defined. Their ability to describe the ELM impact on the divertor target is discussed. Indeed it is found that the total energy loss is not a useful quantity to measure the thermal load induced on the divertor target. Therefore, a database for a set of representative values was collected exploiting the technical capabilities of JET. The two main quantities found useful for the assessment of the load onto the divertor are the energy fluency ϵ

and the duration of the energy deposition τ. The energy fluency is the energy density deposited by the transient heat load. The duration of the energy deposition is defined by the time of the start and end of the ELM where the power arriving on the outer divertor is above $1/e$ of the peak power of the ELM.

For the characterisation of the edge of the confined plasma data from the high resolution Thomson scattering (HRTS) system is used. In contrast to earlier attempts, for all discharges the ELM resolved pedestal top electron density $n_{e,ped}$ and $T_{e,ped}$ were collected by optimization of the discharge sequence and configuration. This is needed to have the pedestal density and temperature prior to the ELM occurrence.

The thermal load is estimated by the heat impact factor ΔT which is only dependent on the energy fluency and the energy deposition time. The heat impact factor increases linearly with the energy fluency of the ELM and decreases with the duration of the energy deposition. For the same deposited energy fluency a longer deposition time is beneficial in terms of thermal load, i.e. $\Delta T \propto \epsilon/\sqrt{\tau}$

For JET it is observed that for the entire database the average ELM duration with the ITER-like wall ($\sim$ 2 ms) is longer than the duration observed with carbon plasma facing components ($\sim$ 750 µs). It is found that the ELM duration is dependent on the density and temperature of the plasma at the pedestal. The ELM duration is increased with the pedestal density and decreased with the pedestal temperature.

It is concluded that the ELM duration is independent on the wall material, but the different operational space with on average higher density and lower temperature in JET with the ITER-like wall compared to JET with carbon plasma facing components leads to a on average longer ELM duration.

The different observed ELM durations with the ITER-like wall and carbon plasma facing components are a result of the different pedestal conditions present in JET with carbon and all metal wall. With the ITER-like wall e.g. JET is operated with a higher gas fueling rate in order to prevent impurity accumulation. This results on average in a higher pedestal density and lower pedestal temperature in JET with the ILW compared to the operation with carbon plasma facing components. For the same pedestal density and temperature an identical ELM duration is found with both wall materials within errorbars.

Additionally, it is found that the energy fluency mainly depends on the pedestal pressure of the plasma. Notably, for a fixed pedestal pressure it has a weak dependence on the relative loss in stored energy. For identical pedestal conditions the peak energy fluency parallel to the magnetic field lines is found to be the same within error bars for JET with the ITER-like wall and with carbon plasma facing components. This is

noteworthy since the ELM duration for both cases is largely different on average. In JET with carbon plasma facing components the same energy density is deposited in a shorter time interval compared to the case with the ITER-like wall. These findings support previous reports associating the ELM energy transport with an ergodic reconnection event [70]. It is concluded that the higher energy density resulting from a higher pedestal pressure induces a higher energy density on the target. Summarizing for ELMs the following was found:

- On average longer ELM duration in JET with the ITER-like wall compared to JET with a carbon wall but they become equal when the plasma edge parameters are matched for the two configurations.

- Empirical scaling law for the ELM duration base on the pedestal temperature and density.

- ELM energy fluency ϵ independent on wall material, despite different deposition times, i.e. $\epsilon \sim n \cdot T$ and $\tau \sim \sqrt{n/T}$.

The results of this work offer the opportunity, to predict the power loads caused by ELMs for next step devices, such as ITER.

Acknowledgements

I would like to thank my academic supervisor Professor Ulrich Stroth who enabled this work and who gave valuable suggestions during the work. Furthermore I want to thank Thomas Eich for his great supervision during this thesis. During both my work at ASDEX Upgrade and JET he always was an excellent guidance helping me completing this thesis.

Of course no experiment of this size can be conducted alone. Both at ASDEX Upgrade and JET many people are necessary to keep the machines in operation. Because I cannot mention everyone explicitly, I want to thank the ASDEX Upgrade Team and the JET Home Team for their great support.

For the work on the IR thermography I want to thank the IR teams. At ASDEX Upgrade in particular Albrecht Herrmann and Pascal De Marne who helped me bring the 2D IR system back into operation. At JET I want to thank Gilles Arnoux, Itziar Balboa and Stephan Devaux who during countless and many visits in the torus hall helped to keep the IR system up and running. Special thanks go to Michael Rack who was a great help on the movement correction on the camera.

I want to thank Henri Greuner and Bernd Böswirth for the help on the GLADIS measurements.

For her great support before and during my thesis I want to thank Elisabeth Wolfrum.

For the great time at JET and all the coffee breaks in the fish bowl I want to thank Rudolf Neu, Jörg Hobirk, Peter Lang, Hans Meier, Philippe Mertens, Guy Matthews, Sebastijan Brezinsek, Marc Beurskens, Matthias Brix, Emilia Solano and Dirk Dodt. I want to thank Alexander Bock, Matthias Bernert, Matthias Willensdorfer and Roland Wenninger for all the input during our discussions.

Last but not least I want to thank my whole family for all their great support. My parents for always believing in me and supporting my studies. My sister and her husband for the all the nice time in the garden having barbecues. A special thanks goes to Vanessa, Julie-Ann and Eleanor for being a great support and for their patience regarding my long hours and sometimes whole weekends at JET.

Chapter A

Movement Detection

For the correct measurement of the target heat flux, it is necessary to account for any possible displacements of the camera view during the discharge. For the JET system the displacement is mostly due to forces acting on the camera shielding induces by the nearby poloidal field coils. At ASDEX Upgrade the occurrence of ELMs induces periodic forces onto the camera, which leads to an oscillating displacement. In the following a detection of the displacement based on the information in the acquired images is shown.

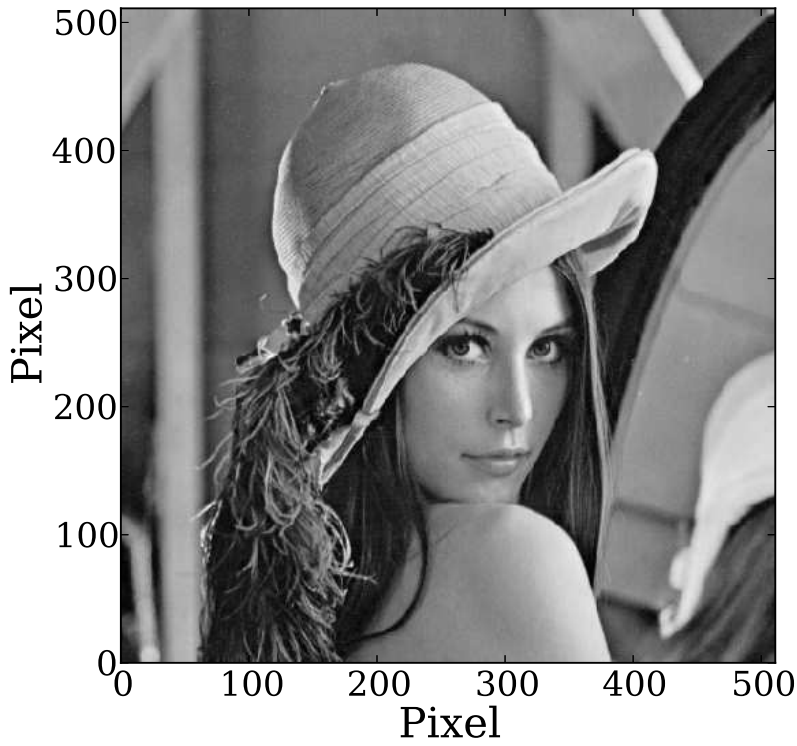

Figure A.1: Sample image [71]

Figure A.1 shows the example image that is used to show the movement detection

algorithm. Two overlapping areas of the image will be used as *reference* and *sample* (fig. A.2) for the algorithm. In addition Gaussian noise was added to both frames to show the robustness of the method against noise.

A.1. Phase Correlation

Phase correlation compares two signals in the frequency domain to obtain the phase shift. By applying phase correlation to images the spatial displacement can be calculated. In the following section the basic algorithm is explained.

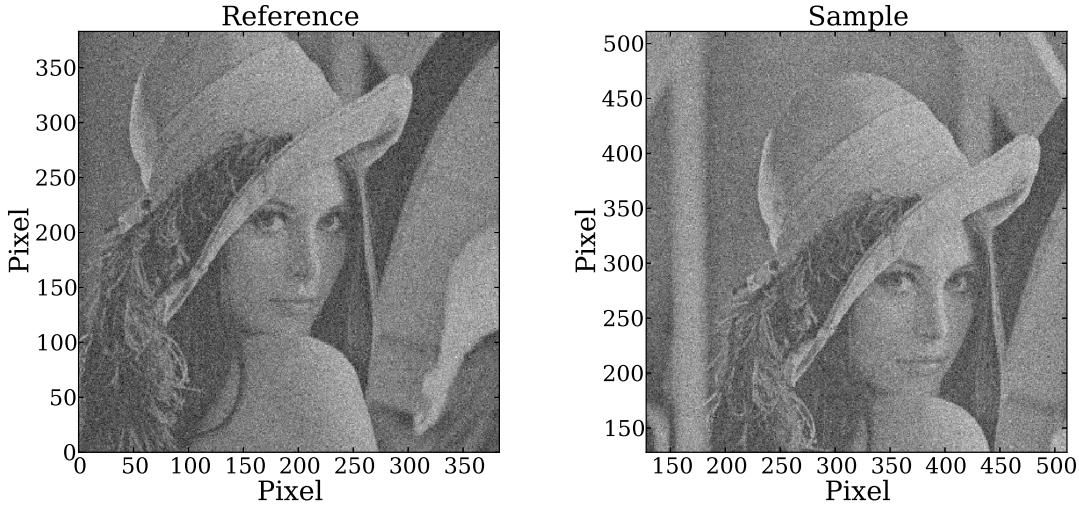

a) Reference b) Sample

Figure A.2: Reference and sample frame with added Gaussian noise.

The reference frame is denoted with g_{ref} and the sample frame is g_{sam}. In a first step the Fourier transforms G_{ref} and G_{sam} of the reference g_{ref} and the sample g_{sam} are computed.

$$G_{ref} = \mathcal{F}(g_{ref}) \tag{A.1}$$

$$G_{sam} = \mathcal{F}(g_{sam}) \tag{A.2}$$

For the computation a fast Fourier transform FFT is recommended especially for large images. The resulting Fourier transforms for the frames (fig. A.2) is shown in figure A.3.

The cross-power spectrum R is calculated by multiplying the reference spectrum G_{ref} with the complex conjugate of the sample spectrum G_{sam} and normalizing the result

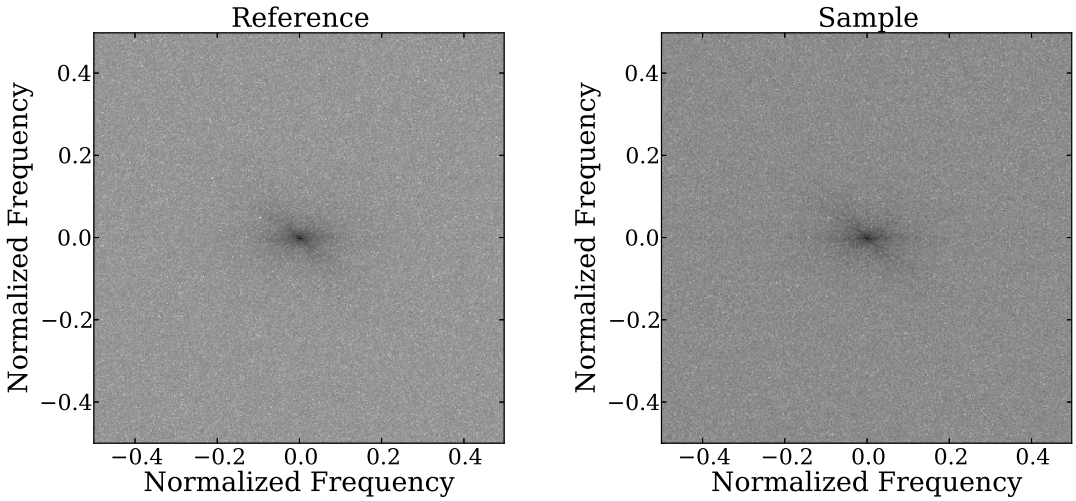

a) Reference b) Sample

Figure A.3: Fourier transform G_{ref} and G_{sam} for the reference and sample frame.

with its absolute value $|G_{ref}G_{sam}^{\dagger}|$.

$$R = \frac{G_{ref}G_{sam}^{\dagger}}{\left|G_{ref}G_{sam}^{\dagger}\right|} \tag{A.3}$$

The phase correlation r is now calculated as the inverse Fourier transform of the cross-power spectrum.

$$r = \mathcal{F}^{-1}(R) \tag{A.4}$$

The position of the maximum of the phase correlation gives the shift between the two frames g_{ref} and g_{ref}.

Figure A.4 shows the phase correlation r between the sample and the reference frame. The maximum of the phase correlation r in the given example lies at (-64, -64) pixels which is the shift that the sample frame needs to overlay the reference frame.

A.2. Improvements

Though the basic phase correlation algorithm has been proven to be able to detect the displacement between two frames, some improvements have been made to further increase the robustness against noise and to increase the resolution of the detection.

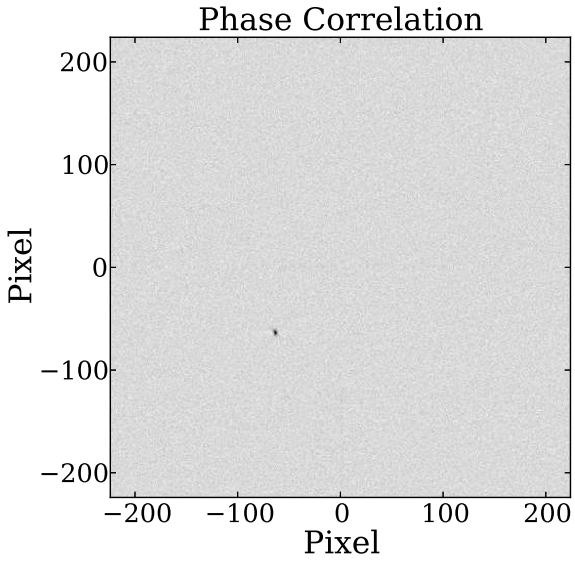

Figure A.4: Phase correlation between the reference and the sample frame. The maximum (black) indicates the shift between the sample and the reference.

A.2.1. Robustness Against Noise

In order to increase the robustness against noise and to reduce the effects induced due to the finite size of the frame, a window function is applied to the cross-power spectrum R (eq. A.3) before the calculation of the phase correlation r (eq. A.4). For the analysis different window functions have been tested and the best results have been with a Hann window [72].

$$w(n) = 0.5 - 0.5\cos\left(\frac{2\pi n}{N-1}\right) \tag{A.5}$$

Where n is the position in the window and N is the total width of the window. Since the acquired images are two dimensional, the window function has to be extended from one dimension to two dimensions. This can be done in two ways. The first one is multiplying two window functions piecewise for every pixel of the image.

$$w(n,m) = w(n) \cdot w(m) \tag{A.6}$$

This method has the advantage, that it can be used easily for non square images. The other method is to calculate a radial symmetric window. This is done by introducing the radius $r(n,m)$ around the center of the image.

$$r(n,m) = \sqrt{\left(n - \frac{N}{2}\right)^2 + \left(m - \frac{M}{2}\right)^2} \tag{A.7}$$

The resulting window function is given as:

$$w(n,m) = \begin{cases} 0.5 - 0.5\cos\left(\dfrac{r(n,m)-1}{2}\right), r \leq 1 \\ 0 \qquad\qquad\qquad\qquad\qquad\quad , r > 1 \end{cases} \tag{A.8}$$

It is advised to crop the image to a square whenever possible to obtain an optimal phase correlation which is not influenced by the choice of the 2D window function.

In the following the phase correlation has been calculated for the reference and sample frame (fig. A.2) with and without the application of the window function. To asses the influence of the window function on the robustness against noise the phase correlation was calculated for different levels of Gaussian noise applied to the frames.

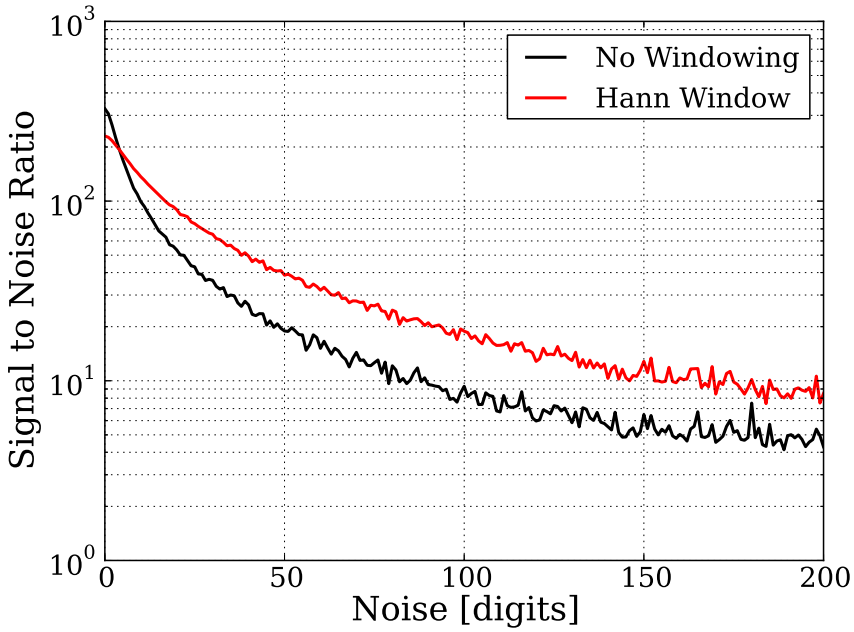

Figure A.5: Signal to noise ratio of the detected peak in the phase correlation with and without application of a Hann window function in dependence on the noise level.

Figure A.5 shows the signal to noise ratio of the detected peak of the phase correlation with and without the application of a Hann window function. For low noise levels the application of the Hann window function reduces the signal to noise ratio compared to the phase correlation without a window function. For medium to large noise levels the signal to noise ratio is significantly higher in the case that the window function is applied.

It is concluded that a window function should be used for the phase correlation since the benefits for medium and large noise levels outweigh the deficits at low noise levels.

A.2.2. Sub Pixel Accuracy

For the evaluation of the heat flux, especially on castellated structures like the bulk tungsten target in JET, it is necessary to calculate the displacement to the reference frame down to sub pixel accuracy. In order to calculate the shift to a higher precision than the sampling precision, the result is interpolated using zero padding.

Zero padding is an interpolation in the frequency domain, which is accomplished by appending zeros at the end of the signal. In the following the amount of zero padding done is specified by k:

$$N_{zero\,padded} = k \cdot N_{signal} \tag{A.9}$$

Where N_{signal} is the number of samples in the signal and $N_{zero\,padded}$ is the length of the signal including appended zeros used for the calculation of the Fourier transform. A k of 1 corresponds to no zero padding.

In the following the effect of zero padding is illustrated by calculating the Fourier transform of a sample signal. The following function for the sample signal is used:

$$f(t) = \sin(t) + \cos(3t) \tag{A.10}$$

The resulting power spectrum of the Fourier transform exhibits strong peaks at a frequency of 1 and 3. The signal $f(t)$ and 32 sample points used for the calculation of the Fourier transform are shown in figure A.6a).

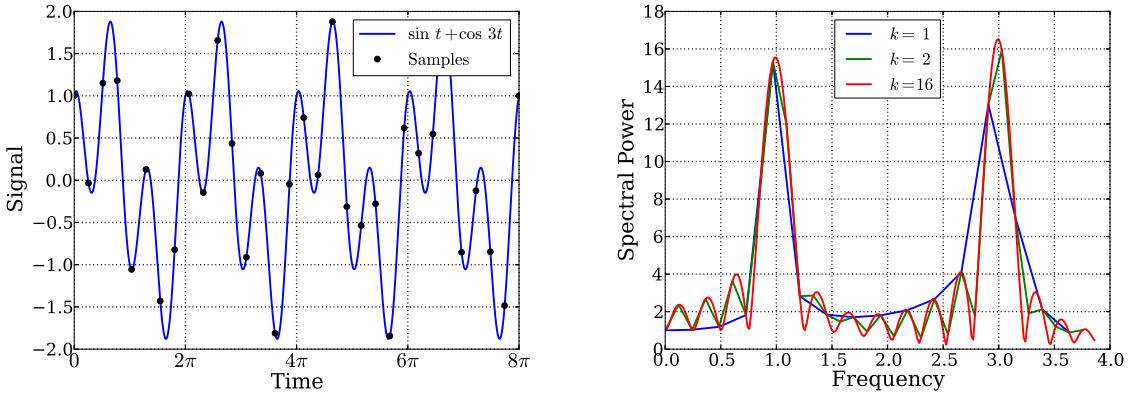

a) Signal b) Power Spectrum

Figure A.6: Signal and power spectrum with applied zero padding.

Figure A.6b) shows the power spectrum resulting from the Fourier transforms for $k = 1, 2, 16$. The case without zero padding (blue) has peaks close to 1 and 3 but is not able to resolve the correct position of the peaks. Applying zero padding with $k = 2$ (green) improves the accuracy and $k = 16$ (red) agrees well with the expected

positions of the peaks. Note here that for an inverse Fourier transform the zeros are added in the middle of the frequency spectrum between the positive and the negative frequencies.

Sub pixel accuracy for the movement detection is achieved by the interpolation of the phase correlation r (eq. A.4) using zero padding in the inverse Fourier transform.

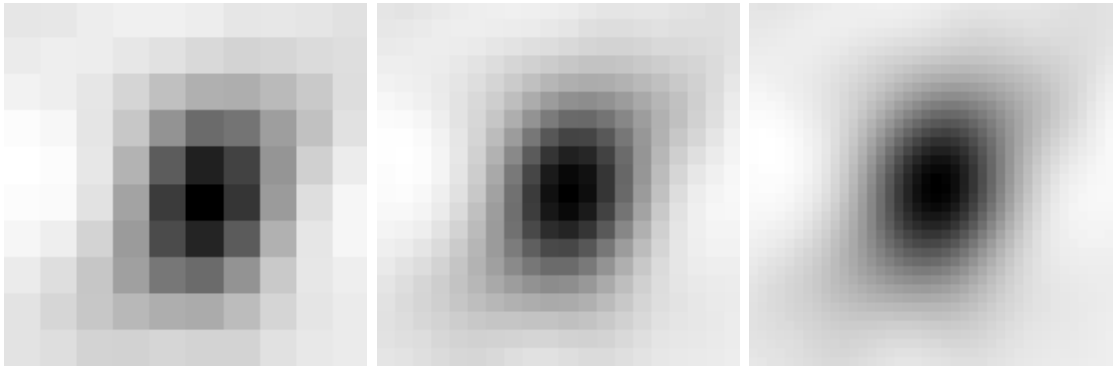

a) k=1 b) k=2 c) k=4

Figure A.7: Phase correlation peak with different amount of zero padding.

Figure A.7 shows the peak of the phase correlation for different amounts of zero padding. It is seen that the shape of the peak is not changed with zero padding but the resolution is increased. The resolution Δ achieved depends on the amount of zero padding k used for the calculation of the phase correlation.

$$\Delta = \frac{1}{k} \qquad \text{[pixel]} \qquad \text{(A.11)}$$

The amount of zero padding k used in the evaluation of the measurement is a trade-off between accuracy and time needed for the calculation of the phase correlation.

Dependent on the quality of the data it might be necessary to apply a time filtering to the evaluated movement to remove falsely detected displacements. For this a running median filter has proven itself useful.

Chapter B

THEODOR

In this chapter the heat flux evaluation code **TH**ermal **E**nergy **O**nto **D**ivert**OR** is shown. THEODOR has been developed to determine the heat flux density profile $q(s,t)$ onto the surface of a target tile from the measured surface temperature evolution $T(s,t)$. The quantity s denotes the position on the surface of the tile, t denotes the time within the measurement. The code calculates the temperature distribution in two dimensions, along the target surface and into the target volume. This is done under the assumption that the measured temperature profile in the tokamak is toroidally symmetric and therefore only one poloidal cross section of the tile is computed. To obtain the heat flux on the surface of the tile the heat diffusion equation (eq. B.1) is solved consecutively for each time step t of the measured surface temperature $T(s,t)$.

$$\rho c_p \frac{\partial T}{\partial t} = \nabla \kappa \nabla T \tag{B.1}$$

Where T is the temperature distribution in the target plate, t is the time, κ is the heat conductivity, ρ is the density and c_p is the specific heat capacity of the target material. Expanding the differential operator on the right hand side results in the following equation.

$$\rho c_p \frac{\partial T}{\partial t} = \kappa \Delta T + (\nabla \kappa) \cdot (\nabla T) \tag{B.2}$$

If the heat conductivity κ is constant ($\nabla \kappa = 0$) for the whole tile the second term on the right hand side vanishes.

$$\rho c_p \frac{\partial T}{\partial t} = \kappa \Delta T \tag{B.3}$$

The code has been developed at a time when computational power was limited and equation B.3 was much more beneficial compared to the full heat diffusion equation B.2 in terms of calculation time. The heat conductivity $\kappa(T)$ however depends on the

material temperature making it necessary to solve the full heat diffusion equation.

A solution to this dilemma was found by introducing the so called heat flux potential U.

$$U(T) = \int_0^T \kappa(T')\mathrm{d}T' \qquad \left[\frac{\mathrm{W}}{\mathrm{m}}\right] \tag{B.4}$$

For the heat flux potential the following relation is easily shown:

$$\frac{\partial U(T)}{\partial T} = \kappa(T) \qquad \left[\frac{\mathrm{W}}{\mathrm{mK}}\right] \tag{B.5}$$

Using this relation the partial differentials are formulated:

$$\frac{\partial U}{\partial t} = \frac{\partial U}{\partial T}\frac{\partial T}{\partial t} = \kappa\frac{\partial T}{\partial t} \tag{B.6}$$

$$\begin{aligned}\frac{\partial^2 U}{\partial x^2} &= \frac{\partial}{\partial x}\frac{\partial U}{\partial x} = \frac{\partial}{\partial x}\kappa\frac{\partial T}{\partial x} \\ &= \frac{\partial \kappa}{\partial x}\frac{\partial T}{\partial x} + \kappa\frac{\partial^2 T}{\partial x^2}\end{aligned} \tag{B.7}$$

Using these differentials, the heat flux equation is rewritten in terms of the heat flux potential U.

$$\frac{\partial U}{\partial T} = \frac{\kappa}{\rho c_p}\frac{\partial^2 U}{\partial x^2} \tag{B.8}$$

This equation has the same form as equation B.3 reducing the computational effort for the solution of the equation while still incorporating the temperature dependent heat conductivity κ. For further simplification the heat diffusivity D is defined as:

$$D = \frac{\kappa}{\rho c_p} \qquad \left[\frac{\mathrm{m}^2}{\mathrm{s}}\right] \tag{B.9}$$

With this the heat diffusion equation is written as:

$$\frac{\partial U}{\partial t} = D\Delta U \tag{B.10}$$

For the discretization of the heat diffusion equation the forward time centered space (FTCS) representation is used.

$$\frac{\partial U}{\partial t} = \frac{U(t+\Delta t) - U(t)}{\Delta t} \tag{B.11}$$

$$\frac{\partial^2 U}{\partial x^2} = \frac{U(x-\Delta x) - 2U(x) + U(x+\Delta x)}{\Delta x^2} \tag{B.12}$$

For the solution of the heat diffusion equation a fully explicit method is used:

$$\begin{aligned} U(t+\Delta t,x,y) = &\left(1-\frac{2\Delta tD}{\Delta x^2}-\frac{2\Delta tD}{\Delta y^2}\right)U(t,x,y) \\ &+\frac{\Delta tD}{\Delta x^2}U(t,x+\Delta x,y)+\frac{\Delta tD}{\Delta x^2}U(t,x-\Delta x,y) \\ &+\frac{\Delta tD}{\Delta y^2}U(t,x,y+\Delta y)+\frac{\Delta tD}{\Delta y^2}U(t,x,y-\Delta y) \end{aligned} \tag{B.13}$$

This update instruction is performed for every time point t in the measurement. For this method the following stability criterion is given:

$$\frac{D\Delta t}{\min(\Delta x^2,\Delta y^2)} \leq 0.5 \tag{B.14}$$

Since the calculation of the next step $U(t+\Delta t,x,y)$ also depends on the heat flux potential U in the neighbouring grid cells, boundary conditions have to be introduced for the edges of the tile. An illustration of the temperature distribution inside the target tile and the boundary conditions can be seen in figure B.1.

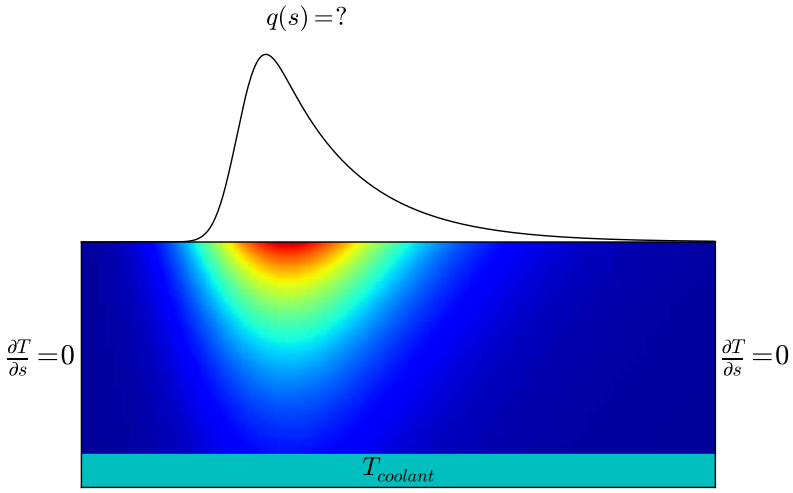

Figure B.1: Illustration of the target heat flux and the temperature distribution in the target plate with boundary conditions.

For the heat flux evaluation the temperature distribution in the target plate is calculated by solving the heat flux equation with measured surface temperature evolution $T(s,t)$ as boundary condition for the target surface. It has been found that infrared thermography can overestimate the surface temperature in the presence of surface imperfections [12] and surface layers [14]. For the use as boundary condition the surface

temperature is corrected:

$$T_{bound}(s,t) = T_(s,t) - \frac{q(s,t)}{\alpha} \qquad [\mathrm{K}] \tag{B.15}$$

Where α is the surface heat transfer coefficient which has to be known. The surface modifications are described as additional thermal resistivity of the surface which causes an increase of the surface temperature proportional to the heat flux onto the target. Because the heat flux $q(s,t)$ is not known, the code uses the heat flux determined in the previous time step $q(s,t-\Delta t)$.

For the lower boundary of the tile a similar boundary condition is used. Here the heat transfer coefficient between the tile and the coolant α_{bot} is used together with the temperature of the coolant T_{cool}.

For both the upper and lower boundary conditions the resulting temperatures are converted to the heat flux potential U which is used in the calculation of the heat diffusion equation (eq. B.13).

For the sides of the tile it is assumed that no heat flows through them. For the heat flux Fourier's law is utilized.

$$\begin{aligned} q &= -\kappa \frac{\partial T}{\partial x} \\ &= -\frac{\partial U}{\partial x} \end{aligned} \qquad \left[\frac{\mathrm{W}}{\mathrm{m}^2}\right] \tag{B.16}$$

If there is no heat flux q then the temperature gradient has to be zero. Because of this the tile temperature distribution at the side of the tile is used as boundary condition for the next step.

In the end the heat flux onto the top of the tile is derived using Fourier's law (eq. B.16). For the calculation the following discretization is used.

$$\frac{\partial U}{\partial y} \approx \frac{3U(t,x,y) - 4U(t,x,y-\Delta y) - U(t,x,y-2\Delta y)}{2\Delta y} \tag{B.17}$$

Assumptions

For the solution of the heat diffusion equation (eq. B.1) THEODOR assumes a functional dependence of the heat conductivity κ and heat diffusivity D on the temperature

T. For this the following parametrization is used.

$$f(T) = a + b\left(1 + \frac{T}{T_0}\right)^{-2} \tag{B.18}$$

Where T is the temperature and a, b and T_0 coefficients that are fitted to the data of κ and D. Using this function for the heat conductivity $\kappa(T)$ the heat flux potential $U(T)$ B.4 can be calculated analytically:

$$U(T) = aT + b\frac{TT_0}{T + T_0} \tag{B.19}$$

Using this function the temperature is converted to the heat flux potential cost efficiently in terms of calculation power. The equation for the heat flux potential (eq. B.19) can be inverted analytically:

$$T(U) = \frac{U - aT_0 - bT_0 + \sqrt{(aT_0 + bT_0 - U)^2 + 4aUT_0}}{2a} \tag{B.20}$$

This allows the quick calculation of the tile temperature to be returned at the location of possible thermocouples.

Chapter C

Fit Reliability Studies of Heat Flux Profiles

In this chapter the reliability of the determination of the power fall-off length λ_q and the divertor broadening S is discussed. For inter-ELM heat flux profiles the influence of noise on the evaluation accuracy is determined. The power fall-off length λ_q and the divertor broadening S are varied between 0.1 and 5.0 mm. For the calculation of the target data a flux expansion of $f_x = 5.5$ and a spatial resolution of 1.65 mm is assumed. For different noise levels synthetic data is generated and λ_q and S are determined. Using this the systematic deviation of the evaluation is studied.

On the basis of the diffusive model introduced in section 4.3.1 for the heat flux profiles synthetic data is generated. The model is written as:

$$q(\bar{s}) = \frac{q_0}{2} \exp\left(\left(\frac{S}{2\lambda_q}\right)^2 - \frac{\bar{s}}{\lambda_q f_x}\right) \operatorname{erfc}\left(\frac{S}{2\lambda_q} - \frac{\bar{s}}{S f_x}\right) + q_{BG} \left[\frac{\mathrm{MW}}{\mathrm{m}^2}\right] \tag{C.1}$$

Where $\bar{s} = s - s_0$ is the distance from the strike line position, q_0 the peak heat flux and λ_q the decay length of the exponential, the divertor diffusion S being the width of the convoluted Gaussian, f_x the flux expansion and q_{BG} the constant background heat flux. The synthetic data is created by adding $1/q(\bar{s})$ dependent noise to the model. This provides data that is close to the experimental observations in ASDEX Upgrade and JET.

The heat flux dependent noise is given by a normal distribution with a standard deviation of

$$\sigma\left(\bar{s}\right) = \delta \cdot \frac{q_{BG}}{q\left(\bar{s}\right)} \tag{C.2}$$

C.1. Synthetic Data

Five different noise levels δ between 0.1 and 1.0 are used for the determination of the fit accuracy of λ_q and S.

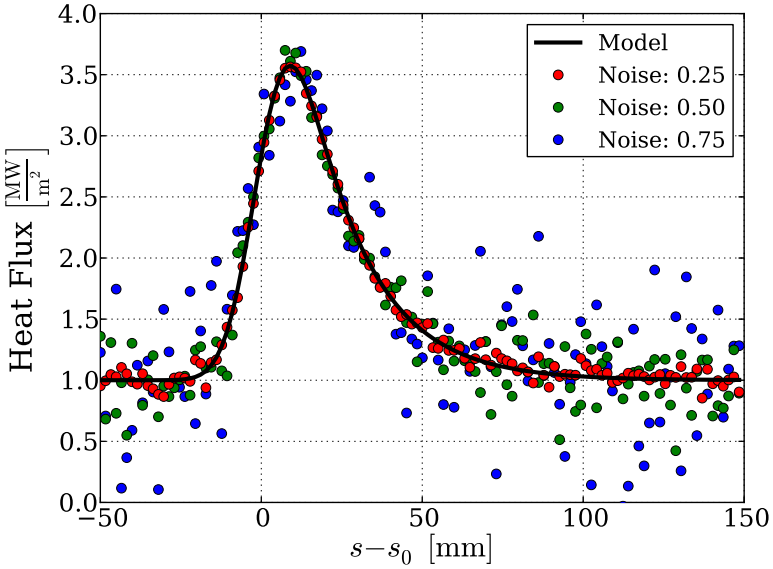

Figure C.1: Examples of synthetic data with different noise levels for $\lambda_q = 3.5$ mm and $S = 2.1$ mm.

Figure C.1 shows synthetic data generated using the heat flux model (eq. C.1) and the heat flux dependent noise (eq. C.2). It is seen that the noise is larger for low heat fluxes compared to areas with high heat flux. This models the higher measurement noise at low temperatures as are present in regions with a low heat flux density.

The noise levels of $\delta = 0.25$ and 0.5 correspond to typical noise levels observed in the data used in this thesis. Lower noise levels are used to show the general ability of the fit to determine the power fall-off length λ_q and the divertor broadening S from the convoluted heat flux model.

Figure C.2 shows the relative error of the determined values of the power fall-off length λ_q and the divertor broadening S for a low noise level of $\delta = 0.1$. The relative error is defined as follows:

$$\Delta\lambda_q = \left| \frac{\lambda_q - \lambda_{q,fit}}{\lambda_q} \right| \tag{C.3}$$

$$\Delta S = \left| \frac{S - S_{fit}}{S} \right| \tag{C.4}$$

Where $\lambda_{q,fit}$ and S_{fit} are values determined using the synthetic data. It is seen that for the whole parameter range the fit is able to determine both λ_q and S.

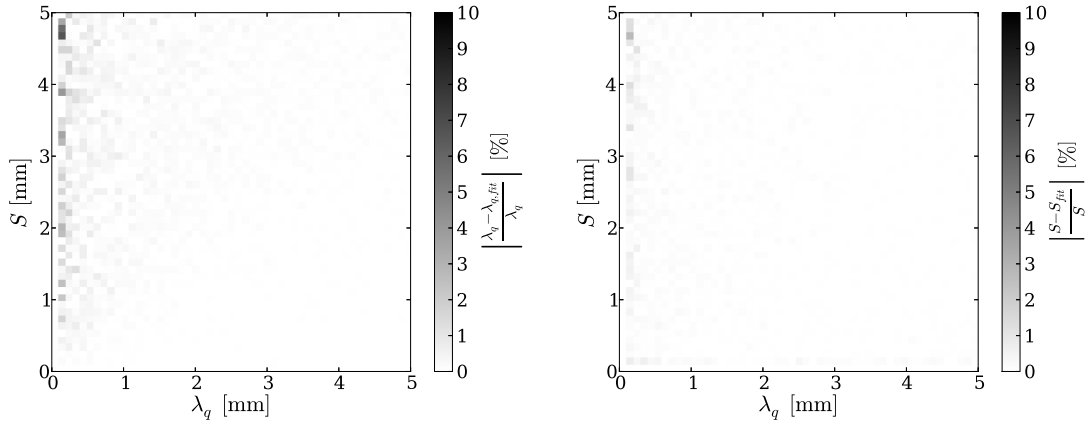

a) Power fall-off length λ_q b) Divertor Broadening S

Figure C.2: Relative error of the determined values of λ_q and S for a noise level of $\delta = 0.1$.

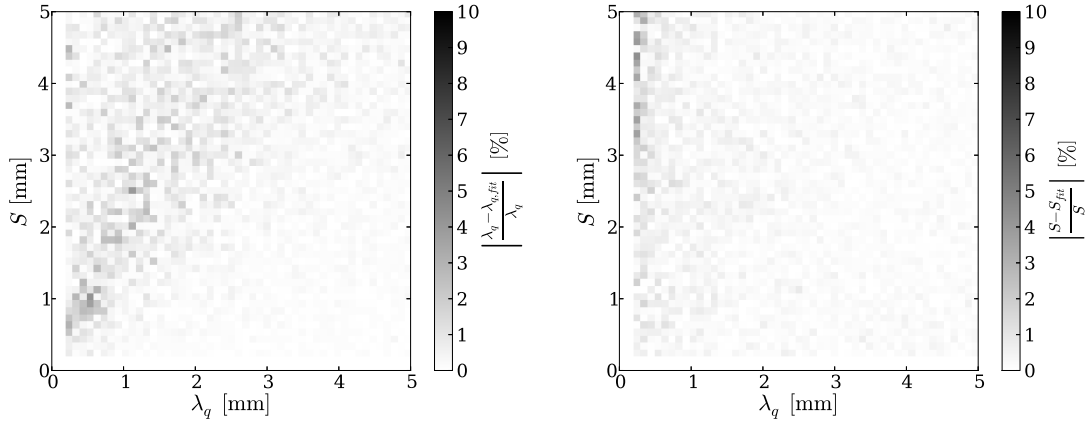

a) Power fall-off length λ_q b) Divertor Broadening S

Figure C.3: Relative error of the determined values of λ_q and S for a noise level of $\delta = 0.25$.

In figure C.3 the relative error of both λ_q and S are shown for a noise level of $\delta = 0.25$. It is seen that the error for the divertor broadening S is low. A larger error of up to 5 % is only observed for a large divertor broadening $S > 3$ mm and small power fall-off length $\lambda_q < 0.3$ mm. The fit is able to determine the power fall-off length in cases where λ_q is larger than the divertor broadening S. Otherwise the error increases to up to 5 %.

For a noise level of $\delta = 0.5$ (fig. C.4) the fit is able to determine the power fall-off length if the divertor broadening S is smaller than λ_q. For a divertor broadening S larger than λ_q the uncertainty increases to over 10 %, especially for small values of λ_q and S. For a small power fall-off length $\lambda_q < 0.4$ mm the error of the divertor broadening S strongly increases to over 10 %.

The general trend observed in the previous cases is continued for a large noise level

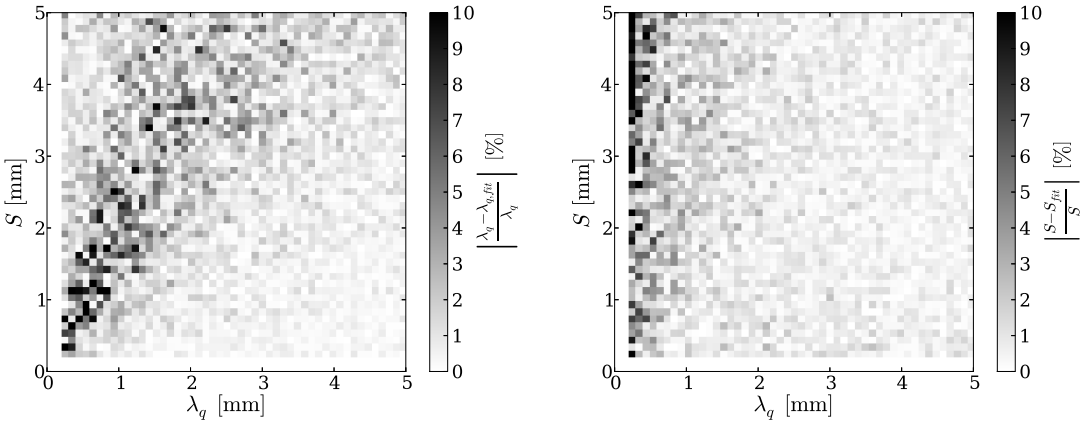

a) Power fall-off length λ_q b) Divertor Broadening S

Figure C.4: Relative error of the determined values of λ_q and S for a noise level of $\delta = 0.5$.

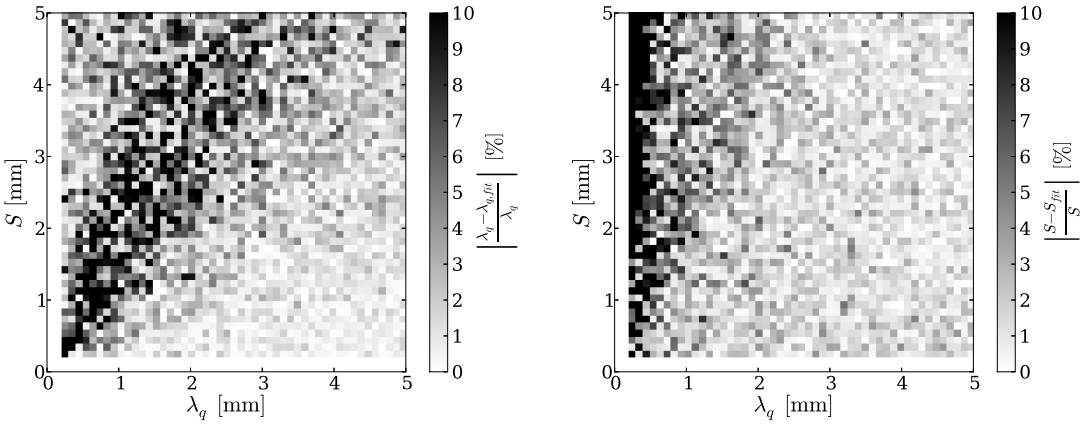

a) Power fall-off length λ_q b) Divertor Broadening S

Figure C.5: Relative error of the determined values of λ_q and S for a noise level of $\delta = 0.75$.

of $\delta = 0.75$. Where λ_q is larger than S the fit is able to reproduce the power fall-off length λ_q, although the error increases to up to 5 % in this region. For the divertor broadening S the error for small values of $\lambda_q < 0.4$ mm increases further. In general the error increases with increasing noise level.

The case with a high noise level of $\delta = 1.0$ (fig. C.6) is included to show the limits of the determination of the power fall-off length λ_q and the divertor broadening S. The error for both the power fall-off length λ_q and the divertor broadening S increases further and the region where λ_q is determined with a comparably low error decreases. The error of the divertor broadening S increases especially for small values of $\lambda_q < 2$ mm.

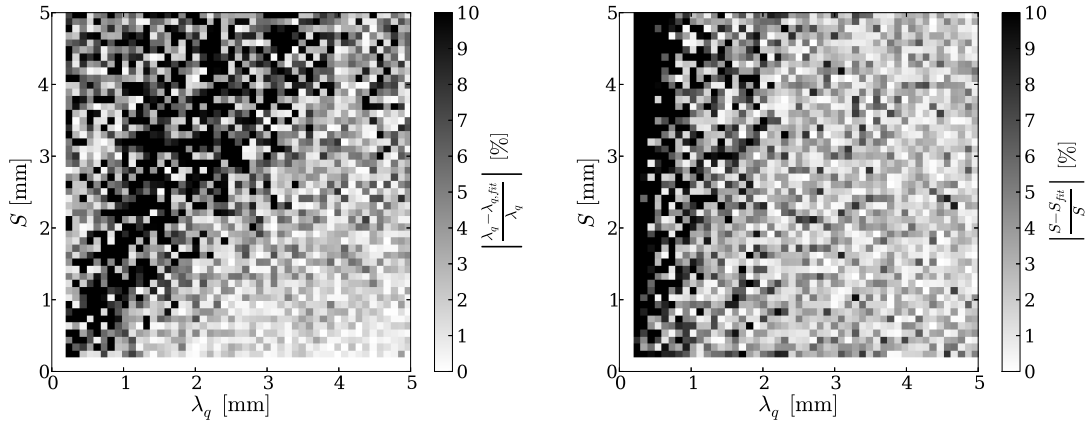

a) Power fall-off length λ_q b) Divertor Broadening S

Figure C.6: Relative error of the determined values of λ_q and S for a noise level of $\delta = 1.0$.

C.2. Comparison to Measured Data

In the following the data measured in JET with both carbon (JET-C) and ITER-like wall (JET-ILW) and in ASDEX Upgrade with a full tungsten wall is compared to the results obtained using the synthetic data. Figure C.7 shows a comparison of the

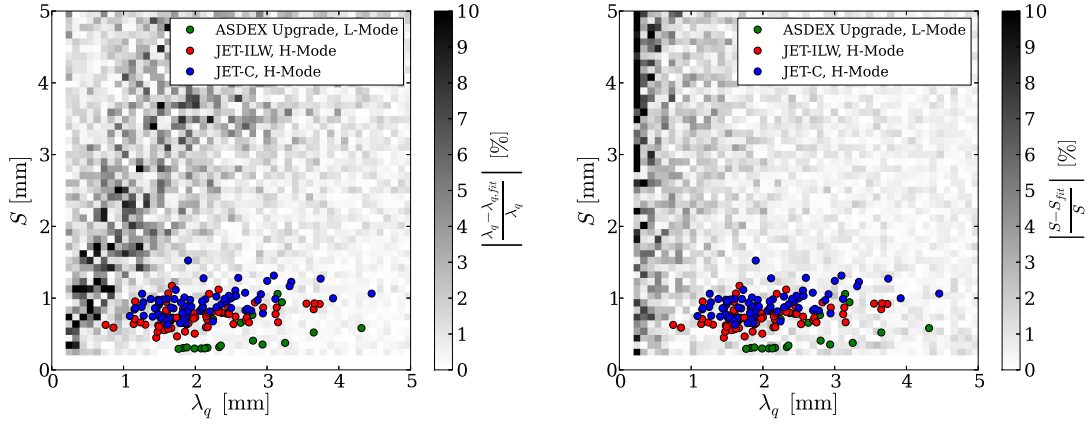

a) Power fall-off length λ_q b) Divertor Broadening S

Figure C.7: Relative error of the determined values of λ_q and S for a noise level of $\delta = 0.5$ in comparison to measured values in ASDEX Upgrade and JET.

measured data to the relative error of the fit at a noise level of $\delta = 0.5$. This noise level is chosen for the comparison because it is a good representation of the noise observed in the measurement. It is seen that the available data covers a parameter range where the error is small for both the power fall-off length λ_q and the divertor broadening S. Note here that the study is using the spatial resolution of the JET IR system, the data from ASDEX Upgrade has a better spatial resolution of 1.3 mm. It is concluded that for all data used in this thesis the fit is able to reproduce the power fall-off length λ_q and the divertor broadening S.

Bibliography

[1] R. Neu, V. Bobkov, R. Dux, A. Kallenbach, Th. Pütterich, H. Greuner, O. Gruber, A. Herrmann, Ch. Hopf, K. Krieger, C.F. Maggi, H. Maier, M. Mayer, V. Rohde, K. Schmid, and W. Suttrop. Final steps to an all tungsten divertor tokamak. *Journal of Nuclear Materials*, 363–365(0):52–59, 2007.

[2] V. Philipps, Ph. Mertens, G.F. Matthews, and H. Maier. Overview of the JET ITER-like Wall Project. *Fusion Engineering and Design*, 85(7–9):1581–1586, 2010.

[3] T. Eich, B. Sieglin, A. Scarabosio, W. Fundamenski, R.J. Goldston, and A. Herrmann. Inter-ELM power decay length for JET and ASDEX Upgrade: Measurement and comparison with heuristic drift-based model. *Physical Review Letters*, 107(21), 2011.

[4] J. Wesson and D.J. Campbell. *Tokamaks*. International Series of Monographs on Physics. OUP Oxford, 2011.

[5] G.G.Dolgov-Saveliev, D.P. Ivanov, V.S. Mukhovatov, K.A. Razumova, V.S. Strelkov, M.N. Shepelyev, and N.A. Yavlinsky. Investigations of the stability and heating of plasmas in toroidal chambers. In *Proc. Second United Nations Intern. Conf. on the Peaceful Use of Atomic Energy*, volume 32, pages 82–9, Geneva, September 1958.

[6] EFDA. `http://www.efda.org`, 2014. Accessed: 2014-01-17.

[7] G. Federici, R. Kemp, D. Ward, C. Bachmann, T. Franke, S. Gonzales, C. Lowry, M. Gadomska, J. Harman, B. Meszaros, C. Morlock, F. Romanelli, and R. Wenninger. Overview of EU DEMO Design and R&D Activities. *Fusion Engineering and Design*, Accepted, 2014.

[8] M. Planck. Über eine Verbesserung der Wienschen Spektralgleichung. *Deutsche Physikalische Gesellschaft*, Verhandlungen 2:202–204, 1900.

[9] M. Planck. Zur Theorie des Gesetzes der Energieverteilung im Normalspektrum. *Deutsche Physikalische Gesellschaft*, Verhandlungen 2:237–245, 1900.

[10] A Herrmann, W Junker, K Gunther, S Bosch, M Kaufmann, J Neuhauser, G Pautasso, Th Richter, and R Schneider. Energy flux to the ASDEX-Upgrade diverter plates determined by thermography and calorimetry. *Plasma Physics and Controlled Fusion*, 37(1):17, 1995.

[11] A. Herrmann, P. Franzen, W. Herrmann, C. F. Fuchs, M. Weinlich, ASDEX Upgrade Team, NI Team, and ICRH Team. Energy Deposition at the Divertor Plates During Elmy H-Mode and Poloidal and Toroidal Distribution of Heat Load on the Wall in ASDEX Upgrade. In M. Schittenhelm, R. Bartiromo, and F. Wagner, editors, *Europhysics Conference Abstracts (Proc. of the 24th EPS Conference on Controlled Fusion and Plasma Physics, Berchtesgaden, 1997)*, volume 21A, part IV, pages 1417–1420, Petit-Lancy, 1997. EPS.

[12] A. Herrmann. Thermal properties of plasma exposed carbon and heat flux calculations on a spatial scale of a few microns. *Journal of Nuclear Materials*, 337–339 (0):907–911, 2005.

[13] A. Herrmann, H. Greuner, N. Jaksic, B. Böswirth, F. Reimold, A. Scarabosio, S. Vorbrugg, and M. Wischmeier. Design and concept validation of the new solid tungsten divertor for ASDEX Upgrade. *Fusion Engineering and Design*, 2013.

[14] S. Devaux, G. Arnoux, T. Eich, H. Thomsen, S. Brezinsek, P. Coad, J. Likonen, M. Stamp, and A. Widdowson. Surface layers effect on heat loads on the JET divertor targets. *38th EPS Conference on Plasma Physics 2011, EPS 2011 - Europhysics Conference Abstracts*, 35 1:49–52, 2011.

[15] R. Neu, R. Dux, A. Geier, O. Gruber, A. Kallenbach, K. Krieger, H. Maier, R. Pugno, V. Rohde, and S. Schweizer. Tungsten as plasma-facing material in ASDEX Upgrade. *Fusion Engineering and Design*, 65(3):367–374, 2003.

[16] Tetsuo Tanabe. Tritium issues to be solved for establishment of a fusion reactor. *Fusion Engineering and Design*, 87(5–6):722–727, 2012.

[17] R.A Causey, J.N Brooks, and G Federici. Tritium inventory and recovery in next-step fusion devices. *Fusion Engineering and Design*, 61–62(0):525–536, 2002.

[18] ASDEX Upgrade. `http://www.aug.ipp.mpg.de`, 2014. Accessed: 2014-01-17.

[19] M. Kaufmann. *Plasmaphysik und Fusionsforschung*. Teubner Studienbücher. Teubner B.G. GmbH, 2003.

[20] I. Balboa, G. Arnoux, T. Eich, B. Sieglin, S. Devaux, W. Zeidner, C. Morlock, U. Kruezi, G. Sergienko, D. Kinna, P. D. Thomas, M. Rack, and JET EFDA Contributors. Upgrade of the infrared camera diagnostics for the JET ITER-like wall divertor. *Review of Scientific Instruments*, 83(10):10D530, 2012.

[21] R. Pasqualotto, P. Nielsen, C. Gowers, M. Beurskens, M. Kempenaars, T. Carlstrom, D. Johnson, and JET-EFDA Contributors. High resolution Thomson scattering for Joint European Torus (JET). *Review of Scientific Instruments*, 75(10): 3891–3893, 2004.

[22] H. Greuner, B. Boeswirth, J. Boscary, and P. McNeely. High heat flux facility GLADIS: Operational characteristics and results of W7-X pre-series target tests. *Journal of Nuclear Materials*, 367-370, Part B(0):1444–1448, 2007.

[23] Y R Martin, T Takizuka, and the ITPA CDBM H-mode Threshold Database Working Group. Power requirement for accessing the H-mode in ITER. *Journal of Physics: Conference Series*, 123(1):012033, 2008.

[24] F. Ryter, S.K. Rathgeber, L. Barrera Orte, M. Bernert, G.D. Conway, R. Fischer, T. Happel, B. Kurzan, R.M. McDermott, A. Scarabosio, W. Suttrop, E. Viezzer, M. Willensdorfer, E. Wolfrum, and the ASDEX Upgrade Team. Survey of the H-mode power threshold and transition physics studies in ASDEX Upgrade. *Nuclear Fusion*, 53(11):113003, 2013.

[25] C.F. Maggi, G. Calabro, E. Delabie, M. Groth, N.C. Hawkes, M. Lehnena, E. de la Luna, K. McCormick, F. Militello, C. Reux, F. Rimini, E.R. Solano, V. Bobkov, M. Brix, A. Czarnecka, J. Flanagan, E. Lerche, S. Marsen, I. Nunes, B. Sieglin, D. Van Eester, and JET EFDA contributors. The H-Mode Threshold in JET with the ITER-Like Wall. *Proceedings of the 39th European Physical Society Conference on Plasma Physics, Stockholm, Sweden*, 2013.

[26] F. Wagner. A study of the perpendicular particle transport properties in the scrape-off layer of ASDEX. *Nuclear Fusion*, 25(5):525, 1985.

[27] M.A. Makowski, D. Elder, T.K. Gray, B. Labombard, C.J. Lasnier, A.W. Leonard, R. Maingi, T.H. Osborne, P.C. Stangeby, J.L. Terry, and J. Watkins. Analysis of a multi-machine database on divertor heat fluxes. *Physics of Plasmas*, 19(5), 2012.

[28] A Loarte, S Bosch, A Chankin, S Clement, A Herrmann, D Hill, K Itami, J Lingertat, B Lipschultz, K McCormick, R Monk, G.D Porter, M Shimada, and M Sugihara. Multi-machine scaling of the divertor peak heat flux and width for L-mode and H-mode discharges. *Journal of Nuclear Materials*, 266–269(0):587–592, 1999.

[29] R.A. Pitts, S. Carpentier, F. Escourbiac, T. Hirai, V. Komarov, S. Lisgo, A.S. Kukushkin, A. Loarte, M. Merola, A. Sashala Naik, R. Mitteau, M. Sugihara, B. Bazylev, and P.C. Stangeby. A full tungsten divertor for ITER: Physics issues and design status. *Journal of Nuclear Materials*, 438, Supplement(0):S48–S56, 2013.

[30] T. Eich, B. Sieglin, A. Scarabosio, A. Herrmann, A. Kallenbach, G.F. Matthews, S. Jachmich, S. Brezinsek, M. Rack, and R.J. Goldston. Empirical scaling of inter-ELM power widths in ASDEX Upgrade and JET. *Journal of Nuclear Materials*, 2013.

[31] L. Spitzer Jr. and R. Härm. Transport phenomena in a completely ionized gas. *Physical Review*, 89(5):977–981, 1953.

[32] A. Scarabosio, T. Eich, A. Herrmann, and B. Sieglin. Outer target heat fluxes and power decay length scaling in L-mode plasmas at JET and AUG. *Journal of Nuclear Materials*, 2013.

[33] B Sieglin, T Eich, A Scarabosio, G Arnoux, I Balboa, S Devaux, A Herrmann, F Hoppe, M Hölzl, A Kallenbach, P Lang, G F Matthews, S Marsen, S Pamela, M Rack, R Wenninger, the ASDEX Upgrade Team, and JET EFDA Contributors. Power load studies in JET and ASDEX-Upgrade with full-W divertors. *Plasma Physics and Controlled Fusion*, 55(12):124039, 2013.

[34] A. Scarabosio, G. Haas, H.W. Müller, R. Pugno, and M. Wischmeier. Measurements of neutral gas fluxes under different plasma and divertor regimes in ASDEX Upgrade. *Journal of Nuclear Materials*, 390–391(0):494–497, 2009.

[35] B.K. Venkanna. *Fundamentals of Heat and Mass Transfer*. Prentice-Hall Of India Pvt. Limited, 2010. ISBN 9788120340312.

[36] D Bohm, A Guthrie, and R K Wakerling. *The Characteristics of electrical discharges in magnetic fields*. McGraw-Hill, 1st ed edition, 1949.

[37] A Taroni, M Erba, E Springmann, and F Tibone. Global and local energy confinement properties of simple transport coefficients of the bohm type. *Plasma Physics and Controlled Fusion*, 36(10):1629, 1994.

[38] P.C. Stangeby. *The Plasma Boundary of Magnetic Fusion Devices: Peter C. Stangeby*. Plasma physics series. Institute of Physics Publishing, 2000.

[39] A S Kukushkin and H D Pacher. Divertor modelling and extrapolation to reactor conditions. *Plasma Physics and Controlled Fusion*, 44(6):931, 2002.

[40] A Kallenbach, D Coster, J C Fuchs, H Y Guo, G Haas, A Herrmann, L D Horton, L C Ingesson, C F Maggi, G F Matthews, R D Monk, J Neuhauser, F Ryter, J Schweinzer, J Stober, W Suttrop, ASDEX Upgrade Team, and JET Team. Closed divertor operation in ASDEX Upgrade and JET. *Plasma Physics and Controlled Fusion*, 41(12B):B177, 1999.

[41] M. Wischmeier, M. Groth, A. Kallenbach, A.V. Chankin, D.P. Coster, R. Dux, A. Herrmann, H.W. Müller, R. Pugno, D. Reiter, A. Scarabosio, and J.G. Watkins. Current understanding of divertor detachment: Experiments and modelling. *Journal of Nuclear Materials*, 390–391(0):250–254, 2009.

[42] A. Kallenbach, M. Kaufmann, D.P. Coster, J.C. Fuchs, A. Herrmann, J. Neuhauser, R. Schneider, K. Borrass, H.-S. Bosch, A. Carlson, J. Gafert, K. Lackner, K. Schmidtmann, J. Schweinzer, W. Suttrop, U. Wenzel, and ASDEX Upgrade Team. Scrape-off layer radiation and heat load to the ASDEX Upgrade LYRA divertor. *Nuclear Fusion*, 39(7):901, 1999.

[43] A Kallenbach, R Dux, J C Fuchs, R Fischer, B Geiger, L Giannone, A Herrmann, T Lunt, V Mertens, R McDermott, R Neu, T Pütterich, S Rathgeber, V Rohde, K Schmid, J Schweinzer, W Treutterer, and ASDEX Upgrade Team. Divertor power load feedback with nitrogen seeding in ASDEX Upgrade. *Plasma Physics and Controlled Fusion*, 52(5):055002, 2010.

[44] A. Kallenbach, M. Bernert, T. Eich, J.C. Fuchs, L. Giannone, A. Herrmann, J. Schweinzer, W. Treutterer, and the ASDEX Upgrade Team. Optimized tokamak power exhaust with double radiative feedback in ASDEX Upgrade. *Nuclear Fusion*, 52(12):122003, 2012.

[45] A.W. Leonard, A. Herrmann, K. Itami, J. Lingertat, A. Loarte, T.H. Osborne, W. Suttrop, the ITER Divertor Modeling, Database Expert Group, and the ITER Divertor Physics Expert Group. The impact of ELMs on the ITER divertor. *Journal of Nuclear Materials*, 266–269(0):109–117, 1999.

[46] A. Loarte, G. Saibene, R. Sartori, M. Becoulet, L. Horton, T. Eich, A. Herrmann, M. Laux, G. Matthews, S. Jachmich, N. Asakura, A. Chankin, A. Leonard, G. Porter, G. Federici, M. Shimada, M. Sugihara, and G. Janeschitz. ELM energy and particle losses and their extrapolation to burning plasma experiments. *Journal of Nuclear Materials*, 313–316(0):962–966, 2003.

[47] T. Eich, H. Thomsen, W. Fundamenski, G. Arnoux, S. Brezinsek, S. Devaux, A. Herrmann, S. Jachmich, and J. Rapp. Type-I ELM power deposition profile width and temporal shape in JET. *Journal of Nuclear Materials*, 415(1, Supplement):S856–S859, 2011.

[48] H Zohm. Edge localized modes ELMs. *Plasma Physics and Controlled Fusion*, 38 (2):105, 1996.

[49] E J Doyle, R J Groebner, K H Burrell, P Gohil, T Lehecka, N C Luhmann Jr, H Matsumoto, T H Osborne, W A Peebles, and R Philipona. Modifications in

turbulence and edge electric fields at the L-H transition in the DIII-D tokamak. *Physics of Fluids B*, 3(8):2300–2307, 1991.

[50] P Gohil, M Ali Mahdavi, L Lao, K H Burrell, M S Chu, J C Deboo, C L Hsieh, N Ohyabu, R T Snider, R D Stambaugh, and R E Stockdale. Study of giant edge-localized modes in DIII-D and comparison with ballooning theory. *Physical Review Letters*, 61(14):1603–1606, 1988.

[51] W Suttrop, K Büchl, H J de Blank, J Schweinzer, H Zohm, ASDEX Upgrade team, NBI group, and ICRH group. Characteristics of edge localized modes in ASDEX Upgrade. *Plasma Physics and Controlled Fusion*, 38(8):1407, 1996.

[52] R Scannell, A Kirk, N Ben Ayed, P G Carolan, G Cunningham, J McCone, S L Prunty, and M J Walsh. Experimental investigation into ELM filament formation on MAST. *Plasma Physics and Controlled Fusion*, 49(9):1431, 2007.

[53] C.P. Perez, H.R. Koslowski, G.T.A. Huysmans, T.C. Hender, P. Smeulders, B. Alper, E. de la Luna, R.J. Hastie, L. Meneses, M.F.F. Nave, V. Parail, M. Zerbini, and JET-EFDA Contributors. Type-I ELM precursor modes in JET. *Nuclear Fusion*, 44(5):609, 2004.

[54] N. Oyama, N. Asakura, A.V. Chankin, T. Oikawa, M. Sugihara, H. Takenaga, K. Itami, Y. Miura, Y. Kamada, K. Shinohara, and the JT-60 Team. Fast dynamics of type I ELMs and transport of the ELM pulse in JT-60U. *Nuclear Fusion*, 44(5):582, 2004.

[55] J. Stober, M. Maraschek, G.D. Conway, O. Gruber, A. Herrmann, A.C.C. Sips, W. Treutterer, H. Zohm, and ASDEX Upgrade Team. Type-II ELMy H-modes on ASDEX Upgrade with good confinement at high density. *Nuclear Fusion*, 41 (9):1123, 2001.

[56] K.H. Burrell, S.L. Allen, G. Bramson, N.H. Brooks, R.W. Callis, T.N. Carlstrom, M.S. Chu, A.P. Colleraine, D. Content, J.C. Deboo, R.R. Dominguez, J.R. Ferron, R.L. Freeman, P. Gohil, C.M. Greenfield, R.J. Groebner, G. Haas, W.W. Heidbrink, D.N. Hill, F.L. Hinton, R.-M. Hong, W. Howl, C.L. Hsieh, G.L. Jackson, G.L. Jahns, R.A. James, A.G. Kellman, J. Kim, L.L. Lao, E.A. Lazarus, T. Lehecka, J. Lister, J. Lohr, T.C. Luce, J.L. Luxon, M.A. Mahdavi, H. Matsumoto, M. Mayberry, C.P. Moeller, Y. Neyatani, T. Ohkawa, N. Ohyabu, T. Okazaki, T.H. Osborne, D.O. Overskei, T. Ozeki, A. Peebles, S. Perkins, M. Perry, P.I. Petersen, T.W. Petrie, R. Philipona, J.C. Phillips, R. Pinsker, P.A. Politzer, G.D. Porter, R. Prater, M.E. Rensink, M.J. Schaffer, D.P. Schissel, J.T. Scoville, R.P. Seraydarian, M. Shimada, T.C. Simonen, R.T. Snider, G.M. Staebler, B.W. Stallard, R.D. Stambaugh, R.D. Stav, H. St. John, R.E. Stockdale,

E.J. Strait, Taylor P.l., T.S. Taylor, P.K. Trost, U. Stroth, R.E. Waltz, S.M. Wolfe, R.D. Wood, and D. Wroblewski. Confinement physics of H-mode discharges in DIII-D. *Plasma Physics and Controlled Fusion*, 31(10):1649–1664, 1989.

[57] W Suttrop. The physics of large and small edge localized modes. *Plasma Physics and Controlled Fusion*, 42(5A):A1, 2000.

[58] M.W. Jakubowski, W. Fundamenski, G. Arnoux, Th. Eich, R.A. Pitts, D. Reiter, and R.C. Wolf. ELM filament interaction with the JET main chamber. *Journal of Nuclear Materials*, 390–391(0):781–784, 2009.

[59] S. Devaux, T. Eich, G. Arnoux, W. Fundamenski, and H. Thomsen. Type-I ELM filamentary substructure on the JET divertor target. *Journal of Nuclear Materials*, 415(1, Supplement):S865–S868, 2011.

[60] J. Marki, R.A. Pitts, J. Horacek, and D. Tskhakaya. ELM induced divertor heat loads on TCV. *Journal of Nuclear Materials*, 390–391(0):801–805, 2009.

[61] A.J. Thornton, A. Kirk, I.T. Chapman, and J.R. Harrison. Divertor heat fluxes and profiles during mitigated and unmitigated edge localised modes (ELMs) on the Mega Amp Spherical Tokamak (MAST). *Journal of Nuclear Materials*, 438, Supplement(0):S199–S202, 2013.

[62] T.D. Rognlien, R.H. Cohen, D.D. Ryutov, and M.V. Umansky. Comparison of ELM heat loads in snowflake and standard divertors. *Journal of Nuclear Materials*, 438, Supplement(0):S418–S421, 2013.

[63] T. Hirai, F. Escourbiac, S. Carpentier-Chouchana, A. Fedosov, L. Ferrand, T. Jokinen, V. Komarov, A. Kukushkin, M. Merola, R. Mitteau, R.A. Pitts, W. Shu, M. Sugihara, B. Riccardi, S. Suzuki, and R. Villari. ITER tungsten divertor design development and qualification program. *Fusion Engineering and Design*, 88(9–10):1798–1801, 2013.

[64] J. Linke, F. Escourbiac, I.V. Mazul, R. Nygren, Rödig M., J. Schlosser, and S. Suzuki. High heat flux testing of plasma facing materials and components - Status and perspectives for ITER related activities. *Journal of Nuclear Materials*, 367–370 B(SPEC. ISS.):1422–1431, 2007.

[65] Th. Loewenhoff, J. Linke, G. Pintsuk, and C. Thomser. Tungsten and CFC degradation under combined high cycle transient and steady state heat loads. *Fusion Engineering and Design*, 87(7–8):1201–1205, 2012.

[66] G.J. van Rooij, J.W. Coenen, L. Aho-Mantila, S. Brezinsek, M. Clever, R. Dux, M. Groth, K. Krieger, S. Marsen, G.F. Matthews, A. Meigs, R. Neu, S. Potzel, T. Pütterich, J. Rapp, and M.F. Stampp. Tungsten divertor erosion in all metal

devices: Lessons from the ITER like wall of JET. *Journal of Nuclear Materials*, 438, Supplement(0):S42–S47, 2013.

[67] W. Fundamenski, R.A. Pitts, and JET EFDA contributors. A model of ELM filament energy evolution due to parallel losses. *Plasma Physics and Controlled Fusion*, 48(1):109, 2006.

[68] T. Eich, A. Kallenbach, W. Fundamenski, A. Herrmann, and V. Naulin. On the asymmetries of ELM divertor power deposition in JET and ASDEX Upgrade. *Journal of Nuclear Materials*, 390–391(0):760–763, 2009.

[69] D. Moulton, W. Fundamenski, G. Manfredi, S. Hirstoaga, and D. Tskhakaya. Comparison of free-streaming ELM formulae to a Vlasov simulation. *Journal of Nuclear Materials*, 438, Supplement(0):S633–S637, 2013.

[70] T. Eich, A. Herrmann, and J. Neuhauser. Nonaxisymmetric Energy Deposition Pattern on ASDEX Upgrade Divertor Target Plates during Type-I Edge-Localized Modes. *Physical Review Letters*, 91:195003, Nov 2003.

[71] Python. `http://www.python.org`, 2014. Accessed: 2014-01-24.

[72] R. B. Blackman and J. W. Tukey. The Measurement of Power Spectra from the Point of View of Communications Engineering - Part I. *Bell System Technical Journal*, 37(1):185–282, 1958.